INVESTIGATION OF SURFACE FILMS IN LITHIUM-ION BATTERIES

A Thesis
Presented to
The Academic Faculty

by

Rajiv R. Jaini

In Partial Fulfillment
of the Requirements for the Degree
Doctor of Philosophy in the
School of School of Chemical & Biomolecular Engineering

Georgia Institute of Technology
May 2017

INVESTIGATION OF SURFACE FILMS IN LITHIUM-ION BATTERIES

Approved by:

Dr. Thomas F. Fuller, Advisor
School of Chemical & Biomolecular Engineering
Georgia Institute of Technology

Dr. Ryan P. Lively
School of Chemical & Biomolecular Engineering
Georgia Institute of Technology

Dr. Paul A. Kohl
School of Chemical & Biomolecular Engineering
Georgia Institute of Technology

Dr. Gleb Yushin
School of Materials Science & Engineering
Georgia Institute of Technology

Dr. William J. Koros
School of Chemical & Biomolecular Engineering
Georgia Institute of Technology

Date Approved: December 21, 2016

To whom batteries may concern

ACKNOWLEDGEMENTS

I wish to thank Professor Thomas F. Fuller for his guidance and encouragement. A sincere thanks is given to the committee members for their recommendations. I would like to thank my labmates, past and present. These members include KwangSup Eom, Erin Redmond, Brian, Setzler, Vyran George, Tapesh Joshi, Andrew Star, Greg Chipman, and Jung Fang.

I would like to thank my family members, including new members, for their continued support and steadfast inspiration. Finally, a special thank you to my friends Mustafa Ali and Jean-Guillame Durand for their wisdom in all aspects of life.

TABLE OF CONTENTS

ACKNOWLEDGEMENTS iv
LIST OF TABLES vii
LIST OF FIGURES viii
LIST OF SYMBOLS AND ABBREVIATIONS xii
SUMMARY xvii

CHAPTER 1 INTRODUCTION 1
Scope of Work 1
Background 2
Investigating the Solid Electrolyte Interphase Formed by Additive Reduction at 0.6 V *vs.* Li/Li^+ Using Physics-Based Modeling 2
Investigation of the Differences in Passivation Mechanisms of Neat and Additive-Containing Electrolytes 3
A Physics-Based Model of the Impedance Response of a Graphite|LiNMC Cell 3
Summary and Recommendations 3

CHAPTER 2 BACKGROUND 4
Components and Features of Lithium-Ion Batteries 4
Capacity Fade 6
Accelerated Testing 8
Causes of Capacity Fade 9
The Characterization of the Solid Electrolyte Interphase 12
Using Planar Electrodes to Investigate the Formation and Growth of the SEI 14
Chemical Additives for Improved Battery Performance 17
Mathematical Modeling of LiBs 18
References 24

CHAPTER 3 INVESTIGATING THE SOLID ELECTROLYTE INTERPHASE FORMED BY ADDITIVE REDUCTION AT 0.6 V *VS.* LI/LI^+ USING PHYSICS-BASED MODELING 36
Introduction 36
Model Development 39
Transient Model for Simulation of Cyclic Voltammetry 40
Simulation of Impedance Model 43
Experimental 46
Results and Discussion 49
Determining Extent of Surface Passivation 49
Ferrocene Reaction on Pristine Electrode 54
Characterization of Surface Passivation Using Ferrocene 56
Estimation of Kinetic and Transport Parameters 63
Model Fitting Uniqueness Explored 70
FIB+SEM Imaging of the Thickness of the SEI 72
Polymerization Reactions Driving the Formation of Large SEI Thicknesses 74

IR Spectroscopy to Determine Polymerization Effect 76
Conclusion 79
Acknowledgments 80
References 81

CHAPTER 4 INVESTIGATION OF THE DIFFERENCES IN PASSIVATION MECHANISMS OF NEAT AND ADDITIVE-CONTAINING ELECTROLYTES 85
Introduction 85
Experimental 88
Model 91
Results 91
Pristine Electrode 91
SEI Formation 92
The Validity of the Bruggeman Relation 104
Conclusion 114
References 116

CHAPTER 5 A PHYSICS-BASED MODEL OF THE IMPEDANCE RESPONSE OF A GRAPHITE|LINMC CELL 118
Introduction 118
Model Formulation 122
General Model Equations 122
Physical-Model Equations Transformed 130
Simulation of Impedance Model 131
Impedance Definitions 132
Single-Particle Model Development 132
Expansion to a Porous Electrode 137
Open-Circuit Potential Functions 139
Experimental Procedure 140
Experimental Results 141
Cathode Particle TEM Results 141
Full Cell Impedance Response Measurements 142
Model Results 146
Conclusions 156
References 158

CHAPTER 6 SUMMARY AND RECOMMENDATIONS 169

LIST OF TABLES

Table 1. List of parameters used for the solid matrix, electrolyte, separator, and SEI physical properties that are assumed constant in each simulation. 146

Table 2. A parameter comparison of fresh and aged cells. 147

LIST OF FIGURES

Figure 2.1. Illustration of the components of a LiB.The composite negative electrode shows a surface film enveloping the electrode particles. 5

Figure 2.2. Charge capacity of $LiNi_{0.8}Co_{0.15}Al_{0.05}O_2$|graphite cell. When charging the cell, lithium is inserted into the graphite negative electrode particles. A cycle represents the action of charging and discharging graphite with respect to constant cut-off voltages. The charge capacity of the cell decreases with increasing cycle number, illustrating the action of capacity fade. 7

Figure 3.1: Illustration of electrode, SEI, and electrolyte (not to scale). L_p is the thickness of the porous SEI, and L_d is the thickness of the diffusion layer. A sample concentration profile is provided of a diffusing species, *s*. The diffusing species is solvent or redox couple. 40

Figure 3.2. CV scans of glassy carbon in neat, FEC-containing, and VC-containing electrolytes. The first two cycles for each sample are given, with v = 10 mV-s^{-1}. Data in blue and green correspond to neat electrolyte. Data in red and black correspond to FEC-containing electrolyte. Data in magenta and cyan correspond to VC-containing electrolyte. Reduction current densities are generally equivalent to or higher over a given cycle for electrolyte with FEC and VC than neat electrolyte. A large decay in the 1st cycle current is observed for all electrolytes. There is no evidence of intercalation into the electrode. 50

Figure 3.3. Sample SEI formation curves in neat electrolyte on a pristine glassy-carbon electrode under a potentiostatic hold at 0.6 V *vs.* Li/Li$^+$. (a) Current density and (b) total formation charge, -*q*, versus time of the potentiostatic hold. 52

Figure 3.4. Film-formation charge versus the square root of the hold time for neat, FEC-containing, and VC-containing electrolyte passivated at 0.6 V *vs.* Li/Li$^+$. The total charge was obtained by integrating the current over the passivation time. .. 53

Figure 3.5. CVs of cleaned glassy carbon without (black) and with (red) the Fc/Fc$^+$. CVs were obtained at 1 mV-s^{-1}. Redox-couple electrolyte contains approximately 1.8 and 1.4 mmol of Fc and Fc$^+$, respectively. The reversible condition, governed by the Nernst expression, is shown as a comparison to the redox couple CV. The Nernst condition shows that the cleaning procedure is effective in removing films from the surface of the electrode. 55

Figure 3.6. Nyquist plots of the impedance response of Fc/Fc$^+$ before and after passivation. Responses to increasing passivation times are given. (a) Entire spectra given after passivation in neat electrolyte. (b) Entire spectra given for various hold times after passivation in FEC-containing electrolyte. (c) Entire spectra given for various hold times after passivation in VC-containing electrolyte. (d) The spectra in (a) are stretched to show high-frequency behavior.

(e) The spectra in (b) are stretched to show high-frequency behavior. (f) The spectra in (c) are stretched to show high-frequency behavior. 58

Figure 3.7. CVs of Fc/Fc^+ before and after passivation. Scan rates are 10 $mV\text{-}s^{-1}$. (a) 5th cycle CVs for an electrode passivated in neat electrolyte. (b) 5th cycle CVs for an electrode passivated in electrolyte containing FEC. (c) 5th cycle CVs for an electrode passivated in electrolyte containing VC. 62

Figure 3.8. Sample Nyquist plots, Bode plots, and CVs of Fc/Fc^+ with simulation results overlaid. The (a), (b), and (c) correspond to neat electrolyte and (d), (e), and (f) to FEC-containing electrolyte. Response to ten minute and forty-five minute passivation times are shown and insets are provided for the high-frequency portion of the impedance spectra. VC-containing electrolyte passivation (not shown) appears similar in fitting. 64

Figure 3.9. SEI physical parameters obtained from impedance and CV experimental data fittings of Fc/Fc^+. Parameters are fitted for SEIs formed from electrolytes in neat, FEC-, and VC-containing electrolyte. (a) exchange-current densities, (b) SEI thickness, and (c) porosity to tortuosity ratios are provided from the fittings as a function of passivation time. 69

Figure 3.10. Model fitting uniqueness is explored. Two simulation results with different SEI thickness and tortuosity parameters are overlaid on experimental data for 45 minutes of passivation in neat electrolyte. In simulation one, the overlaid model spectrum captures the shape of the impedance spectra for a given thickness and tortuosity, with respect to the characteristic frequency. In simulation two, the thickness is doubled and porosity to tortuosity is halved from simulation one. The resulting simulation worsens as a result of the parameter change. 71

Figure 3.11. HR-SEM images for electrodes passivated in neat, FEC-, and VC-containing electrolytes. The thicknesses observed by microscopy are on the same order of magnitude as predicted by the model. 73

Figure 3.12. The experimental formation charge per unit volume of SEI formed. The total formation charge per unit volume of SEI has been obtained by normalizing the formation charges experimentally measured in Figure 3.4 by the SEI thicknesses obtained from simulation, shown in Figure 3.9. The normalized formation charge values are provided for neat, FEC-, and VC-containing electrolyte. An additional compound is shown in the figure, Li_2CO_3, which is known to be a standard organic SEI formation product for neat electrolyte. 75

Figure 3.13. FTIR spectra for neat, FEC-, and VC-passivated electrodes. A fresh electrode spectrum is provided, as a baseline. The FTIR spectra comparison indicates the presence of polymerized compounds post passivation. 77

Figure 4.1. Experimental (A and B) and simulated (Nernst) CVs for a pristine glassy-carbon electrode with Fc/Fc^+ in the electrolyte. The CV scans are obtained at 1 $mV\text{-}s^{-1}$. Approximately 1.8 mmol and 1.6 mmol of Fc^+ and Fc, respectively, have

been added to neat electrolyte. Day to day reproducibility of experimental voltammograms is good. A simulated CV is overlaid on the experimental CVs. The cleaning procedure is effective in restoring the electrode after passivation.. 92

Figure 4.2. Formation charge measurement at 0.1 V and 0.3 V. Multiple experiments for neat, FEC-, and VC-containing electrolytes are shown at each potential. Figures in each column are measured at the labeled potential. The final point from each formation charge curve is shown as the last subfigure in each column. The shape of the curves over the sampled time is parabolic, independent of the electrolyte. The final points from the formation charge curve experiments are also parabolic with time. 95

Figure 4.3. The linear dependence of the formation charge *vs.* $\sqrt{t}$ at 0.1 V and 0.3 V vs. Li/Li^+. Multiple experiments for neat, FEC-, and VC-containing electrolytes are shown at each potential. Figures in each column are measured at the labeled potential..... 96

Figure 4.4. Impedance responses of Fc/Fc^+after passivation at 0.3 V *vs.* Li/Li^+. Both Nyquist and Bode plots are shown for neat, FEC-, and VC-containing electrolytes. Four formation charges are shown. (a) and (b) correspond to neat electrolyte, (c) and (d) correspond to FEC-containing electrolyte, and (e) and (f) correspond to VC-containing electrolyte. The magnitude of the impedance increases with increasing passivation time for all electrolytes. However, additive-containing electrolyte appears to be less effective at passivating the surface than neat electrolyte..... 101

Figure 4.5. Impedance responses of Fc/Fc^+ after passivation at 0.1 V *vs.* Li/Li^+. Both Nyquist and Bode plots are shown for neat, FEC-, and VC-containing electrolytes. Four formation charges are shown. (a) and (b) correspond to neat electrolyte, (c) and (d) correspond to FEC-containing electrolyte, and (e) and (f) correspond to VC-containing electrolyte. The magnitude of the impedance increases with increasing passivation time for all electrolytes. However, additive-containing electrolyte appears, at best, to be equally passivating as neat electrolyte..... 102

Figure 4.6. Average slope of formation charge vs. the square root of time. Neat, FEC-containing, and VC-containing electrolyte passivation slopes are calculated at 0.1 V, 0.3 V, and 0.6 V. The 0.6 V slopes are obtained from experimental data, shown in Figure 3.3(b). Neat and FEC-containing electrolyte tend to similar average slopes. VC-containing electrolyte is markedly different in average slope. The data suggests that formation is not only limited by rates of mass-transfer of solvent through the SEI..... 104

Figure 4.7. SEM image of a glassy-carbon electrode with SEI and Nyquist and Bode plots of Fc/Fc^+ under the same passivation conditions. (a) The electrode is passivated in neat electrolyte for 10 minutes at 0.3 V. The SEI appears structurally homogeneous and approximately 500 nm in thickness. (b) Nyquist plot and (c) Bode plot of the impedance response with simulation results overlaid.

simulation results are overlaid on experimental data. The Bruggeman relation only effectively represents the data when the SEI thickness is set to 31 μm. For a description of the labels "Bruggeman" and "Free Parameters," see text. 106

Figure 4.8. Characteristic frequency and bulk Fc^+ concentration relationship. The impedance response of 10 min passivated samples at 0.3 V is given. The concentration of Fc^+ is increased and measurements are obtained at approximately 3.241 V for all samples. Measurements for neat, FEC-, and VC-containing electrolytes are provided. The characteristic frequency is labelled 'f_c.' A downward pointing arrow is shown in the direction of increasing Fc+ concentration. There is a noticeable shift in the characteristic frequency with increasing concentration, suggesting adsorption of Fc^+ on the formed SEI. 109

Figure 4.9. Nyquist and Bode plots of the impedance response of the Fc/Fc^+ after 10 minutes of passivation at 0.3 V in neat electrolyte, with simulation results overlaid. The adsorption fitting parameter, $\boldsymbol{dQ/dc_{Fc^+}}$ is changed amongst simulations. $\boldsymbol{dQ/dc_{Fc^+}}$ is 5.8 (squares), 4.7 (circles), 4 (upward triangles), and 3.6 (downward triangles). 113

Figure 5.1. Illustration of the dual-lithium ion insertion cell with two porous insertion electrodes with separator and current collectors. Secondary particles are shown in the main illustration. A detailed primary particle is shown in an expanded version of the illustration. The graphite electrode particles are enveloped by a surface film. 123

Figure 5.2. Detailed charge placement illustration, with corresponding current paths for the development of the single particle model. See text for discussion. 124

Figure 5.3. The open-circuit potential function of the cathode material. 130

Figure 5.4. TEM images of fresh (a) and aged (b) cells taken of the cathode. (c) and (d) are magnifications of (a) and (b), respectively. A surface layer is found on the cathode particles following aging. Images obtained from the unpublished work of Jung Tae Lee et al. 142

Figure 5.5. Experimental impedance responses for both fresh and calendar-aged full cells. (a) Nyquist-plot format of the entire spectrum for each cell, (b) the real and imaginary axes of (a) are been expanded, and (c) Bode-plot format of the entire spectrum for each cell. Fresh (squares) and calendar aged (circles) indicate that degradation leads to a separate process that causes the formation of a distinct semicircle in Nyquist-plot format at high frequencies. Spectra were obtained from the unpublished work of Tapesh Joshi *et al.* 145

Figure 5.6. Nyquist- and Bode-plot formats of the impedance response at 50 % SOC for a full graphite|LiNMC cell during first cycle charging. 149

Figure 5.7. Nyquist- and Bode-plot formats of the impedance response at 50 % SOC for a full graphite|LiNMC cell after 3200 hours of calendar aging at 75° C. 154

LIST OF SYMBOLS AND ABBREVIATIONS

α_a	anodic charge transfer coefficient
α_c	cathodic charge transfer coefficient
ε	porosity
ε_p	porosity of SEI
γ	exponent for solid diffusivity
θ	active site for insertion into solid
κ	conductivity, S/m
η	surface overpotential, V
ρ	density, g/cm^3
ν	scan rate, mV/s
σ	conductivity in the solid phase, S/m
τ	tortuosity
Φ	potential, V
ω	angular frequency, rad/s
Ω	dimensionless term describing solid transport
a	specific surface area of the porous electrode, m^2/m^3
A	area of working electrode, m^2
C_{dl}	double-layer capacitance, F/m^2
c	lithium concentration in solution phase, mol/m^3
$c_{i,d}$	concentration in diffusion layer, mol/m^3

$c_{i,p}$	concentration in porous layer, mol/m^3
c_{max}	maximum Li concentration inside the active material, mol/m^3
c_s	lithium concentration in the solid phase, mol/m^3
c_{sf}	particle surface concentration, mol/m^3
D	lithium diffusion coefficient in the solution phase, m^2/s
D_{eff}	effective lithium diffusion coefficient in the solution phase, m^2/s
D_i	diffusivity, m^2/s
D_s	lithium diffusion coefficient inside the active material, m^2/s
e^-	electron
EOL	end of life
f_A	thermodynamic activity
F	Faraday's constant, 96,487 C-mol^{-1}
f_c	characteristic frequency, Hz
Fc^+	ferrocenium hexafluorophosphate
Fc	ferrocene
i	current density, A/m^2
i_0	exchange-current density, A/m^2
i_1	current density in the solid phase, A/m^2
i_2	current density in the solution phase, A/m^2
i_{dl}	double-layer current, A/m^2
i_{int}	intercalation current density, A/m^2
i_n	pore-wall current density, A/m^2
I	total superficial current density, A/m^2

j	imaginary unit
L	thickness, m
L_d	length of diffusion layer, m
Li^+	lithium ion
L_p	length of porous layer, m
n_{Li}	mole fraction of lithium
N_S	solvent flux in SEI layer, mol/(m^{2}s)
MW	molecular weight, g/mol
$N_{i,d}$	superficial flux in diffusion layer, mol/m^2/s
$N_{i,p}$	superficial flux SEI, mol/m^2/s
Q_v	formation charge, C/cm^3
r	radial distance from the center of the particle, m
R	universal gas constant, J/mol/K
R_e	electrolyte resistance, Ω -m^2
R_{part}	particle impedance, Ω - m^2
R_s	particle radius, m
R_{SEI}	resistance of the SEI layer, Ω - m^2
s_i	stoichiometric coefficient of intercalation reaction
S	solvent
t	time, s
t_+^0	transport number of lithium ion
T	temperature, K
x	distance from the anode current collector, m

x_i	dimensionless Li concentration at electrode surface
U	thermodynamic potential, V
V	cell potential, V
Z	impedance, Ω - cm^2

Subscripts

0	exchange-current density subscript
1	solid phase
2	solution phase
a	anodic
an	anode
b	bulk
ca	cathode
conc	concentration
dl	double layer
d	diffusion layer
e	electrolyte
f	film
far	faradaic
Im	imaginary
Li_2CO_3	lithium carbonate
Li	lithium
max	maximum

o	oxidized species, ferrocenium
part	particle
p	SEI
r	reduced species, ferrocene
Re	real
s	solid
sf	surface
$\overline{overbar}$	steady-state variable
$\widetilde{tilde}$	complex variable

SUMMARY

In this work, we present a detailed investigation of the role of surface films on electrodes used in lithium-ion batteries (LiBs). Surface films are proven to reduce LiB capacity but are beneficial for the long-term performance of a battery. Therefore, the formation and growth of these surface films is of much interest to the future development of batteries. In the negative electrode, the surface film is referred to as the solid electrolyte interphase (SEI).

We investigate SEI formation on a model electrode with a model, *in situ* electrochemical probe. The electrode is planar glassy carbon, and the electrochemical probe is the ferrocene redox shuttle. The ferrocene redox shuttle is assumed analogous to solvent molecules in the solution phase. SEIs are formed at 0.6 V *vs.* Li/Li^+ and are characterized with the ferrocene redox shuttle. Results are found to contrast with observations in the literature about the role of additives in battery electrolytes.

In the second part of our work, we build on part one to determine if our model system is representative of real battery behavior. SEIs are formed at lower potentials at which practical operation of a real battery is conducted. The ferrocene redox shuttle is used to characterize the formed SEIs. It is determined that the benefits of additives are never observed in the model system. The evidence presented suggests that ferrocene is not an analog of solvent.

In the third part of our work, the previous investigations of negative electrode surface films are extended to the positive electrode of a real LiB. Imaging of calendar aged positive electrodes indicates the formation of a surface film. Impedance

measurements show the development of a new arc in the spectrum. The two observations are combined, and an investigation into surface film formation on the cathode is conducted. A full-cell physics-based model is developed to simulate the impedance response to determine if the cathode surface film results in a new arc. Simulation of the impedance response suggests that, although it is possible that the film causes a new arc in the spectrum, the result is not likely.

CHAPTER 1

INTRODUCTION

Lithium-ion batteries (LiB) are used in a wide array of mobile and stationary applications because of their high energy densities and long cycle lives. For example, the widespread usage of mobile phones has been largely facilitated by the high energy densities of LiBs. With continued advancements in mobile and stationary applications, the demands placed on LiB performance is only increasing.

There are two avenues that can be taken to improve LiB performance. First, new materials with higher capacities and energy densities can be developed. Both negative and positive electrode materials have been the focus of many investigations detailed in the literature. Second, improved performance of LiBs can be achieved through designing the components of the battery to prevent the onset of prominent degradation mechanisms. This preventative design requires identifying and understanding the causes of degradation in LiBs. For example, the primary mode of degradation in the negative electrode of LiBs is surface film formation. In the cathode, surface film formation is also a less understood mode of degradation. The films are the products of complex reactions between the electrode and the electrolyte. The films have been shown to reduce battery life but are necessary for ensuring high energy densities in LiBs. Therefore, a complete understanding of surface films is needed for the continual improvement of LiBs.

Scope of Work

In this work, we present three investigations aimed at elucidating the characteristics of surface films formed on negative and positive electrode materials in lithium-ion batteries. In the first two sections of the work, we present a detailed study on surface film formation in the negative electrode using a model system. The design of the system is advantageous because of its simplicity and well-defined physical characteristics. Therefore, the enhanced analytical ability is found to compensate for the lack of practicality of the material. In the third section of the work, we demonstrate the advantages of physics-based mathematical modeling in the analysis of experimental data.

Background

A literature review on the relevant degradation modes and modeling techniques that are used to investigate lithium-ion battery performance is presented.

Investigating the Solid Electrolyte Interphase Formed by Additive Reduction at 0.6 V *vs.* Li/Li^+ Using Physics-Based Modeling

In Chapter 3, we use a model electrode-electrolyte system to investigate the benefits of additives in lithium-ion batteries. Neat and additive-containing electrolytes are used to passivate planar glassy carbon at 0.6 V *vs.* Li/Li^+ and form an SEI. The ferrocene redox couple is then introduced into the electrolyte under the assumption that its kinetic and mass-transport behavior is analogous to solvent molecules. Counterintuitive behavior is found to result from electrochemical characterization of ferrocene kinetic and mass-transport. That is, the benefits of additives are never

observed. The counterintuitive behavior is discussed, and an *ex situ* analysis is presented of the system.

Investigation of the Differences in Passivation Mechanisms of Neat and Additive-Containing Electrolytes

In Chapter 4, the investigation from Chapter 3 is extended to lower passivating potentials that are more practical in lithium-ion battery operation. Glassy carbon is passivated at 0.3 V and 0.1 V *vs.* Li/Li^+ in neat and additive-containing electrolytes. Passivation curves are combined with impedance spectra to analyze if the benefits of additives are ever obtained in this system. Additionally, the adsorption of ferrocene is found to influence the impedance response. The results suggest that, over the potential ranges investigated, ferrocene does not behave analogously to solvent molecules.

A Physics-Based Model of the Impedance Response of a Graphite|LiNMC Cell

In Chapter 5, the investigation of electrode passivation is continued. A mathematical model of the impedance response of a real lithium-ion battery is presented. The model is used to investigate the role of surface film formation on the particles of the cathode

Summary and Recommendations

In Chapter 6, conclusions from Chapters 3, 4, and 5 are summarized. Recommendations for future work are given.

CHAPTER 2

BACKGROUND

Components and Features of Lithium-Ion Batteries

Rechargeable lithium-ion batteries (LiBs) are the premier energy storage devices for a wide variety of mobile and stationary devices (1). The popularity of LiBs results from their high energy densities, theoretical capacities, environmentally friendly components, potentially low costs, and long cycling life (2). Generally, a LiB consists of a positive electrode (cathode during discharge) and negative electrode (anode during discharge) separated by a porous film to prevent contact of the electrodes (2). The positive and negative electrodes are composite materials that include particles, electrolyte, conductive additives, and binder. At the ends of the cell are metallic current collectors that are in contact with the particles of the porous electrodes. Figure 2.1 is an illustration of the major components of a LiB.

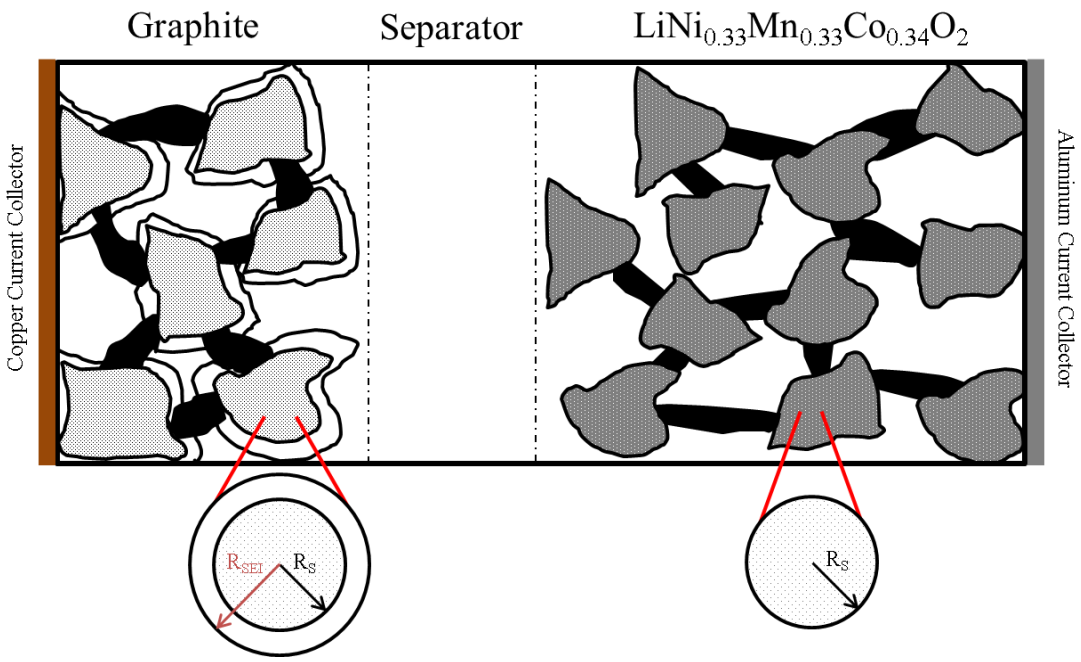

Figure 2.1. Illustration of the components of a LiB.The composite negative electrode shows a surface film enveloping the electrode particles.

The electrodes are made porous to increase the interfacial areas between electrolyte and active material and to reduce the diffusion length in the solid, thus allowing greater utilization of material (3). The electrode particles range from the nanoscale to the microscale in size. The electrolyte, which contains a dissolved lithium salt, fills the pores of the electrodes and separator and transports lithium ions between the electrodes. Lithium ions then react at the particle surface and intercalate into the particle. The electrolyte phase is an insulator to electrons. Current is passed by the transport of ions in the electrolyte phase. Electronic current passes through an external circuit.

An enlarged illustration of the electrode particles is shown in Figure 2.1. At the negative electrode, a film forms during charging and discharging on the surface of the electrode particles. The film is a result of decomposition reactions occurring between

lithium, electrons, and the electrolyte solvent. The products of the reactions lead to the formation of insoluble species that precipitate onto the surface of the particle. This surface film is referred to as the solid electrolyte interphase (SEI) (4). The SEI is a primary mode of lithium-ion battery degradation, leading to eventual failure (5-7).

Commercial carbonaceous materials, graphitic and hard carbons, are the most frequently used negative electrode materials (8). Lithium titanate oxide (LTO) is an alternative to graphitic and hard carbons but has drawbacks in its relatively low energy density. Alloying materials, those that compound phases with lithium, are promising materials due to their high theoretical gravimetric capacities. Examples of these materials include silicon, tin, and germanium. However, for widespread adoption of these materials, several challenges both cost related and scientific must be overcome (9). Positive electrode materials include layered $LiCoO_2$, spinel structured $LiMn_2O_4$, olivine structured $LiFePO_4$, and tavorite structured $LiFeSO_4F$ (10-13). Each of these materials has a different specific capacity (Ah/g), specific energy (Wh/g), cycle stability, and safety limitations, which are used to select the materials that best meet the requirements of the application (14).

Capacity Fade

Despite having drastically improved in quality since their inception, LiBs are still prone to capacity fade. The action of capacity fade refers to the loss of charge and discharge capacity with time. Figure 2.2 shows the charge capacity of a $LiNi_{0.8}Co_{0.15}Al_{0.05}O_2$ (LiNCA)|graphite cell, cycled at a C/30 rate with respect to the negative electrode. In this case, a cycle represents the action of charging and discharging

graphite, within the confines of the upper and lower potential charge and discharge limits. The charge capacity of the cell decreases with increasing cycle number, illustrating the action of capacity fade. The sharp decline from cycle 1 to cycle 2 is primarily a result of SEI formation. For this particular battery, the subsequent decline in charge capacity has a slope of approximately 4.4 mAh-g^{-1} per cycle. However, this slope is not unique and depends on the degradation processes occurring within the cell, both during operation (cycle life losses) and during periods of inactivity (calendar life losses) (15).

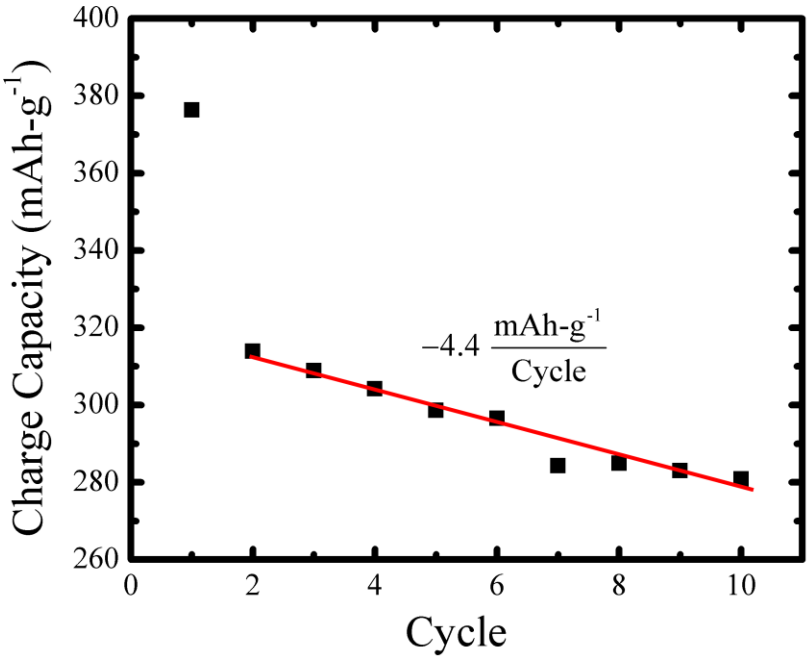

Figure 2.2. Charge capacity of $LiNi_{0.8}Co_{0.15}Al_{0.05}O_2$|graphite cell. When charging the cell, lithium is inserted into the graphite negative electrode particles. A cycle represents the action of charging and discharging graphite with respect to constant cut-off voltages. The charge capacity of the cell decreases with increasing cycle number, illustrating the action of capacity fade.

Eventually, capacity fade renders batteries inoperable, and accurate prediction of the battery's end of life (EOL) has proven to be a difficult. To understand the degradation processes leading to EOL, experimental data are needed that can be analyzed in such a way as to uniquely separate the causes of degradation within the cell. In most cases, there are only limited data on capacity fade available over extended periods of time. For example, satellite batteries are expected to stay in operation for a decade or more. However, testing cells to ensure they last for a decade is problematic. Not only are these tests extraordinarily costly, but they do not allow battery suppliers to keep pace with new materials development. Thus, a large lag develops between the qualified batteries and the state-of-the-art cells used in commercial applications. In extreme cases, suppliers no longer manufacture the materials that took ten years to qualify. Consequently, there is a strong incentive to shorten the qualification time for new materials and new batteries. The only options are to simultaneously develop accelerated tests and physics-based models to ensure long-term battery operation.

Accelerated Testing

Accelerated testing has many advantages with the most obvious being a reduction of costs through the development of less time consuming experimental techniques. Series of accelerated aging tests have been developed to quantify battery performance (16). Unfortunately, there are limitations to such tests, as imposing harsh testing conditions on the cell can unintentionally change the degradation mechanisms being studied. These limitations are mitigated with physics-based models that reliably simulate the charge-discharge behavior of a cell under the proposed conditions of operation. For

such a model only a limited, but high fidelity, experimental data set is needed to extract important model parameters and trends. More rigorous models allow for better prediction of battery lifetime but typically require more experimental parameters.

In the case of lithium-ion batteries, development of a more rigorous model requires integrating as many of the causes of capacity fade as possible. These models therefore require incorporating thermodynamics, mass-transport, and reactions kinetics with reliable parameter inputs. Indeed, mathematical models are useful in that they allow a variety of tests to be performed on a given electrochemical system without the overburdening need of having years of experimental data.

Causes of Capacity Fade

Identifying degradation mechanisms is the first step towards developing high fidelity models. The literature is well developed in identifying these degradation mechanisms that lead to capacity fade (15, 17). Arora *et al.* provide a thorough summary of the causes of capacity fade in LiBs (18). Several major causes to capacity fade are provided. In particular, capacity fade has been known to result from lithium deposition in the negative electrode due to overcharge, self-discharge of the cell at the cell open-circuit potential, current collector film formation and corrosion, active material dissolution, and SEI formation and growth.

Overcharge is a condition in which more lithium intercalates into the electrode than optimally desired. Overcharge can occur for negative graphitic electrodes (19) and high voltage positive electrodes (20) leading to unwanted side reactions. The side

reactions consume electrolyte, cause active material loss, and can potentially lead to the formation of undesired gases and subsequent electrode degradation.

Self-discharge refers to a spontaneous reduction of the open-circuit cell potential, which is measured during cell inactivity (18). Guyomard *et al.* described the capacity fade due to self-discharge as either reversible or irreversible (21). Capacity losses recovered when recharging the cell are reversible. Irreversible capacity losses are not recovered by recharging the cell. Johnson *et al.* performed capacity retention tests by continuously charging and discharging the cells and holding the cells at the open-circuit voltage condition and measuring the drop in the initial cell capacity (22). For the open-circuit potential tests, they held commercial Sony and Matsushita cells at an open-circuit potential for 30 days at ambient temperature conditions after measuring the initial cell capacity. On subsequent discharge after the 30 day voltage hold, they found a 3% reduction in the initial cell capacity. They concluded that for the given commercial cells, the capacity losses due to self-discharge were insignificant. No discussion was provided on whether the capacity loss was recovered after recharging the cells.

Current collector film formation and corrosion increase the internal impedance of the cell, leading to an increase in cell polarization and capacity fade (23). Copper and aluminum are common materials used as negative and positive electrode current collectors, respectively. The current collectors must adhere to the electrode active material. The loss of this adherence from corrosion indirectly leads to capacity fade, as the current collector might separate from the electrode active material causing an increase in cell impedance. Braithwaite *et al*. studied the differences in corrosion and passive

surface film formation on aluminum and copper current collectors immersed in $LiPF_6$ electrolyte based solution (24). They found no significant difference in the surface films formed on either material. However, they did find that aluminum was susceptible to pitting corrosion and copper was susceptible to environmentally assisted cracking.

Active material dissolution is known to lead to capacity fade in lithium ion cells. Dissolution is material specific, temperature dependent, and can be traced back to three sources (18). First, structural defects of oxygen in the active material at the positive electrode can cause oxygen-transition metal bonds to weaken, allowing for dissolution and subsequent capacity fade. Much interest has been taken into investigating the dissolution of manganese from LiNMC, a high voltage positive electrode material (25-27). Joshi *et al.* dissolved a low concentration of manganese into the electrolyte of a LiNMC|graphite cell (28). They observed that dissolved manganese in the electrolyte phase increased the growth rate of the SEI on graphite, ultimately accelerating capacity fade. Second, high charging potentials can cause the same type of bond weakening. Third, carbon from the binding material in the positive electrode active solid matrix can catalyze active material dissolution. Pieczonka *et al*. found that high voltage positive electrode spinel material dissolution rates increased with increasing temperature for prolonged storage periods by performing analytical measurements of the solution concentration (29).

Finally, the importance of the SEI towards capacity fade cannot be understated. The SEI is the primary mode of degradation in the negative electrode. SEI formation is a consequence of electrolyte reduction over the course of negative electrode charge and

discharge (4, 30). The electrolyte reaction means a loss of cyclable lithium ions, the same ions that govern cell energy density (7, 31). However, the SEI is a necessary mode of degradation. Without the SEI, solvent molecules would freely intercalate into the particle, causing particle exfoliation (32-34). Effectively, the SEI can have both beneficial and detrimental effects on the performance of a LiB.

The Characterization of the Solid Electrolyte Interphase

Martin Winter has stated that the SEI is "the most important and least understood solid electrolyte in rechargeable Li batteries" (6). SEI formation and growth is dependent on a number of factors that are not limited to the electrode composition and geometry, the electrolyte composition, and the potential of formation. Generally, the SEI forms due to side reactions between electrode particles and neighboring electrolyte as the electrode potential is far removed from open-circuit conditions. These reactions lead to the precipitation and deposition of soluble and insoluble reaction products on the particle surfaces (35, 36). In an ideal scenario, these initial films will prevent access of solvent to the electrode particles surfaces. However, the ideal scenario is not the case, and film growth does occur over the lifetime of the cell (37). Additionally, SEI formation reactions have also been linked to gas evolution at negative and positive electrodes, further accelerating capacity fade (38-40).

Characterization of the SEI requires the investigation of composition and structure, formation mechanisms, and time dependent thickness. Several groups have studied the film composition of the common carbon materials and lithium foil used as negative electrodes. Tsubouchi *et al.* used atomic force microscopy, ER-FTIR, and XPS

to analyze SEI formed on planar graphite. They found that in 1 mol-dm^{-3} $LiClO_4$/EC+DEC electrolyte solution the primary reaction products formed were $LiOCO_2R$, Li_2CO_3, $(CH_2CH_2O)_n$, Li_2O and LiCl (41). Murakami *et al.* identified the presence of LiF as a major byproduct for a $LiCoO_2$ positive electrode, Li negative electrode cell with $LiPF_6$ salt by NMR spectroscopy (42). Structurally, groups have suggested the existence of a multilayer SEI (4, 5, 32, 43, 44). Outer and inner layers are distinguished by composition. For example, Edstrom *et al.* used XPS and synchrotron-based PES to identify the outermost layer of the SEI. The components of this SEI tended to be organic. Additionally, they concluded that previous reports of Li_2O formed on the SEI were an experimental artifact. Their work did confirm the existence of LiF as a major byproduct of electrolyte decomposition (45).

Stoichiometric expressions are useful in describing film formation mechanisms. von Socken *et al.* studied the thermal stability of cells containing graphite positive electrode and lithium negative electrode cells during accelerated rate calorimetry testing (46). Note that thermal runaway is another failure mechanism under which abusive conditions can lead to excessive heating of the cell and eventually temperatures above the critical operating temperature of the cell. von Socken *et al.* found from the results of their study that the best way to explain solvent reduction was through the stoichiometric reaction between graphite and the electrolyte solution (S) as

$$Li_xC_6 + zS \rightleftharpoons Li_{x-z}C_6 + zLiS, \tag{2.1}$$

where *z* is the stoichiometric coefficient. Several types of stoichiometric expressions have been hypothesized in the literature, primarily from film composition determination.

SEI thicknesses have been measured by analytical imaging techniques and reported by groups in the literature. Cresce *et al.* reported film thicknesses by atomic force microscopy measurements for various additives on an HOPG negative electrode (47). Thickness was governed by the type of additive used and ranged from *ca.* 1 to 1000 nm. Lee *et al.* used XPS based low energy induced ion etching to measure the thicknesses of both porous and dense layers of the SEI for a graphite negative electrode. Based on their measurements, the porous layer thickness ranged from 20 to 30 nm and the dense layer from 10 to 15 nm (48). Bordes *et al.* measured film thicknesses for silicon-graphene composite negative electrodes using focused ion beam – scanning electron microscopy (FIB-SEM) imaging (49). SEI thicknesses were reported to be 30 to 50 nm with fluoroethylene carbonate (FEC) additive.

As previously mentioned, porous graphitic electrodes are the most common and commercially used negative electrode materials. The SEIs on these electrodes have been well investigated, both experimentally and mathematically (50-53). However, the analysis of porous electrodes is complicated by heterogeneity in structure and difficult-to-measure physical parameters. More informative studies on the structure and composition of carbonaceous electrodes have used planar electrodes.

Using Planar Electrodes to Investigate the Formation and Growth of the SEI

Planar electrodes are used to investigate the structure and properties of SEIs because of their simplicity. On planar electrodes, surface areas are easily measured, and unknown heterogeneity in composition and structure do not complicate analysis.

Therefore, the enhanced analytical ability gained with planar electrodes offsets that the materials used are only model, laboratory materials.

The most commonly investigated carbonaceous planar electrode material is highly oriented pyrolytic graphite (HOPG) and can be envisioned as a model, planar form of porous graphite. The material has two intercalation sites, basal-plane sites and edge-plane sites, and isolation of these sites for analytical investigation is the primary use of HOPG. In 1983, Yazami and Touzain first showed lithium intercalation into graphite in the presence of a solid polymer electrolyte as a method to store electrochemical energy (54). They used potentiostatic and galvanostatic intermittent titration to determine the diffusivity of lithium into graphite in the system. Additionally, cyclic voltammograms (CV) of the electrolyte indicated the presence of different stages of intercalation into lithium, a necessary technique to investigate the thermodynamics of lithium insertion. Funabiki *et al.* isolated the basal planes from the entirety of an HOPG electrode to investigate lithium intercalation (55). They used cyclic voltammetry to measure the current response of the basal plane in comparison to both basal and edge-plane sites. The basal plane current response was shown to be much muted in comparison to the edge plane response. Impedance spectroscopy supported their voltammogram measurements, confirming that the insertion kinetics were indeed slower at the basal plane. Hirasawa *et al.* extended these studies to investigate SEI formation on HOPG in 1:1 (vol) ethylene carbonate: ethylmethyl carbonate with 1 M $LiClO_4$ with *in situ* atomic force microscopy and frictional force microscopy (56). Following charging and discharging of the HOPG electrode, they found that reduction began on the cleaved portions of the HOPG surface starting at 2 V *vs.* Li/Li^+, suggesting high potential formation of the SEI on edge sites.

On the basal plane, the presence of an *ca.* 50 nm surface film was observed. The film remained stable after the open-circuit potential of the cell was increased to 3 V *vs.* Li/Li^+. Surprisingly, at these very positive potentials, the film was expected to oxidize and stripped from the surface. Yamada *et al.* extended the work of Hirasawa to investigate the role of the quantity of edge sites exposed on the basal plane and lithium intercalation kinetics (57). In the process of their investigation, they induced the formation of an SEI. They inferred the high frequency portion of their impedance responses suggested a time constant associated with transport through the SEI. Because the arc width of the high frequency portion of the response remained constant with increasing edge sites, the authors concluded that the number of edge sites did not affect SEI growth. We note that for the given surface area of the exposed electrode (*ca.* 1 cm^2), assuming an arc width of 20 Ω-cm^{-2} and characteristic frequency of 5 kHz, the capacitance associated with such an SEI would need to be on the order of *ca.* 1 □F-cm^{-2}. The magnitude of such a capacitance is typically associated with the double layer in organic electrolytes. Therefore, we suspect it is unlikely that the time constant that was observed was associated with the SEI. Tang *et al.* investigated the electronic passivity of HOPG after SEI formation using a model redox shuttle. They observed that the fluorinated anion, PF_6^-, a typical component of battery electrolytes, accelerated the oxidative stripping of the SEI (58, 59).

More recently, planar, glassy-carbon electrodes have been used as model electrodes for the investigation of SEI formation and growth (37, 44, 60). Because these materials are carbonaceous and are used as additives in LiBs, they are still relevant materials to use for basic research. Glassy-carbon electrodes are unique in that they have

negligible intercalation of lithium ions (61). Rather, glassy-carbon electrodes only form an SEI (60). Much of the focus of this particular work is towards the investigation of the physical properties of SEIs formed on glassy carbon.

Chemical Additives for Improved Battery Performance

Electrolyte additive co-solvents are an inexpensive way of ensuring capacity retention in LiBs (62). Examples of these co-solvents include fluoroethylene carbonate (FEC), vinylene carbonate (VC), and ethylene sulfide (ES) (62). The additives are introduced as co-solvents to the primary electrolyte, accounting for 10 % or less of the total electrolyte weight. Despite only accounting for a small fraction of the weight of the cell, additives have been shown to aid in improving cycling performance and reducing capacity fade as compared to systems without additives (63). The primary function of the additive is to form the SEI during formation cycling. The additive is selected so that, during formation cycling, the additive reduces on the electrode surface instead of the primary electrolyte. Typically, capacity retention improves as a result of incorporating the additive co-solvent in the primary electrolyte. The improved capacity retention has been shown to result from less gas generation within the cell, reduced formation cycle irreversible capacity losses, enhanced transport properties, and improved safety (62). Counterintuitively, additive formed SEIs tend to produce thinner SEIs than neat electrolyte (30, 49, 64). In some cases, a sharp contrast in performance is observed when comparing neat and additive-containing electrolytes. For example, Burns *et al.* experimentally measured that additives in the systems that they investigated extended battery lifetime by an order of magnitude (65). In other cases, experimental studies were

supported by model findings. For example, Jeong *et al.* measured the capacity retention of graphite negative electrodes in propylene carbonate solvent for cells with multiple additives. They measured cells with vinylene carbonate, FEC, and ethylene sulfite as co-solvents improved capacity retention. The improved capacity retention was attributed to a decline in solvent reduction and a reduction in graphite exfoliation, as compared to a neat electrolyte (66). Wang *et al.* used density functional theory calculations to find that the VC is more likely to be reduced than ethylene carbonate solvent, supporting the findings of Jeong *et al.* (67).

Mathematical Modeling of LiBs

SEI Models - SEI film formation and growth is a common degradation mechanism addressed in porous electrode models (4, 68-70). The most widespread models are based on solvent reduction mechanisms. Peled proposed the first major solid electrolyte interphase model for non-aqueous battery systems (4). During initial formation, SEI growth was proposed to be limited by electron tunneling ranges. After tunneling distances were exceeded, SEI growth was assumed to be limited by the migration or diffusion of electrons. Two SEI growth rate expressions were derived based on these two electron transport mechanisms. Both expressions resulted in SEI thickness scaling with the square root of time. Ploehn *et al.* developed a similar semi-empirical growth model with the assumption of solvent diffusion and reaction at the particle surface (71). They similarly proposed an analytical relationship that suggested that the SEI growth rate scaled with the square root of time. Broussely *et al.* measured the moles of lithium lost as a function of time for cells stored under constant voltage conditions over the course of

a year. They found experimental evidence to suggest that the cyclable lithium loss rate was proportional to the square root of time. They proceeded to derive a semi-empirical expression, based on the experimental findings, which supported the experimental outcome (68). More specifically, models have been developed strictly studying the SEI that aim to understand the development of concentration profiles of mobile species and predict growth rates of the surface film. The foundations of the more recent models that address lithium ion batteries, however, are from those developed for other electrochemical systems. For example, Battaglia and Newman developed a model to track film growth for an iron/iron oxide film forming system (72). One-dimensional transport through the oxide film was considered through vacancies and defects. Transport of electrons and holes was accounted for in the film, thereby defining the film as a semiconductor. Christiansen *et al.* extended Battaglia's model to predict SEI growth rates at graphitic negative electrodes (73). This model incorporated the irreversible decomposition reaction of solvent to form insoluble product on the graphite surface. Material and charge balances were solved in the SEI film, giving concentration profiles of species within the film. The model hypothesizes that only a small fraction of the film contains defects, and it is through these defects that species transport occurs. The assumption allowed the use of dilute solution theory to calculate the fluxes of each of the transporting species. This model required assuming known kinetics for SEI formation, which included reactions and rate constants. Colclasure *et al.* expanded on Christiansen's model to include SEI growth rate over the course of cycling (69). However, Colclasure's model is still limited in its assumption that the SEI has a constant density, which has been proven to be inaccurate in much of the literature. Recently, there has been a strong

agreement in LiB literature of the existence of two layers of the surface film that result from the decomposition of electrolyte solution at the particle surface (43, 69, 70). It has been proposed that the dense layer forms adjacent to the solid insertion material during initial cycles. The dense layer is sandwiched between the particle and the porous layer, which lies adjacent to the electrolytic solution phase.

Porous Electrode Models - A variety of electrochemical systems and electrode-electrolyte-film chemistries have been modeled based on the theory of porous electrodes. Fuller, Doyle, and Newman developed a dual lithium-ion insertion cell charge-discharge model that is extensively referenced in battery simulation literature (74, 75). This model allowed for an accurate prediction of the capacity of a cell based on the chemistry of the electrodes. From the dual lithium-ion insertion cell model, models that include capacity fade mechanisms have been presented in the literature. Sponitz has presented a review of capacity fade models (15). In the review, the current models are divided into those that include irreversible capacity loss to SEI growth, those that include irreversible and reversible capacity loss to SEI growth, and those that include irreversible and reversible capacity loss due to SEI growth and dissolution of active material.

Impedance Response Models - As discussed earlier, a wide array of *ex situ* analytical techniques have been used in the literature to study the causes of capacity fade in lithium ion batteries. In contrast, electrochemical impedance spectroscopy (EIS) has been used extensively as an *in situ* and non-destructive experimental method in the general study of electrochemical systems. EIS is useful in developing reaction

mechanisms, measuring electrode transport properties for both planar and porous electrodes, and studying passive film formation and growth in electrodes (76, 77).

There are two techniques used to model the impedance response of a LiB. The first technique, and most common method, is to develop an equivalent circuit representation of the system. For example, Yang *et al.* investigated the SEI that forms on mesocarbon microbead electrodes using an organic electrolyte (78). Their results suggested differences in the total resistances of single versus binary solvents, with resulting spectra fitted to an RLC network composed of five semicircles. Each of these semicircles represented different physical processes within the cell. Gnanaraj *et al.* found the presence of an inductive loop at low frequencies which they attributed to a leak current flowing in opposition to the expected direction of current on charging the cell (from the solution to the graphite electrode). They present an RLC circuit modified to account for this inductive effect that is described to fit the data well (79). Peled *et al.* formulated an equivalent circuit model that accounted for grain boundaries in the solid electrolyte interphase (due to a variety of decomposition products) (5). His work suggested that the grain boundaries contributed significantly to the overall resistance and capacitance of the surface film.

The second technique is to represent the electrochemical system with a physics-based model. The model is based on the porous electrode models discussed earlier. However, in most cases, the porous electrode equations are transferred from the time domain to the frequency domain (80-86). Doyle *et al.* modeled the impedance response of a dual-lithium ion insertion cell (87). The modeling technique took the transient

porous electrode model equations, applied sinusoidal perturbations to each of the modeled variables around the open-circuit potential in the system, and simulated the response over 11 orders of magnitude of frequency. The response to the perturbation was assumed to be linear and around a steady state. These assumptions are an obvious limitation to the model as the response limitation does not allow full replication of experimental conditions. That is, larger amplitude voltage perturbations that provide non-linear responses are not able to be modeled. Even so, the work was useful in explaining the potential for time constant overlap in impedance spectra. More particularly, the authors provided a thorough discussion on the pitfalls of using impedance data to calculate diffusion coefficients. Several other porous electrode models have been put forth in the literature (81, 82, 84, 88). These models attempt to explain impedance data in much the same way as the model of Doyle *et al.* and have given a new perspective on LiB impedance spectra.

Modeling of Capacitive Processes – Unlike the capacity fade models previously discussed, capacitive processes are an integral component of an impedance response model. Any capacitive process contributes to the magnitude of the imaginary component of the impedance response. However, the impedance response of capacitive processes in impedance spectra can rarely be represented by ideal capacitors. As expected, a circuit element for non-ideal capacitive process has been created to address this situation. The circuit element is referred to as a constant phase element (CPE). Several groups have hypothesized the causes of the representation of the ideal capacitor with a constant phase element (89-92). Rammelt *et al.* showed that by exposing iron electrodes to acidic solution, semicircle depression occurred due to surface roughness (93). Surface

heterogeneity and a distribution of charge-transfer resistances at the electrode surface has been mentioned in the literature (94, 95). Distributed dielectric properties for surface films has also been suggested as a potential cause (90). In porous electrodes, this effect is more common at high frequencies due to the fixed thickness of the electrode causing poor electrode utilization at high frequencies (96). The Warburg impedance element has been created to address semi-infinite diffusion and is also termed a constant phase element.

In the next chapter, we build on the previous planar-electrode SEI investigations in the literature. We use a planar, glassy-carbon electrode to investigate the causes of differences in the passivation character of SEIs formed with neat and additive-containing electrolytes. From our review of LiB literature, a thorough understanding of the differences between passivation characteristics between neat and additive-containing electrolytes is still lacking and is of fundamental concern for the future improvement of LiBs.

References

1. Tarascon, J.M. and M. Armand, *Issues and challenges facing rechargeable lithium batteries.* Nature, 2001. 414(6861): p. 359-367.
2. Goodenough, J.B. and K.-S. Park, *The Li-Ion Rechargeable Battery: A Perspective.* Journal of the American Chemical Society, 2013. 135(4): p. 1167-1176.
3. Newman, J.S., *Electrochemical systems*. 3rd ed.. ed, ed. K.E. Thomas-Alyea. 2004, Hoboken, N.J.: Hoboken, N.J. : J. Wiley.
4. Peled, E., *The electrochemical behavior of alkali and alkaline earth metals in nonaqueous battery systems—the solid electrolyte interphase model.* Journal of the Electrochemical Society, 1979. 126(12): p. 2047-2051.
5. Peled, E., D. Golodnitsky, and G. Ardel, *Advanced Model for Solid Electrolyte Interphase Electrodes in Liquid and Polymer Electrolytes.* Journal of the Electrochemical Society, 1997. 144(8): p. L208-L210.
6. Winter, M., *The Solid Electrolyte Interphase – The Most Important and the Least Understood Solid Electrolyte in Rechargeable Li Batteries*, in *Zeitschrift für Physikalische Chemie International journal of research in physical chemistry and chemical physics*2009. p. 1395.
7. Verma, P., P. Maire, and P. Novák, *A review of the features and analyses of the solid electrolyte interphase in Li-ion batteries.* Electrochimica Acta, 2010. 55(22): p. 6332-6341.
8. Etacheri, V., et al., *Challenges in the development of advanced Li-ion batteries: a review.* Energy & Environmental Science, 2011. 4(9): p. 3243-3262.

9. Nitta, N., et al., *Li-ion battery materials: present and future.* Materials Today, 2015. 18(5): p. 252-264.

10. Thackeray, M.M., et al., *Lithium insertion into manganese spinels.* Materials Research Bulletin, 1983. 18(4): p. 461-472.

11. Wang, B., et al., *Characterization of Thin-Film Rechargeable Lithium Batteries with Lithium Cobalt Oxide Cathodes.* Journal of the Electrochemical Society, 1996. 143(10): p. 3203-3213.

12. Padhi, A.K., K.S. Nanjundaswamy, and J.B. Goodenough, *Phospho-olivines as Positive-Electrode Materials for Rechargeable Lithium Batteries.* Journal of the Electrochemical Society, 1997. 144(4): p. 1188-1194.

13. Sobkowiak, A., et al., *Understanding and controlling the surface chemistry of LiFeSO4F for an enhanced cathode functionality.* Chemistry of Materials, 2013. 25(15): p. 3020-3029.

14. Ellis, B.L., K.T. Lee, and L.F. Nazar, *Positive Electrode Materials for Li-Ion and Li-Batteries.* Chemistry of Materials, 2010. 22(3): p. 691-714.

15. Spotnitz, R., *Simulation of capacity fade in lithium-ion batteries.* Journal of Power Sources, 2003. 113(1): p. 72-80.

16. Ecker, M., et al., *Development of a lifetime prediction model for lithium-ion batteries based on extended accelerated aging test data.* Journal of Power Sources, 2012. 215(0): p. 248-257.

17. Vetter, J., et al., *Ageing mechanisms in lithium-ion batteries.* Journal of Power Sources, 2005. 147(1–2): p. 269-281.

18. Arora, P., R.E. White, and M. Doyle, *Capacity fade mechanisms and side reactions in lithium-ion batteries.* Journal of the Electrochemical Society, 1998. 145(10): p. 3647-3667.

19. Fong, R., U. von Sacken, and J.R. Dahn, *Studies of Lithium Intercalation into Carbons Using Nonaqueous Electrochemical Cells.* Journal of the Electrochemical Society, 1990. 137(7): p. 2009-2013.

20. Dahn, J.R., et al., *Thermal stability of LixCoO2, LixNiO2 and λ-MnO2 and consequences for the safety of Li-ion cells.* Solid State Ionics, 1994. 69(3–4): p. 265-270.

21. Guyomard, D. and J.M. Tarascon, *The carbon/Li1+xMn2O4 system.* Solid State Ionics, 1994. 69(3–4): p. 222-237.

22. Johnson, B.A. and R.E. White, *Characterization of commercially available lithium-ion batteries.* Journal of Power Sources, 1998. 70(1): p. 48-54.

23. Zhang, X., et al., *Corrosion of Aluminum Current Collectors in Lithium-Ion Batteries with Electrolytes Containing LiPF6.* Journal of the Electrochemical Society, 2005. 152(11): p. B448-B454.

24. Braithwaite, J.W., et al., *Corrosion of Lithium-Ion Battery Current Collectors.* Journal of the Electrochemical Society, 1999. 146(2): p. 448-456.

25. Aoshima, T., et al., *Mechanisms of manganese spinels dissolution and capacity fade at high temperature.* Journal of Power Sources, 2001. 97–98: p. 377-380.

26. Lu, J., et al., *Effectively suppressing dissolution of manganese from spinel lithium manganate via a nanoscale surface-doping approach.* Nature Communications, 2014. 5: p. 5693.

27. Esbenshade, J.L. and A.A. Gewirth, *Effect of Mn and Cu Addition on Lithiation and SEI Formation on Model Anode Electrodes*. Journal of the Electrochemical Society, 2014. 161(4): p. A513-A518.

28. Joshi, T., et al., *Effects of Dissolved Transition Metals on the Electrochemical Performance and SEI Growth in Lithium-Ion Batteries.* Journal of the Electrochemical Society, 2014. 161(12): p. A1915-A1921.

29. Pieczonka, N.P.W., et al., *Understanding Transition-Metal Dissolution Behavior in LiNi0.5Mn1.5O4 High-Voltage Spinel for Lithium Ion Batteries.* The Journal of Physical Chemistry C, 2013. 117(31): p. 15947-15957.

30. Nie, M., et al., *Effect of Vinylene Carbonate and Fluoroethylene Carbonate on SEI Formation on Graphitic Anodes in Li-Ion Batteries.* Journal of the Electrochemical Society, 2015. 162(13): p. A7008-A7014.

31. Bryngelsson, H., et al., *How dynamic is the SEI?* Journal of Power Sources, 2007. 174(2): p. 970-975.

32. Aurbach, D., et al., *On the use of vinylene carbonate (VC) as an additive to electrolyte solutions for Li-ion batteries.* Electrochimica Acta, 2002. 47(9): p. 1423-1439.

33. Aurbach, D., et al., *Failure and Stabilization Mechanisms of Graphite Electrodes.* The Journal of Physical Chemistry B, 1997. 101(12): p. 2195-2206.

34. Aurbach, D., et al., *On the correlation between surface chemistry and performance of graphite negative electrodes for Li ion batteries.* Electrochimica Acta, 1999. 45(1–2): p. 67-86.

35. Soto, F.A., et al., *Formation and Growth Mechanisms of Solid-Electrolyte Interphase Layers in Rechargeable Batteries.* Chemistry of Materials, 2015. 27(23): p. 7990-8000.

36. Zhuang, G.V., et al., *A Study of Electrochemical Reduction of Ethylene and Propylene Carbonate Electrolytes on Graphite Using ATR-FTIR Spectroscopy.* Electrochemical and Solid-State Letters, 2005. 8(9): p. A441-A445.

37. Tang, M. and J. Newman, *Transient Characterization of Solid-Electrolyte-Interphase Using Ferrocene.* Journal of the Electrochemical Society, 2012. 159(3): p. A281-A289.

38. Goers, D., et al., *In situ neutron radiography of lithium-ion batteries: the gas evolution on graphite electrodes during the charging.* Journal of Power Sources, 2004. 130(1–2): p. 221-226.

39. Lanz, M. and P. Novák, *DEMS study of gas evolution at thick graphite electrodes for lithium-ion batteries: the effect of γ-butyrolactone.* Journal of Power Sources, 2001. 102(1–2): p. 277-282.

40. Kong, W.H., et al., *Gas evolution behaviors for several cathode materials in lithium-ion batteries.* Journal of Power Sources, 2005. 142(1-2): p. 285-291.

41. Tsubouchi, S., et al., *Spectroscopic Analysis of Surface Layers in Close Contact with Edge Plane Graphite Negative-Electrodes.* Journal of the Electrochemical Society, 2013. 160(4): p. A575-A580.

42. Murakami, M., et al., *Direct Evidence of LiF Formation at Electrode/Electrolyte Interface by 7Li and 19F Double-Resonance Solid-State NMR Spectroscopy.* Electrochemical and Solid-State Letters, 2011. 14(9): p. A134-A137.

43. Shi, S., et al., *Direct Calculation of Li-Ion Transport in the Solid Electrolyte Interphase.* Journal of the American Chemical Society, 2012. 134(37): p. 15476-15487.

44. Tang, M. and J. Newman, *Electrochemical Characterization of SEI-Type Passivating Films Using Redox Shuttles.* Journal of the Electrochemical Society, 2011. 158(5): p. A530-A536.

45. Edström, K., M. Herstedt, and D.P. Abraham, *A new look at the solid electrolyte interphase on graphite anodes in Li-ion batteries.* Journal of Power Sources, 2006. 153(2): p. 380-384.

46. von Sacken, U., et al., *Comparative thermal stability of carbon intercalation anodes and lithium metal anodes for rechargeable lithium batteries.* Solid State Ionics, 1994. 69(3–4): p. 284-290.

47. Cresce, A.v., et al., *In Situ and Quantitative Characterization of Solid Electrolyte Interphases.* Nano Letters, 2014. 14(3): p. 1405-1412.

48. Lee, S.-H., et al., *A new approach to surface properties of solid electrolyte interphase on a graphite negative electrode.* Journal of Power Sources, 2014. 247(0): p. 307-313.

49. Bordes, A., K. Eom, and T.F. Fuller, *The effect of fluoroethylene carbonate additive content on the formation of the solid-electrolyte interphase and capacity fade of Li-ion full-cell employing nano Si–graphene composite anodes.* Journal of Power Sources, 2014. 257(0): p. 163-169.

50. Ota, H., et al., *Analysis of Vinylene Carbonate Derived SEI Layers on Graphite Anode.* Journal of the Electrochemical Society, 2004. 151(10): p. A1659-A1669.

51. Wang, C.S., A.J. Appleby, and F.E. Little, *Charge-discharge stability of graphite anodes for lithium-ion batteries.* Journal of Electroanalytical Chemistry, 2001. 497(1-2): p. 33-46.

52. Yazami, R. and Y.F. Reynier, *Mechanism of self-discharge in graphite–lithium anode.* Electrochimica Acta, 2002. 47(8): p. 1217-1223.

53. Zhang, S.S., et al., *Understanding solid electrolyte interface film formation on graphite electrodes.* Electrochemical and Solid State Letters, 2001. 4(12): p. A206-A208.

54. Yazami, R. and P. Touzain, *A reversible graphite-lithium negative electrode for electrochemical generators.* Journal of Power Sources, 1983. 9(3): p. 365-371.

55. Funabiki, A., M. Inaba, and Z. Ogumi, *A.c. impedance analysis of electrochemical lithium intercalation into highly oriented pyrolytic graphite.* Journal of Power Sources, 1997. 68(2): p. 227-231.

56. Hirasawa, K.A., et al., *In Situ Electrochemical Atomic Force Microscope Study on Graphite Electrodes.* Journal of the Electrochemical Society, 1997. 144(4): p. L81-L84.

57. Yamada, Y., K. Miyazaki, and T. Abe, *Role of Edge Orientation in Kinetics of Electrochemical Intercalation of Lithium-Ion at Graphite.* Langmuir, 2010. 26(18): p. 14990-14994.

58. Tang, M., et al., *Effect of Graphite Orientation and Lithium Salt on Electronic Passivation of Highly Oriented Pyrolytic Graphite.* Journal of the Electrochemical Society, 2012. 159(5): p. A634-A641.

59. Tang, M. and J. Newman, *Why is the Solid-Electrolyte-Interphase Selective? Through-Film Ferrocenium Reduction on Highly Oriented Pyrolytic Graphite.* Journal of the Electrochemical Society, 2012. 159(12): p. A1922-A1927.

60. Tang, M., S. Lu, and J. Newman, *Experimental and Theoretical Investigation of Solid-Electrolyte-Interphase Formation Mechanisms on Glassy Carbon.* Journal of the Electrochemical Society, 2012. 159(11): p. A1775-A1785.

61. Jaini, R.R., et al., *Investigating the Solid Electrolyte Interphase Formed by Additive Reduction Using Physics-Based Modeling.* Journal of the Electrochemical Society, 2016. 163(10): p. A2185-A2196.

62. Zhang, S.S., *A review on electrolyte additives for lithium-ion batteries.* Journal of Power Sources, 2006. 162(2): p. 1379-1394.

63. Markevich, E., et al., *Fluoroethylene Carbonate as an Important Component in Electrolyte Solutions for High-Voltage Lithium Batteries: Role of Surface Chemistry on the Cathode.* Langmuir, 2014.

64. Ryou, M.-H., et al., *Effect of fluoroethylene carbonate on high temperature capacity retention of LiMn2O4/graphite Li-ion cells.* Electrochimica Acta, 2010. 55(6): p. 2073-2077.

65. Burns, J.C., et al., *Predicting and Extending the Lifetime of Li-Ion Batteries.* Journal of the Electrochemical Society, 2013. 160(9): p. A1451-A1456.

66. Jeong, S.-K., et al., *Surface Film Formation on a Graphite Negative Electrode in Lithium-Ion Batteries: Atomic Force Microscopy Study on the Effects of Film-Forming Additives in Propylene Carbonate Solutions.* Langmuir, 2001. 17(26): p. 8281-8286.

67. Wang, Y., et al., *Theoretical Studies To Understand Surface Chemistry on Carbon Anodes for Lithium-Ion Batteries: How Does Vinylene Carbonate Play Its Role as an Electrolyte Additive?* Journal of the American Chemical Society, 2002. 124(16): p. 4408-4421.

68. Broussely, M., et al., *Aging mechanism in Li ion cells and calendar life predictions.* Journal of Power Sources, 2001. 97–98(0): p. 13-21.

69. Colclasure, A.M., K.A. Smith, and R.J. Kee, *Modeling detailed chemistry and transport for solid-electrolyte-interface (SEI) films in Li–ion batteries.* Electrochimica Acta, 2011. 58(0): p. 33-43.

70. Wang, C., A.J. Appleby, and F.E. Little, *Electrochemical impedance study of initial lithium ion intercalation into graphite powders.* Electrochimica Acta, 2001. 46(12): p. 1793-1813.

71. Ploehn, H.J., P. Ramadass, and R.E. White, *Solvent Diffusion Model for Aging of Lithium-Ion Battery Cells.* Journal of the Electrochemical Society, 2004. 151(3): p. A456-A462.

72. Battaglia, V. and J. Newman, *Modeling of a Growing Oxide Film: The Iron/Iron Oxide System.* Journal of the Electrochemical Society, 1995. 142(5): p. 1423-1430.

73. Christensen, J. and J. Newman, *A Mathematical Model for the Lithium-Ion Negative Electrode Solid Electrolyte Interphase.* Journal of the Electrochemical Society, 2004. 151(11): p. A1977-A1988.

74. Fuller, T.F., M. Doyle, and J. Newman, *Simulation and optimization of the dual lithium ion insertion cell.* Journal of the Electrochemical Society, 1994. 141(1): p. 1-10.

75. Doyle, M., T.F. Fuller, and J. Newman, *Modeling of Galvanostatic Charge and Discharge of the Lithium/Polymer/Insertion Cell.* Journal of the Electrochemical Society, 1993. 140(6): p. 1526-1533.

76. Macdonald, D.D., *Reflections on the history of electrochemical impedance spectroscopy.* Electrochimica Acta, 2006. 51(8–9): p. 1376-1388.

77. Randviir, E.P. and C.E. Banks, *Electrochemical impedance spectroscopy: an overview of bioanalytical applications.* Analytical Methods, 2013. 5(5): p. 1098-1115.

78. Yang, C.R., et al., *Impedance spectroscopic study for the initiation of passive film on carbon electrodes in lithium ion batteries.* Journal of Applied Electrochemistry, 2000. 30(1): p. 29-34.

79. Gnanaraj, J.S., et al., *Formation and growth of surface films on graphitic anode materials for Li-ion batteries.* Electrochemical and Solid State Letters, 2005. 8(2): p. A128-A132.

80. Chen, C.-F. and P.P. Mukherjee, *Probing the morphological influence on solid electrolyte interphase and impedance response in intercalation electrodes.* Physical Chemistry Chemical Physics, 2015. 17(15): p. 9812-9827.

81. Dees, D., et al., *Alternating current impedance electrochemical modeling of lithium-ion positive electrodes.* Journal of the Electrochemical Society, 2005. 152(7): p. A1409-A1417.

82. Dees, D.W., et al., *Electrochemical Modeling the Impedance of a Lithium-Ion Positive Electrode Single Particle.* Journal of the Electrochemical Society, 2013. 160(3): p. A478-A486.

83. Gambhire, P., et al., *Impedance Response Model of a Lithium Ion Cell with a Phase Change Electrode.* Journal of the Electrochemical Society, 2014. 161(1): p. A183-A193.

84. Huang, J., et al., *An Agglomerate Model for the Impedance of Secondary Particle in Lithium-Ion Battery Electrode.* Journal of the Electrochemical Society, 2014. 161(8): p. E3202-E3215.

85. Song, J. and M.Z. Bazant, *Effects of Nanoparticle Geometry and Size Distribution on Diffusion Impedance of Battery Electrodes.* Journal of the Electrochemical Society, 2013. 160(1): p. A15-A24.

86. Sunde, S., et al., *An Impedance Model for a Porous Intercalation Electrode with Mixed Conductivity.* Journal of the Electrochemical Society, 2009. 156(8): p. B927-B937.

87. Doyle, M., J.P. Meyers, and J. Newman, *Computer Simulations of the Impedance Response of Lithium Rechargeable Batteries.* Journal of the Electrochemical Society, 2000. 147(1): p. 99-110.

88. Mellgren, N., et al., *Impedance as a Tool for Investigating Aging in Lithium-Ion Porous Electrodes: I. Physically Based Electrochemical Model.* Journal of the Electrochemical Society, 2008. 155(4): p. A304-A319.

89. Shoar Abouzari, M.R., et al., *On the physical interpretation of constant phase elements.* Solid State Ionics, 2009. 180(14–16): p. 922-927.

90. Musiani, M., et al., *Constant-Phase-Element Behavior Caused by Coupled Resistivity and Permittivity Distributions in Films.* Journal of the Electrochemical Society, 2011. 158(12): p. C424-C428.

91. Orazem, M.E., et al., *Dielectric Properties of Materials Showing Constant-Phase-Element (CPE) Impedance Response.* Journal of the Electrochemical Society, 2013. 160(6): p. C215-C225.

92. Bisquert, J., et al., *Doubling Exponent Models for the Analysis of Porous Film Electrodes by Impedance. Relaxation of TiO2 Nanoporous in Aqueous Solution.* The Journal of Physical Chemistry B, 2000. 104(10): p. 2287-2298.

93. Rammelt, U. and G. Reinhard, *The influence of surface roughness on the impedance data for iron electrodes in acid solutions.* Corrosion Science, 1987. 27(4): p. 373-382.

94. de Levie, R., *Fractals and rough electrodes.* Journal of Electroanalytical Chemistry and Interfacial Electrochemistry, 1990. 281(1–2): p. 1-21.

95. Pajkossy, T., *Impedance of rough capacitive electrodes.* Journal of Electroanalytical Chemistry, 1994. 364(1–2): p. 111-125.

96. Devan, S., V.R. Subramanian, and R.E. White, *Analytical Solution for the Impedance of a Porous Electrode.* Journal of the Electrochemical Society, 2004. 151(6): p. A905-A913.

CHAPTER 3

INVESTIGATING THE SOLID ELECTROLYTE INTERPHASE FORMED BY ADDITIVE REDUCTION AT 0.6 V *VS.* LI/LI$^+$ USING PHYSICS-BASED MODELING

Introduction

In lithium-ion batteries, formation and growth of the solid electrolyte interphase (SEI) is a well-established mode of capacity and power fade (4, 6). Cell characteristics, including electrode chemistry and primary electrolyte composition, influence the chemical and physical properties of SEIs formed (28). In addition to the primary electrolyte, chemical additives have been incorporated as co-solvents to address SEI formation and growth. When included as co-solvents, both fluoroethylene carbonate (FEC) and vinylene carbonate (VC) electrolyte additives preferentially react with the electrode during the SEI formation process instead of the primary electrolyte. Improved capacity retention, calendar life, and thermal stability are observed with additive inclusion in the electrolyte mixture. Additives such as FEC and VC have been prescribed as co-solvents to primary electrolytes for a variety of electrode chemistries (30, 32, 63, 64, 97).

Several groups have investigated the efficacy of these co-solvents to enhance cell performance. In these studies, the additives are limited to less than or equal to ten weight percent of the total electrolyte. For example, Ryou *et al.* found improved capacity retention at 60 °C with the addition of FEC, for a graphite negative electrode and

$LiMn_2O_4$ positive electrode full cell (64). Bordes *et al.* found that, for a silicon-graphene composite negative electrode, FEC enhanced electrochemical performance by forming a less resistive SEI with smaller thickness using impedance spectroscopy and electron microscopy (49). Aurbach *et al.* observed improved capacity with the addition of VC to a graphite negative electrode, $LiMn_2O_4$ positive electrode full cell (32). Using infrared and x-ray photoelectron spectroscopy, they detected the formation of polymerized VC products on the negative electrode SEI. Nguyen *et al.* compared the cycling performance of silicon half cells in neat, FEC, and VC-containing electrolyte (97). After cycling, they found less cell impedance with FEC but increased cell impedance with VC compared to neat electrolyte.

Coupled with SEI functionality and electrochemical performance enhancement, SEI growth mechanics has been a well-investigated area of study. Polymerization and oligomerization have been shown to be a plausible mechanism by which the SEI grows. Several groups have investigated the role of SEI product distributions and composition by spectroscopic methods (98-100). Shkrob *et al.* used beam radiolysis to polymerize ethylene carbonate (EC) with masses of up to 2 kDa (101). They proposed that the morphology and composition of the radiolytically generated polymer was likely to occur in the SEI of graphitic systems. Tavassol *et al.* used matrix assisted laser desorption ionization time-of-flight mass spectrometry to determine the presence of oligomerized species on Au surfaces in multiple organic electrolyte solvents (100).

Selecting an electrode-electrolyte pairing to form an SEI also poses as a significant challenge due to the complex nature of porous electrodes and possibility of

inducing undesired degradation mechanisms during experimentation (17, 18). Capacity and power retention of porous electrodes on charge and discharge are prescribed as standard methods to evaluate additive effectiveness through both experiment and modeling (102, 103). However, the heterogeneity and difficult-to-measure physical properties of porous electrodes can lead to incorrect estimates of physical parameters. In addition to electrode complexity, experimental protocol can cause the onset of unintended capacity fade mechanisms during experimental testing. In contrast to porous electrodes, planar electrode systems offer the advantage of simplicity. SEI physical properties can be evaluated without the concern of the onset of competing degradation mechanisms. Additionally, quantities such as surface area are easily measurable, simplifying subsequent SEI analysis.

Several electrochemical techniques allow formation and analysis of the SEI. Cyclic voltammetry (CV) and electrochemical impedance spectroscopy (EIS) are two *in situ* techniques that are useful in exploring the properties of the SEI. Introduction of a species of known redox potential in dilute concentrations into the electrolyte can serve as an alternative method to *ex situ* techniques to investigate the characteristics of formed SEIs. Previously, Tang *et al.* used the ferrocene-ferrocenium redox couple to probe the physical structure and electronic passivity of the SEI (37, 44, 58). In this method, the redox couple is analogous to a solvent molecule. The thermodynamic potential of the redox couple (E^0 = 3.24 V *vs.* Li/Li^+) is outside of the potential window for SEI formation. Therefore, the redox couple allowed investigation of the SEI without the complication of significantly altering the structure of the SEI.

In this work, we investigate the differences in SEIs produced with and without additives using the ferrocene redox couple. SEIs formed with additives are known to be more effective in preventing capacity fade than neat electrolyte, while still being smaller in thickness. The relationship between capacity fade and thickness, however, is not intuitive. For additives to form thinner SEIs, they must compensate for the reduced thickness with more effective passivation to prevent solvent reduction. In such a scenario, higher diffusion or kinetic resistance is expected to be observed for ferrocene redox couple. Such observations would allow proposing if the passivation mechanisms for additive-containing electrolyte and neat electrolyte are unique. Therefore, the primary intention of this work is to elucidate the differences in the formation methods of these SEIs. From the outset, we assume that the kinetics and mass-transport of the ferrocene redox couple are analogous to solvent.

Model Development

In Figure **3.1**, an illustration of the electrode-electrolyte interface is provided. Model formulation is based off the work of Tang and Newman (37). The model assumes a single-layer film on the surface of the glassy-carbon electrode. The layer is porous and allows transport of ferrocenium cations and neutral ferrocene species through the electrolyte phase. Reduction of ferrocenium cations occurs at the electrode, porous-layer interface. The outermost layer of the model is the diffusion layer, where mass transport is governed by Fick's law. The parameters that are model inputs are diffusivities and bulk concentrations of the cation and neutral ferrocene species, kinetic parameters for the

redox reactions, double-layer capacitance, void fraction of the porous layer, tortuosity of the porous layer, and porous-layer thickness.

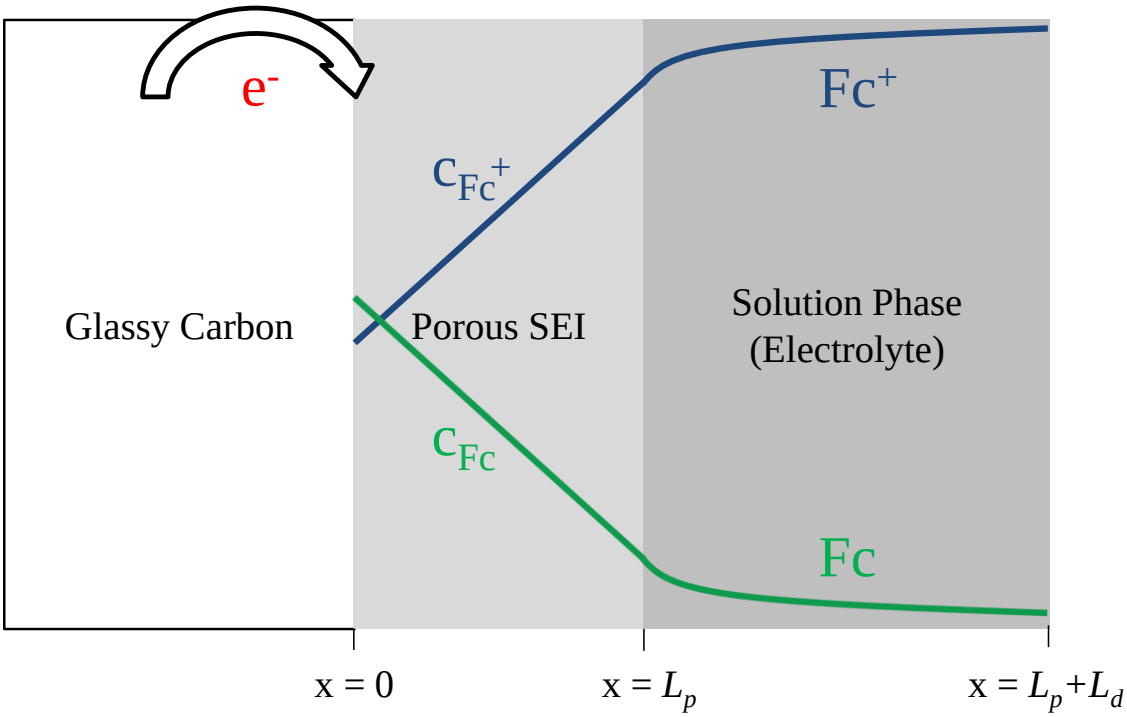

Figure 3.1. Illustration of electrode, SEI, and electrolyte (not to scale). L_p is the thickness of the porous SEI, and L_d is the thickness of the diffusion layer. A sample concentration profile is provided of a diffusing species, *s*. The diffusing species is solvent or redox couple.

Transient Model for Simulation of Cyclic Voltammetry

The working-electrode overpotential, η, with respect to a reference electrode away from the working electrode can be defined as

$$\eta = V - U - iR_e , \tag{3.1}$$

where V is the cell potential, U is the thermodynamic potential, i is the total current density, and R_e is the electrolyte resistance between the working and reference electrodes. The model accounts for faradaic and double-layer charging processes. Both double-layer charging and the faradaic reaction occur at the electrode-SEI interface. Because both processes allow current density to pass from the SEI into the glassy-carbon electrode, the current paths are summed to provide the total current density,

$$i = i_{far} + i_{dl}\,. \tag{3.2}$$

i_{far} is the faradaic current, i_{dl} is the double-layer charging current, and i is the total current density. The faradaic current is governed by Butler-Volmer kinetics

$$i_{far} = i_0 \left[\frac{c_r(0)}{c_{r,b}} \exp\left(\frac{\alpha_a F}{RT} \eta \right) - \frac{c_o(0)}{c_{o,b}} \exp\left(-\frac{\alpha_c F}{RT} \eta \right) \right], \tag{3.3}$$

where α_a and α_c, i_0 the exchange-current density, and η is the surface overpotential. We note that subscript r represents the reduced species, and o represents the oxidized species. The double-layer charging current is given as

$$i_{dl} = C_{dl} \frac{dV}{dt}, \tag{3.4}$$

where C_{dl} is the double-layer capacitance per unit area. Transport of redox couple species in the porous SEI is governed by 1-D diffusion. Because the electric field is small, migration as a transport mechanism across the SEI is neglected. The superficial flux, $N_{i,p}$, in the SEI is given by

$$N_{i,p} = -D_{i,eff}\frac{dc_{i,p}}{dx}, \tag{3.5}$$

where $D_{i,eff} = D_i\frac{\varepsilon_p}{\tau_p}$ is the effective diffusivity of species *i*. $c_{i,p}$ is defined as the in-pore concentration of species *i*. ε_p and τ_p are defined as the porosity and tortuosity of the SEI. The porosity and tortuosity are assumed to be defined by the Bruggeman relation,

$$\tau_p = \varepsilon_p^{-0.5}. \tag{3.6}$$

A material balance in the SEI leads to

$$\frac{\partial \varepsilon_p c_{i,p}}{\partial t} = D_{i,eff}\frac{\partial^2 c_{i,p}}{\partial x^2}. \tag{3.7}$$

At the electrode-SEI interface, the fluxes of the redox species are equal and opposite

$$N_{o,p}(0) = -N_{r,p}(0). \tag{3.8}$$

The faradaic current is related to the flux of electroactive species diffusing to the interface,

$$i_{far} = FN_{i,p}(0). \tag{3.9}$$

At the SEI-diffusion layer interface, the in-pore concentration and superficial fluxes are continuous,

$$c_{i,p} = c_{i,d} \;\; ; \;\; N_{i,p} = N_{i,d}. \tag{3.10}$$

Transport in the diffusion layer is treated with Equations (3.5) and (3.7), with all *p* subscripts changing to *d*. Additionally, $\varepsilon_d = \tau_d = 1$.

Simulation of Impedance Model

The transient model equations are transformed to simulate the impedance response of the planar-electrode, electrolyte system. The model equations are converted from the time domain to the frequency domain using the technique employed by Doyle *et al.* (87). The technique requires the existence of a steady-state solution. Model equations are linearized around zero steady-state overpotential (open-circuit conditions) and expressed as a sum of steady-state and oscillating variable contributions. The steady-state variables can be cancelled, leaving a linear system of complex-valued equations.

The impedance response of a system is measured by perturbing the cell potential and measuring the current response. The cell potential and current density include a steady-state and oscillating contribution that depend on the angular frequency, ω, as

$$V = \overline{V} + \mathrm{Re}\left\{V \exp(j\omega t)\right\} \tag{3.11}$$

and

$$i = \bar{i} + \mathrm{Re}\left\{\tilde{i} \exp(j\omega t)\right\}. \tag{3.12}$$

Terms with overbars denote a steady-state component, and terms with tildes denote an oscillating component expressed as a complex phasor. The impedance response is given as the ratio of voltage to current phasors and is given as

$$Z(\omega) = Z_{re} + jZ_{im} = \frac{\tilde{V}}{\tilde{i}}. \tag{3.13}$$

At the electrode-SEI interface, the current contributions are given as

$$\tilde{i} = \tilde{i}_{far} + \tilde{i}_{dl} = \frac{\tilde{V}}{Z_{far}} + \frac{\tilde{V}}{Z_{dl}}. \tag{3.14}$$

where Z_{far} is the faradaic impedance, and Z_{dl} is the impedance due to double-layer charging. The impedance of the double-layer capacitor is defined as

$$Z_{dl} = \frac{1}{j\omega C_{dl}}, \tag{3.15}$$

where j is the imaginary unit and ω is the angular frequency with units of rad-s^{-1}. Equation (3.14) can be rewritten in terms of impedance as

$$Z(\omega) = \frac{\tilde{V}}{\tilde{i}} = \frac{Z_{far} Z_{dl}}{Z_{far} + Z_{dl}}. \tag{3.16}$$

Linearization of the Butler-Volmer kinetic expression around the open-circuit voltage, $\bar{V} = 0$, gives

$$\tilde{i}_{far} = i_0 \left(\frac{F\tilde{V}}{RT} - \frac{\tilde{c}_{o,p}(0)}{c_{o,b}} + \frac{\tilde{c}_{r,p}(0)}{c_{r,b}} \right). \tag{3.17}$$

We note that at zero steady-state surface overpotential $\bar{c}_o(0)/c_{o,b} = \bar{c}_r(0)/c_{r,b} = 1$. We define the following concentration impedances,

$$Z_{o,p} = \frac{\tilde{c}_{o,p}(0)}{\tilde{N}_{o,p}(0)} \; ; \; Z_{r,p} = -\frac{\tilde{c}_{r,p}(0)}{\tilde{N}_{r,p}(0)} . \tag{3.18}$$

Z_o and Z_r are caused by the diffusion of redox species through the porous SEI. These concentration impedances are analogous to finite Warburg diffusion elements. At the electrode, SEI interface, the fluxes of oxidized and reduced species are equal and opposite

$$\tilde{N}_{o,p}(0) = -\tilde{N}_{r,p}(0) . \tag{3.19}$$

The faradaic current is related to the flux of oxidized or reduced species at the electrode-SEI interface,

$$\tilde{i}_{far} = F\tilde{N}_{i,p}(0) . \tag{3.20}$$

Combining Equations (3.17), (3.18), and (3.20), the total faradaic impedance is given as

$$Z_{far} = \frac{RT}{Fi_o} + \frac{RT}{F^2}\left(\frac{Z_{o,p}}{c_{o,b}} + \frac{Z_{r,p}}{c_{r,b}}\right) . \tag{3.21}$$

The flux of oxidized or reduced species in the SEI is given as

$$\tilde{N}_{i,p} = -D_{i,eff}\frac{d\tilde{c}_{i,p}}{dx}, \tag{3.22}$$

where $D_{i,eff} = D_i \frac{\varepsilon_p}{\tau_p}$ is defined as the effective diffusivity of either redox couple species.

The associated material balance of redox species in the SEI is given as

$$\frac{\partial \varepsilon \tilde{c}_{i,p}}{\partial t} = D_{i,eff} \frac{\partial^2 \tilde{c}_{i,p}}{\partial x^2} . \quad (3.23)$$

At the SEI-diffusion layer interface, the superficial flux of charged species is continuous,

$$F\tilde{N}_{i,p}(L_p) = F\tilde{N}_{i,d}(L_p) . \quad (3.24)$$

Additionally, the in-pore concentration is continuous at the SEI-diffusion layer interface,

$$\tilde{c}_{i,p}(L_p) = \tilde{c}_{i,d}(L_p) . \quad (3.25)$$

Transport in the diffusion layer is treated with equations (3.22) and (3.23), with all *p* subscripts changing to *d*. Additionally, $\varepsilon_d = \tau_d = 1$.

The model was implemented in gPROMS v3.6 (Process Systems Enterprise Ltd.). Kinetic and transport parameters were visually fitted using both EIS and CV experimental data.

Experimental

Experiments were conducted in three-electrode cells made from Teflon, using an Autolab Metrohm Compact Potentiostat Model PGSTAT101. All electrochemical experiments were performed in an argon- glovebox at room temperature. Additionally, prior to any passivation or characterization experiments, all cells were placed on vibration-damping mats (McMaster-Carr) as a preventative measure to minimize convection.

A 1.3 mL Teflon cell was used for SEI formation experiments. A 3 mm diameter glassy-carbon electrode, shrouded in chlorotrifluoroethylene, was used as the working electrode (Basi, Inc.). Lithium foil was used as both counter and reference electrodes (Sigma Aldrich). In each SEI formation experiment, glassy-carbon was subjected to potentiostatic holds at 0.6 V *vs.* Li/Li^+ potentiostatically in approximately 1.3 mL of electrolyte for several hold times.

Three electrolyte solutions were used to form the SEI. Neat electrolyte, FEC-containing electrolyte, and VC-containing electrolyte were used to form the SEI. Neat electrolyte was 1:1 (by weight) ethylene carbonate: diethyl carbonate with 1 M $LiPF_6$ (BASF). FEC- and VC-containing electrolytes were prepared by adding 5 weight percent FEC (Sigma Aldrich) and 5 weight percent VC (Sigma Aldrich) to neat electrolyte, respectively.

A second, separate 1.3 mL Teflon cell was used for electrochemical characterization of the formed SEIs. The passivated glassy-carbon electrode was transferred to this cell. Lithium foil was used as a reference electrode. A pristine glassy-carbon counter electrode or platinum wire was used as the counter electrode. The counter electrode was changed from lithium to allow the reverse reaction to occur to keep the concentration of redox species constant.

A fourth separate electrolyte solution was used for electrochemical characterization of the formed SEIs. Approximately 1.4 ± 0.1 mmol of ferrocene (Fc) and 1.8 ± 0.1 mmol ferrocenium hexafluorophosphate (Fc^+), obtained from Sigma

Aldrich, was dissolved in neat electrolyte. Fc/Fc^+ was used as received. The open-circuit potential of this solution was measured as 3.24 V *vs.* Li/Li^+.

After the passivated glassy-carbon electrode reached the open circuit potential, EIS was performed from 100 kHz to 10 mHz with a 5 mV perturbation around the open-circuit potential. Then, CV scans were measured at scan rates ranging from 1 $mV\text{-}s^{-1}$ to 100 $mV\text{-}s^{-1}$. EIS and CVs were obtained following passivation for four potential hold times: 10, 30, 45, and 60 minutes. The holds were sequentially performed.

Fc/Fc^+ was found to be stable in the presence of lithium foil. That is, no evidence of redox couple plating onto the surface of the lithium foil reference electrode was found. Any imbalance in the concentration of redox couple species would have led to observable changes in the expected steady-state, open-circuit potential.

All glassy-carbon electrodes were polished with 0.05 μm alumina solution (Pine Instruments) before each sequence of passivation characterization cycles. Then, all cell components were rinsed with isopropanol and deionized (18 MOhm) water. The cell was then dried at room temperature and subsequently returned to the glovebox for further experimentation.

Experiments were performed to measure the thicknesses of SEIs in neat, FEC, and VC-containing electrolytes. Polypropylene cells, approximately 2.0 mL in volume, were fabricated to form SEIs on glassy-carbon disc electrodes (Ted Pella, Inc.), with electrode surface area limited by a Viton® Fluoroelastomer O-ring (McMaster-Carr). We note that Buna® rubber O-rings (McMaster-Carr) were incompatible with our system and found to

leach into the electrolyte. The glassy-carbon working electrode was then removed from the cell, separated from the O-ring, and gently rinsed with DMC to remove excess lithium salt. The electrode was dried in the antechamber of the glovebox and subsequently taken for analysis following the drying period. A focused ion beam/scanning electron microscope (FEI Nova Nanolab 200, gallium liquid metal ion source) was used to open a regular cross-sectional face by trench milling. The ion accelerating voltage was 30 kV and polishing cuts were made at 30 pA. Subsequently, SEM images were taken at 5 kV. During transfer from the glovebox to the scanning electron microscope, the electrode was briefly exposed to oxygen and moisture from the air.

IR spectra were measured for the passivated 3 mm diameter glassy-carbon electrode for neat, FEC-containing, and VC-containing electrolytes. IR spectra were obtained using a Nicolet IS50 with a Ge crystal. Spectra were recorded with a resolution of 4 cm^{-1}, and 64 interferogram scans were averaged, providing spectra from 400 to 4000 cm^{-1}. The sample measurements were conducted in ambient conditions outside of the glovebox.

Results and Discussion

Determining Extent of Surface Passivation

In Figure 3.2, CV scans are given for neat, FEC, and VC-containing electrolyte for a glassy-carbon electrode. The first two cycle scans are shown for each system. All electrolytes contained no redox couple; and therefore, the open-circuit potential was

defined by trace impurities on assembly. The open-circuit potential on assembly was approximately 3 V. The potential was swept between 3 V to 100 mV at ν = 10 mV-s^{-1}.

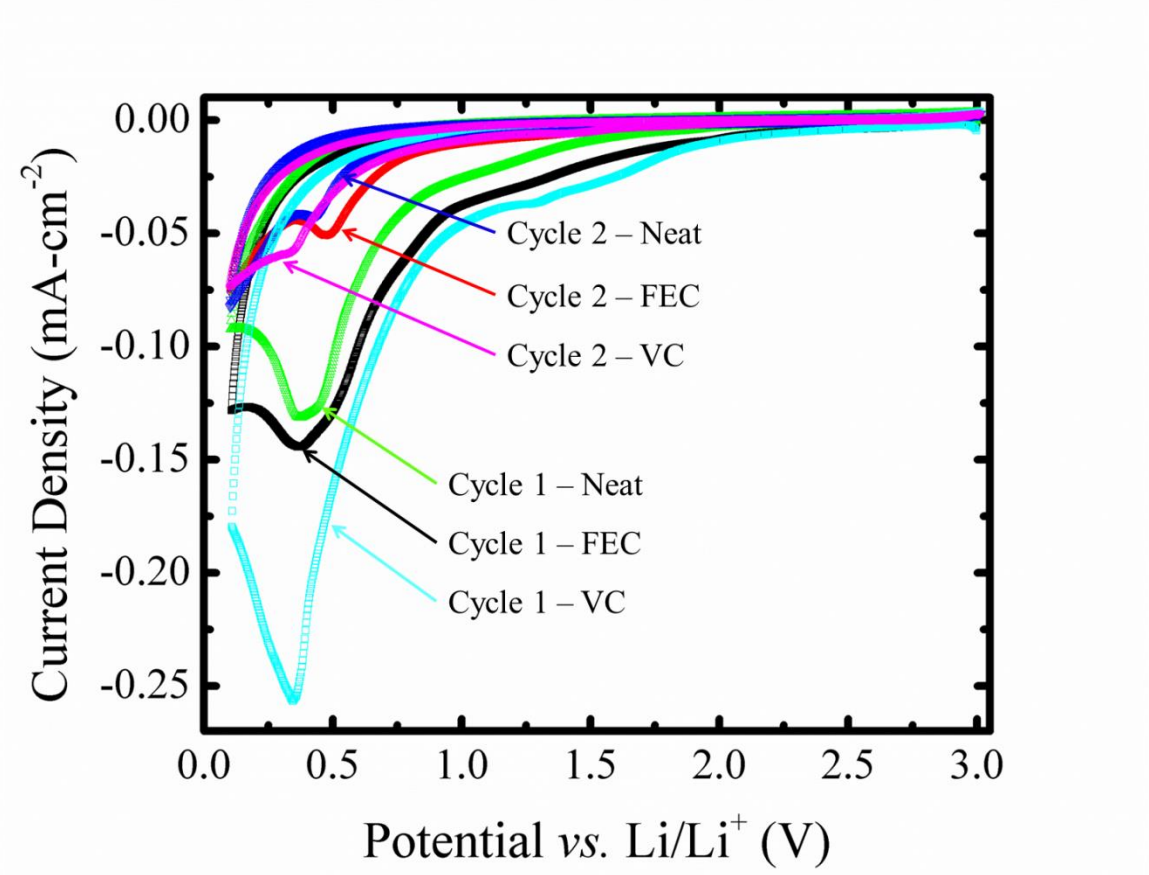

Figure 3.2. CV scans of glassy carbon in neat, FEC-containing, and VC-containing electrolytes. The first two cycles for each sample are given, with ν = 10 mV-s^{-1}. Data in blue and green correspond to neat electrolyte. Data in red and black correspond to FEC-containing electrolyte. Data in magenta and cyan correspond to VC-containing electrolyte. Reduction current densities are generally equivalent to or higher over a given cycle for electrolyte with FEC and VC than neat electrolyte. A large decay in the 1st cycle current is observed for all electrolytes. There is no evidence of intercalation into the electrode.

The addition of VC and FEC to the electrolyte causes an increase in the magnitude of the current response during both cycle one and two over the potential range. In general, the peak positions remain constant when comparing the three electrolytes, indicating that the reduction processes are attributable to the same phenomena. Following the first cycle cathodic and anodic sweeps, a large decay in the magnitude of current occurs in the second cycle over the same potential range. Shoulder peaks on the cathodic scan start at approximately 2 V for FEC- and VC-containing electrolytes and 1.5 V for neat electrolyte. Zhang *et al.* also observed relatively positive reduction potentials of organic electrolytes on glassy carbon (104). We speculate that the reduction potentials are more positive than expected because of the reduction kinetics on glassy carbon are likely different than graphite. Addtionally, trace water contamination is a possibility, and additives are introduced into the electrolyte, each with a characteristic reduction potential. There are no visible oxidation peaks on the anodic sweeps, confirming that the electrode is indeed inert over the potential range. This observation is in agreement with previous experimental work using glassy-carbon working electrodes (60, 104). From the data, it is inferred that the faradaic current that is passed results in the formation of reduction products on the electrode surface.

In Figure 3.3, sample curves are given showing SEI formation in neat electrolyte on a pristine glassy-carbon electrode under conditions of potentiostatic hold at 0.6 V *vs.* Li/Li^+. In Figure 3.3(a), the magnitude of the current density decays with increasing passivation time. The sharp decays indicates that initial passivation products slow the rate of reduction of the electrolyte on the electrode surface. The decay in the current density under potentiostatic hold is consistent with the first and second cycle current

density decay observed in the CVs given in Figure 3.2. In Figure 3.3(b), the formation charge, -q, is shown and obtained by integrating the current density from Figure 3.3(a).

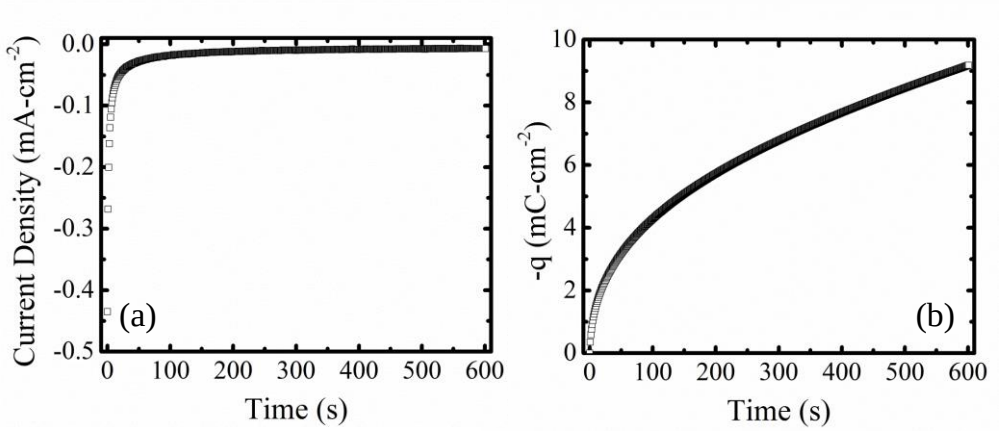

Figure 3.3. Sample SEI formation curves in neat electrolyte on a pristine glassy-carbon electrode under a potentiostatic hold at 0.6 V *vs.* Li/Li^+. (a) Current density and (b) total formation charge, *-q*, versus time of the potentiostatic hold.

In Figure 3.4, we show the total film-formation charge passed versus the square root of hold time for the glassy-carbon electrode. The total film-formation charge is the final point of the sample formation-charge curve in Figure 3.3(b). Therefore, in Figure 3.4 each data point represents a separate experiment with the final time dependent formation-charge value obtained given in Figure 3.4. The electrode was either continuously passivated for the entirety of the hold time or passivated and characterized, with the cumulative passivation time shown.

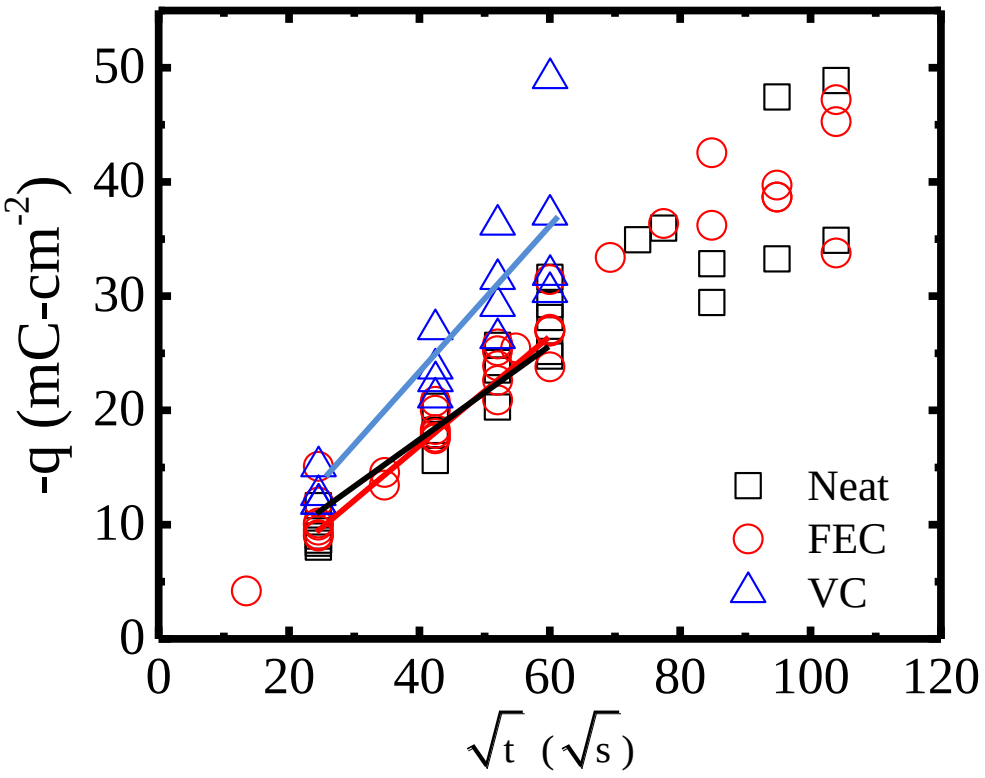

Figure 3.4. Film-formation charge versus the square root of the hold time for neat, FEC-containing, and VC-containing electrolyte passivated at 0.6 V *vs.* Li/Li^+. The total charge was obtained by integrating the current over the passivation time.

Best fit lines indicating the slopes of the passivation processes are overlaid on data from 10, 30, 45, and 60 minutes. The four passivation times are chosen because ferrocene characterization was also performed only at these times. The formation charge scales linearly with the square root of time for cells with neat, FEC-containing, and VC-containing electrolyte used for passivation. The slopes appear to be slightly different, indicating differences in the rates of passivation for each electrolyte. Surprisingly, VC is considerably more reactive than both FEC and neat electrolyte for the same amount of formation time. Scatter in the data is partially attributable to variations in concentrations

of surface oxide species after the cleaning procedure that are known to be present on glassy-carbon electrodes (105).

Ferrocene Reaction on Pristine Electrode

In this system, ferrocenium is reduced at the working electrode, and ferrocene is oxidized at the counter electrode

$$[Fe(C_5H_5)_2]^+PF_6^- + e^- \rightleftharpoons Fe(C_5H_5)_2 + PF_6^- . \quad (3.26)$$

The Nernst equation describes the concentration of reactants at the electrode surface under equilibrium conditions, where kinetics is reversible. Under Nernstian conditions, the concentrations are related to the cell potential by

$$E_{cell} = E^0 + \frac{RT}{nF}\ln\left(\frac{c_o(0)}{c_r(0)}\right), \quad (3.27)$$

where E_{cell} is the reversible cell potential and E^0 is the standard potential for the reaction. As previously shown, ferrocenium reduction has been measured as a one-electron transfer reaction, $n = 1$. For this one electron transfer reaction, the measured open-circuit potential is expected to be 3.24 V *vs.* Li/Li^+ (44, 106).

In Figure 3.5, CVs of cleaned glassy carbon are shown in neat electrolyte with and without Fc/Fc^+. The reversible condition, governed by the Nernst expression, is given as a comparison to the redox couple CV. The electrode scan rate is $\nu = 1\ mV\text{-}s^{-1}$, measured from 3 V to 3.5 V *vs.* Li/Li+. Redox-couple electrolyte contains approximately 1.8 and 1.4 mmol of Fc and Fc^+, respectively. The diffusivities of both redox species

were determined from fitting the Nernst equation to the experimental Fc/Fc^+ CV. Fc^+ diffusivity and Fc diffusivity are measured as $1.5 \pm 0.1 \times 10^{-9}$ m^2-s^{-1} and $2.5 \pm 0.1 \times 10^{-9}$ m^2-s^{-1}, respectively.

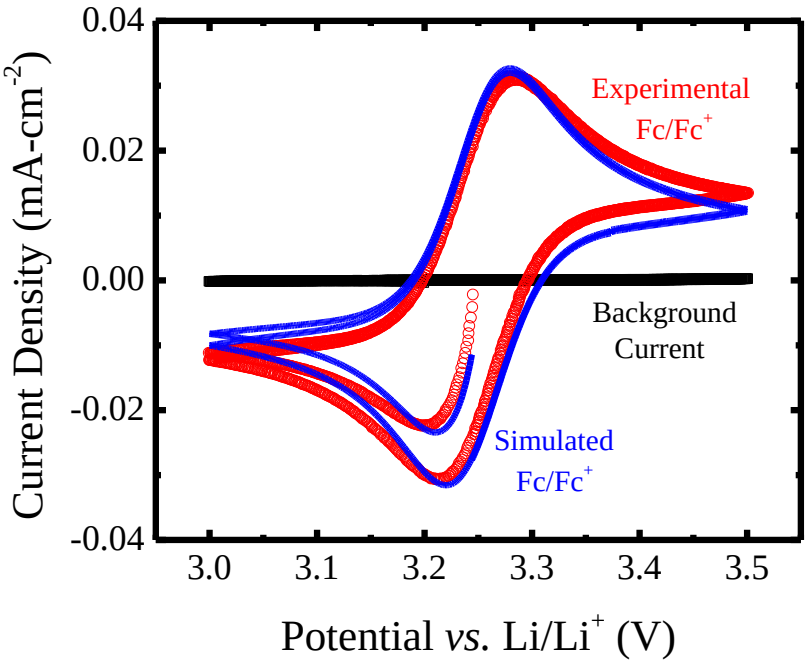

Figure 3.5. CVs of cleaned glassy carbon without (black) and with (red) the Fc/Fc^+. CVs were obtained at 1 mV-s^{-1}. Redox-couple electrolyte contains approximately 1.8 and 1.4 mmol of Fc and Fc^+, respectively. The reversible condition, governed by the Nernst expression, is shown as a comparison to the redox couple CV. The Nernst condition shows that the cleaning procedure is effective in removing films from the surface of the electrode.

In the absence of the Fc/Fc^+, the background current density is approximately zero over the potential range. After addition of the redox couple, a Fc oxidation peak appears around approximately 3.283 V. On the cathodic sweep, a ferrocenium reduction peak appears around approximately 3.213 V. The peak separation is approximately 70

mV. For true thermodynamic reversibility at 25 °C, the peak to peak voltage separation is approximately 59 mV. However, the peak voltage separation data is in agreement with previous work using Fc/Fc^+ (106).

The differences between the reversible Nernstian case and the experimental measurement are a combination of two phenomena. First, the cleaning procedure is imperfect. The alumina polish, although extremely effective in removing surface films, is only one approach to cleaning the electrode. A second approach is to electrochemically strip the film off the electrode by cycling the electrode at highly anodic potentials (44). This technique was attempted to refresh the electrode but was not effective in refreshing the electrode. Polishing the electrode with 50 nm alumina solution was found as most effective in enhancing reproducibility. Second, natural convection in the electrolyte during electrochemical cycling likely leads changes in the transport behavior of Fc/Fc^+. The boundary layer thickness is dynamic in such a scenario and subsequently causes variation in the amount of Fc/Fc^+ available at the electrode surface for reaction.

Of importance is that, because the electrode does not have capacity, any changes to the Fc/Fc^+ CV from Nernst conditions following passivation are a result of SEI formation reactions.

Characterization of Surface Passivation Using Ferrocene

Representative experimental impedance responses of glassy-carbon electrodes in Nyquist-plot format are given for samples passivated in neat electrolyte (Figure 3.6(a)

and Figure 3.6(d)), in FEC-containing electrolyte (Figure 3.6(b) and Figure 3.6(e)), and VC-containing electrolyte (Figure 3.6(c) and Figure 3.6(f)). In Figure 3.6(a), experimental impedance spectra are given for a fresh sample and samples passivated for times not exceeding 60 minutes. At first glance, there is one depressed arc over the high and mid-frequency ranges, with a low frequency tail-like process. Referring to Figure 3.6, the first arc in each of the spectra is assigned to an overlapping kinetic process at $x = 0$ and mass-transport processes of redox species through the SEI, from $x = 0$ to $x = L_p$. The width of the arc depends strongly on passivation time, with electrodes passivated for less than 30 minutes having widths less than 3 $k\Omega - cm^2$. At longer passivation times, the width of the arc increases due to passivation and becomes much more pronounced.

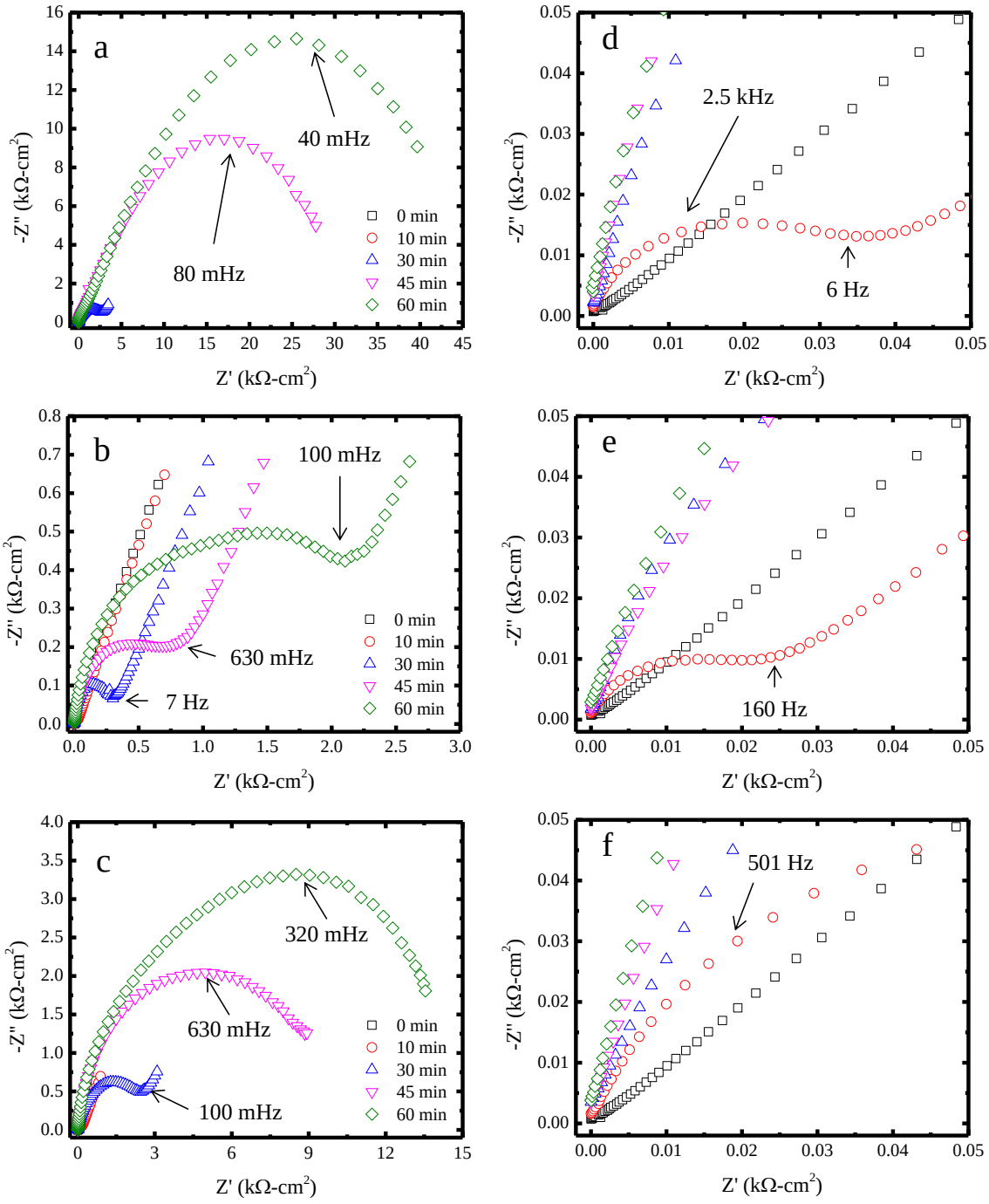

Figure 3.6. Nyquist plots of the impedance response of Fc/Fc^{+} before and after passivation. Responses to increasing passivation times are given. (a) Entire spectra given after passivation in neat electrolyte. (b) Entire spectra given for various hold times after passivation in FEC-containing electrolyte. (c) Entire spectra given for various hold times after passivation in VC-containing electrolyte. (d) The spectra in (a)

are stretched to show high-frequency behavior. (e) The spectra in (b) are stretched to show high-frequency behavior. (f) The spectra in (c) are stretched to show high-frequency behavior.

In Figure 3.6(b), impedance responses are given for the same hold times as in Figure 3.6(a) after the samples were passivated in FEC-containing electrolyte. The impedance responses show the same characteristic features as in Figure 3.6(a). However, the mid-frequency arcs are significantly narrower for samples passivated in electrolyte with FEC than neat electrolyte, when comparing spectra obtained after the same passivation hold times. The results indicate that passivation with FEC-containing electrolyte allows for increased redox shuttle kinetics and mass transport in the SEI than after passivation in neat electrolyte.

The low-frequency process, approximately a 45-degree sloping line, is caused by diffusion of redox species in the diffusion layer. This process is most clearly seen in Figure 3.6(b). The magnitude of imaginary impedance of this tail generally remains constant from 0 min to 60 min of hold time, indicating that this process is independent of surface passivation. Therefore, we conclude that this tail in the low frequency response is attributable to bulk diffusion of the redox species.

In Figure 3.6(c), the impedance response is given for Fc/Fc^+ in VC-passivated electrolyte. Similar to the findings with neat and FEC-containing electrolyte, two time constants appear in the data. These time constants can be shown to correspond with Fc/Fc^+ reduction kinetics and mass transport across the SEI. Additionally, the magnitude of the real component of the impedance increases with increasing passivation time. Noticeably, the magnitude of the impedance response is considerably less with

passivation with VC-containing electrolyte than with neat electrolyte, although greater than with FEC-containing electrolyte. The exception to this observation is given after a ten minute hold when comparing the representative spectra. A comparison of the impedance responses suggest that Fc/Fc^+ passivation behavior observed with VC-containing electrolyte is consistent with FEC-containing electrolyte.

In Figure 3.6(d), Figure 3.6(e), and Figure 3.6(f) both real and imaginary impedance axes have been expanded to show the high-frequency response of Figure 3.6(a), Figure 3.6(b), and Figure 3.6(c) respectively. The expanded axes show the same features of the full response, a depressed arc for the kinetic and mass-transport impedances and diffusion layer semi-infinite diffusion creating a Warburg element. Electrodes that were not passivated are also included in as a single spectrum. The response for the fresh samples show no arcs and only a Warburg element, indicating nearly reversible kinetics and no evidence of measureable surface passivation.

In Figure 3.7, CVs are given for both electrodes with and without passivating films. Following passivation, CVs were taken at scan rates of 10 mV s^{-1} around the open-circuit potential, approximately 3.24 V vs. Li/Li^+. The limits were chosen to allow enough of a potential range to observe redox-couple kinetic and mass-transport processes but also to limit further oxidation or reduction of the formed passivation layer. In Figure 3.7(a), 10, 30, 45, and 60 minute hold data is given for an electrode passivated in neat electrolyte. Additionally, a single reference voltammogram is given for a fresh electrode, labeled as 0 minutes. For the fresh electrode, the current response shows nearly reversible behavior, with a peak to peak voltage difference of approximately 70 mV. For

longer passivation times, peak heights decrease, and peak voltages drift away from reversible conditions. At 60 minutes, passivation leads to a significant reduction in peak currents and shifts in potentials, indicating a significant change in ferrocenium-reduction kinetics and mass transport.

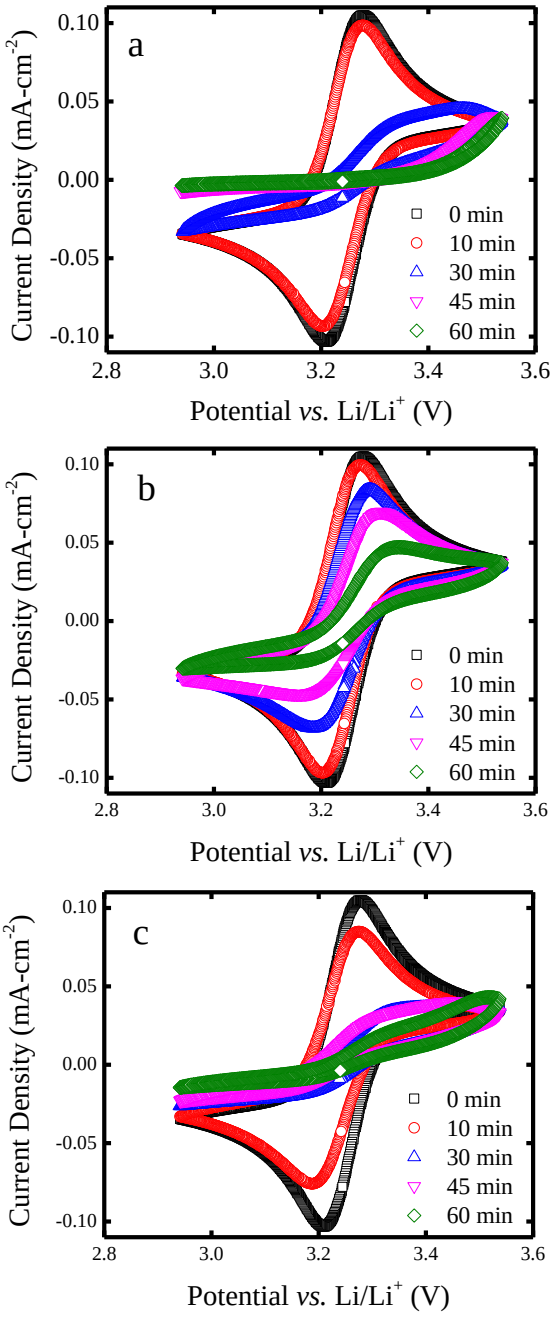

Figure 3.7. CVs of Fc/Fc^+ before and after passivation. Scan rates are 10 $mV\text{-}s^{-1}$. (a) 5th cycle CVs for an electrode passivated in neat electrolyte. (b) 5th cycle CVs for an electrode passivated in electrolyte containing FEC. (c) 5th cycle CVs for an electrode passivated in electrolyte containing VC.

In Figure 3.7(b), CVs are given for the same hold times as in Figure 3.7(a) after the samples were passivated in FEC-containing electrolyte. A comparison of passivation times between Figure 3.7(a) and Figure 3.7(b) reveals that, for all passivation time, the current is larger in magnitude after passivating with electrolytes containing FEC. At times longer than 30 minutes, the peak current positions shift for the Fc/Fc^+ scan after passivation in either electrolyte, indicating a significant increase in the overpotential necessary to drive the redox reaction. Additionally, the voltammograms flatten in shape further suggesting reduced ease of transport and less facile charge transfer due to increased levels of passivation. In Figure 3.7(c), CVs are given for the same hold times as in Figure 3.7(a) after the samples were passivated in VC-containing electrolyte. VC passivation provides the same time-dependent passivation behavior, with slight differences in the shapes of the scans. However, a comparison of passivation times amongst all three electrolytes indicates similar trends in Fc/Fc^+ scans. Additionally, the CVs qualitatively agree with the impedance responses measured in Figure 3.6 for each electrolyte.

We have assumed from the outset that the Fc/Fc^+ is analogous to solvent molecules in the SEI. Thus far, our results suggest that additives are less passivating to the Fc/Fc^+ than neat electrolyte, despite a formation charge that is greater than or equal to one another. The results are counterintuitive. The purpose of additives is to more effectively passivate the surface to prevent reduction of solvent. However, here we

observe that Fc/Fc^+ reduction kinetics and mass transport appear to be less suppressed when the electrode is passivated in additive-containing electrolyte. Next, we explore the potential causes of observed counterintuitive behavior.

Estimation of Kinetic and Transport Parameters

To gain mathematical insight into the counterintuitive behavior observed thus far, the model is used to fit the experimental impedance responses and CVs of FEC-containing, VC-containing, and neat electrolyte passivated samples to extract SEI physical properties. There are multiple approaches that can be used to fit the experimental impedance response and CV data obtained for the fresh and passivated electrode samples. In this work, we use both time constants and characteristic features of the impedance response to justify parameters fits. Sample experimental impedance response and CVs are provided in Figure 3.8. A total of 35 impedance spectra and CVs were acquired for neat, FEC-containing, and VC-containing electrolyte over the range of passivation times presented in Figure 3.4. The exchange-current density (i_0), SEI thickness (L_p), tortuosity (τ), and porosity (ε) parameters are presented as a function of passivation time in Figure 3.9. We note that the double-layer capacitance (C_{dl}) is also a fitted parameter, ranging from $15 \pm 10\ \mu F\text{-}cm^{-2}$. Additionally, the transfer coefficients are subjected to the constraint $\alpha_a + \alpha_c = 1$. The value of α_a ranged between 0.5 and 0.89 and was obtained from fitting the cathodic sweep of the CV. In many cases, the value of α_a was inconsequential to the fittings, as the effects of the L_p dominated the experimental data.

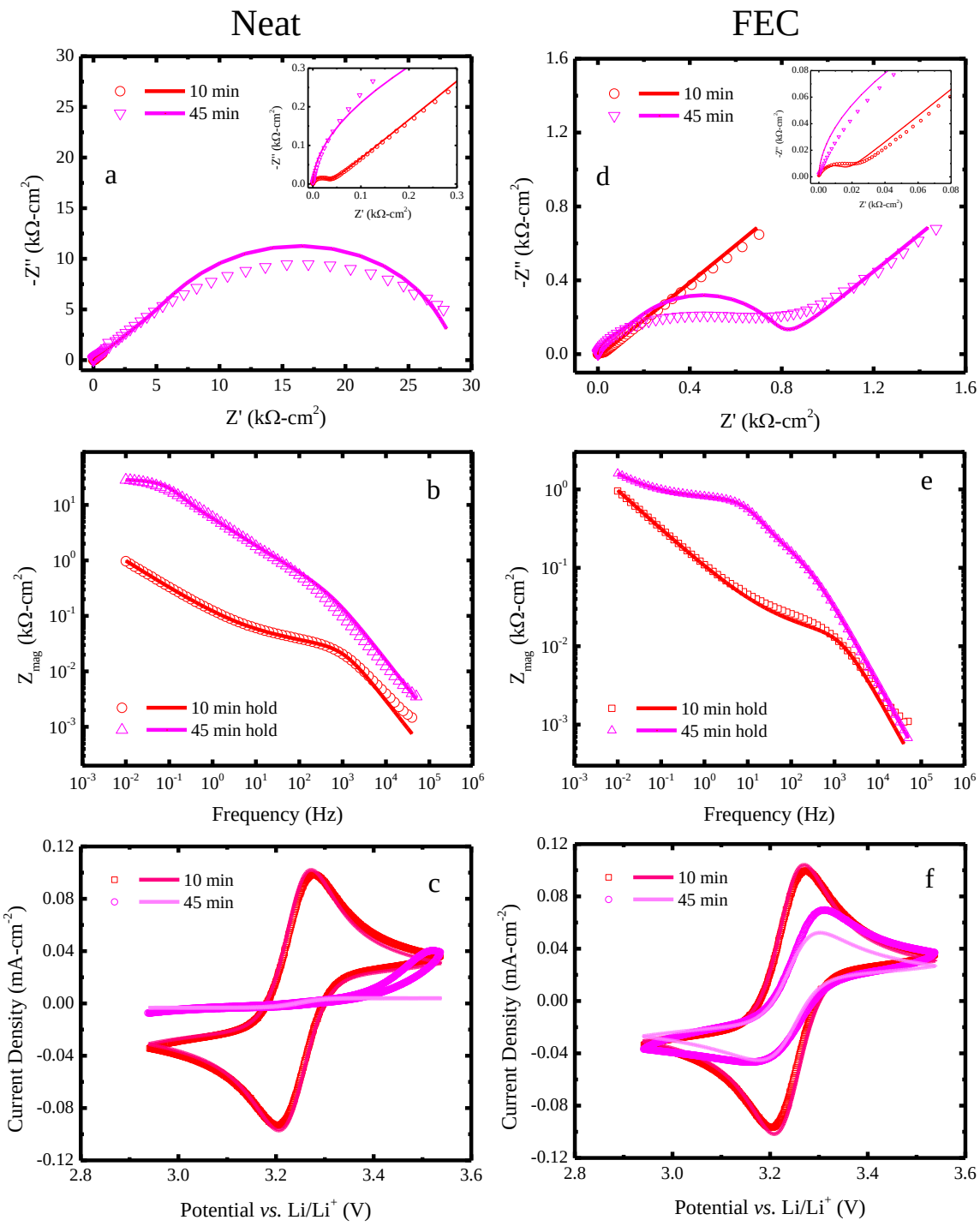

Figure 3.8. Sample Nyquist plots, Bode plots, and CVs of Fc/Fc^+ with simulation results overlaid. The (a), (b), and (c) correspond to neat electrolyte and (d), (e), and (f) to FEC-containing electrolyte. Response to ten minute and forty-five minute passivation times are shown and insets are provided for the high-

frequency portion of the impedance spectra. VC-containing electrolyte passivation (not shown) appears similar in fitting.

In Figure 3.8, we show Nyquist plots, Bode plots, and CVs of Fc/Fc^+ for samples passivated for ten and forty-five minutes in both electrolytes, with model fits overlaid. Figure 3.8(a), Figure 3.8(b), Figure 3.8(b) are measured after passivation in neat electrolyte. Figure 3.8(d), Figure 3.8(e), Figure 3.8(f) are measured after passivation in FEC-containing electrolyte. Insets are shown in Figure Figure 3.8(a) and Figure 3.8(d). For both Nyquist plots, the model captures the general shape of the response, a small arc at high-frequencies that is attributable to Fc/Fc^+ reduction kinetics at the electrode surface and a larger second arc that is a result of Fc/Fc^+ mass-transport across the SEI. The experimental data show a significant amount of time-constant dispersion, leading to a flattened rather than a true semicircular arc. Part of the time constant dispersion can be attributed to distributions in physical processes over a range of values that lead to multiple time constants for the governing processes. These time constants then overlap, creating a flattened or depressed semicircle in the spectra. The model captures some of this dispersion due to Fc/Fc^+ mass transport through the SEI. However, the model does not otherwise intentionally include distribution of physical processes. Unlike equivalent-circuit models, the model includes only physical processes and no artificial circuit elements that would capture arc depression. Therefore, this disagreement between experimental and simulated data is expected.

In Figure 3.8(b) and Figure 3.8(e), the Nyquist plots of Figure 3.8(a) and Figure 3.8(d) are recast as Bode plots. The magnitude of the impedance *vs.* frequency is shown for both neat and FEC-containing electrolyte with overlaid simulation results. The

overlaid simulation results show that, indeed, the model captures the general shape of the impedance response. The fittings show that, despite some of the difficulties encountered in fitting to the frequency due to semicircle depression in Nyquist plots, the fits agree with experimental data.

Figure 3.8(c) and Figure 3.8(f) show experimental CVs with simulation results overlaid, corresponding to the impedance spectra from Figure 3.8((a) and (c)) and Figure 3.8((b) and (d)), respectively. The parameters obtained from impedance spectra fittings were used to simulate the CVs. In both Figure 3.8(c) and Figure 3.8(d), the model and experimental voltammograms show good agreement for ten minutes of hold time. The model captures peak heights, peak positions, and general shape of the voltammograms. At potentials away from peak current density, a mass-transfer limiting current becomes evident, with current densities limited by transport of redox species to the reaction interface. Simulations for forty-five minute hold times show less agreement with experimental measurements. Near the open-circuit potential (approximately 3.24 V), the simulated CVs capture the general shape and current densities experimentally measured. However, at potentials further from open circuit, the simulated current densities tend to be much smaller than those measured experimentally. We suspect that there are two causes for the deviation. First, part of the additional current at highly anodic overpotentials leads to SEI oxidation reactions. We speculate that a host of reversible and irreversible SEI components are formed during passivation. A fraction of these reversible components undergoes oxidation. Additionally, despite the precautions that are taken in the experimental setup, natural convection can occur in the electrolyte. The same convective effect is outlined in Figure 3.5.

In Figure 3.9, SEI physical parameters are provided as a function of passivation time. From the outset, we should note there are limitations in obtaining unique parameters using a stationary electrode with EIS and CV. Parameter fitting at low passivation times proved to be difficult, primarily because of a lack of sufficient time constant separation between kinetic and transport processes. In these cases, the parameters are averages of several possible fits of the data. Therefore, at shorter passivation times, there is significantly more error in the data fits than at longer passivation times.

The data generally show that electrodes passivated in FEC and VC form a thinner SEI, with less transport resistance for the redox couple than neat electrolyte passivation. In Figure 3.9(a), the exchange-current density appears to scale logarithmically with the total formation charge. The result is in contradiction to the linear relationship between formation charge and the square root of time, shown in Figure 3.4. This observation indicates that Fc/Fc^+ and solvent undergo unique reduction mechanisms. Therefore, Fc/Fc^+ is not exactly analogous to solvent molecules.

Figure 3.9(b) indicates that SEI thicknesses formed with additives tend to be less than those formed in neat electrolyte. In Figure 3.9(c), the porosity to tortuosity ratio is provided as a lumped parameter. The ratio of porosity to tortuosity decreases monotonically in the case of each electrolyte. The values of this ratio are surprisingly small, and as with thicknesses fittings, there is an obvious difference between neat and additive-containing electrolytes.

Surprisingly, the model predicts larger SEI layers compared to those observed in other electrode-electrolyte systems. In porous electrodes, graphite is the primary SEI-forming electrode material, with carbon additive included into the matrix to increase electronic conductivity. The SEIs formed in those systems tend to be on the order of 10 nm (30). There are two potential causes of the excessively large thicknesses obtained by simulation. First, a partial explanation of this difference is due to the electrode material, glassy carbon, used in this study. The kinetics of electrolyte reduction on glassy-carbon, as well as the planar geometry of the electrode may alter the properties of the SEI. These kinetics are likely unique to the chemistry of the glassy-carbon sample. This means that different glassy-carbon electrode samples are likely to form compositionally and structurally unique SEIs. Second, the Bruggeman relation is used to link porosity and tortuosity. The relationship is assumed to hold true for transport where pathways are obstructed by spherical and cylindrical particles (107). This assumed relationship is used in porous electrodes but is invalid here. We explore this relationship more in Chapter 4.

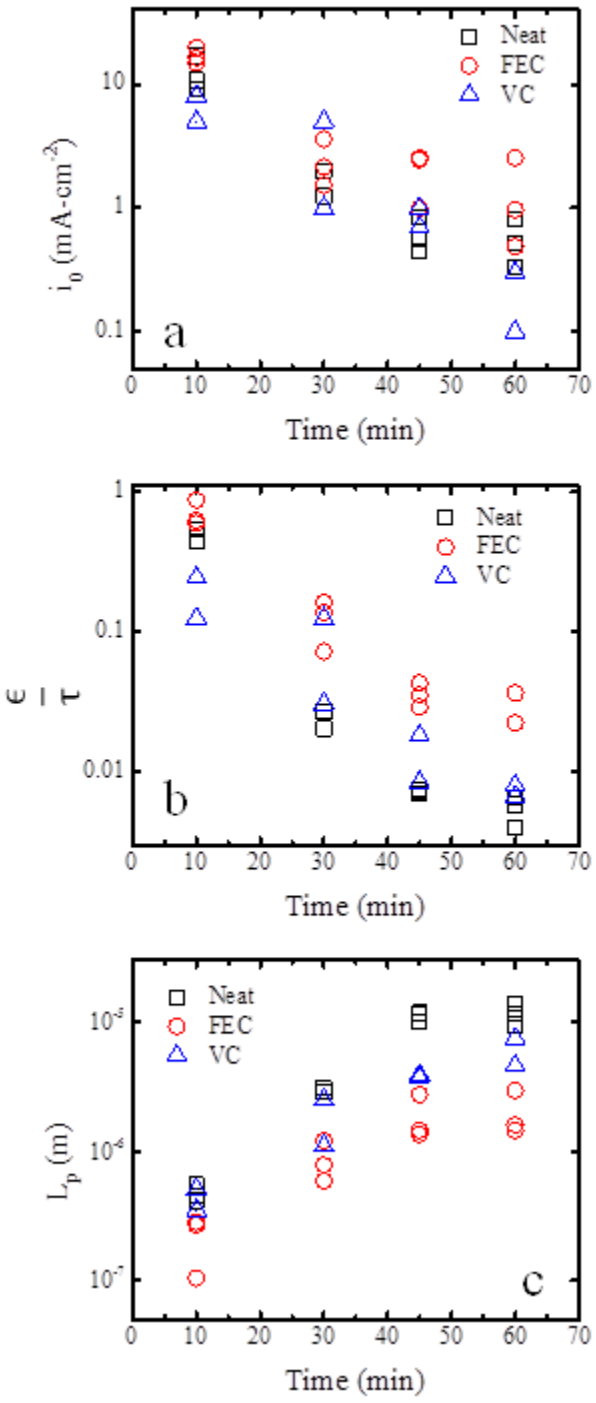

Figure 3.9. SEI physical parameters obtained from impedance and CV experimental data fittings of Fc/Fc^+. Parameters are fitted for SEIs formed from electrolytes in neat, FEC-, and VC-containing electrolyte. (a)

exchange-current densities, (b) SEI thickness, and (c) porosity to tortuosity ratios are provided from the fittings as a function of passivation time.

Model Fitting Uniqueness Explored

Figure 3.9(b) fittings suggest extremely large SEI thicknesses. To confirm if the simulated thickness is appropriate, in Figure 3.10, the uniqueness of the model fittings is explored. From the outset, we note that the Bruggeman relationship is used to define porosity and tortuosity in this system. Experimental data for 45 minutes of passivation in neat electrolyte, taken from Figure 3.8, is given with two simulation results overlaid. The arc width and time constant for diffusion are two scaled parameters that influence the shape of the impedance spectra. In the simulations, a frequency of 80 mHz is labeled for each spectrum. Based on our previous analysis in Figure 3.8, the arc shown corresponds to transport of the ferrocene redox couple in the SEI. The appearance of this arc in the impedance spectrum is governed by the thickness of the SEI, porosity of the SEI, and tortuosity of the SEI. Therefore, these three parameters are the parameters that must be unique. Additionally, between simulations one and two, ferrocene kinetics remain constant.

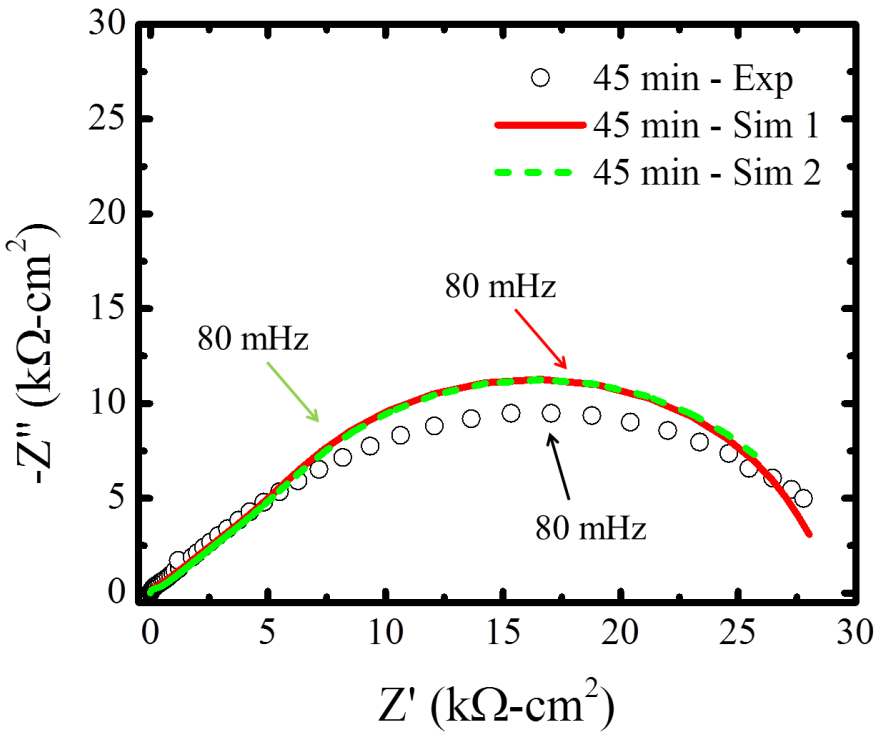

Figure 3.10. Model fitting uniqueness is explored. Two simulation results with different SEI thickness and tortuosity parameters are overlaid on experimental data for 45 minutes of passivation in neat electrolyte. In simulation one, the overlaid model spectrum captures the shape of the impedance spectra for a given thickness and tortuosity, with respect to the characteristic frequency. In simulation two, the thickness is doubled and porosity to tortuosity is halved from simulation one. The resulting simulation worsens as a result of the parameter change.

In simulation two, the SEI thickness is doubled and porosity to tortuosity ratio is halved from simulation one. The resulting simulation provides a worsened fit, despite the parameters intuitively having similar effects on ferrocene redox couple transport through the SEI. The uniqueness in fitting the ferrocene transport arc arises because of the assumption of the Bruggeman relation. In the experimental data, there are only two experimental constraints. The first constraint is the arc width. The second constraint is

the characteristic frequency. By assuming the Bruggeman relation, the three parameters are reduced to two parameters. Coupled with the two constraints set by the experimental data, we can uniquely identify two of the three parameters.

FIB+SEM Imaging of the Thickness of the SEI

As previously noted, the model fitting indicates that the SEIs formed in this electrode-electrolyte system are of much greater thicknesses than those thicknesses found in graphite-electrode based systems. To investigate the plausibility of the thickness fittings, FIB+SEM was used to obtain cross-sectional images of the SEIs in neat, FEC-containing, and VC-containing electrolyte in Figure 3.11. The electrodes were imaged after 10 minute passivation holds at 0.6 V vs. Li/Li^+. Cross-sectional images (x-z plane, where *z* is the through-plane direction) exposed by the FIB are shown. Multiple areas were imaged on the surface, with representative images provided. Thicknesses are labeled in each image, with scale bars shown in the bottom corner.

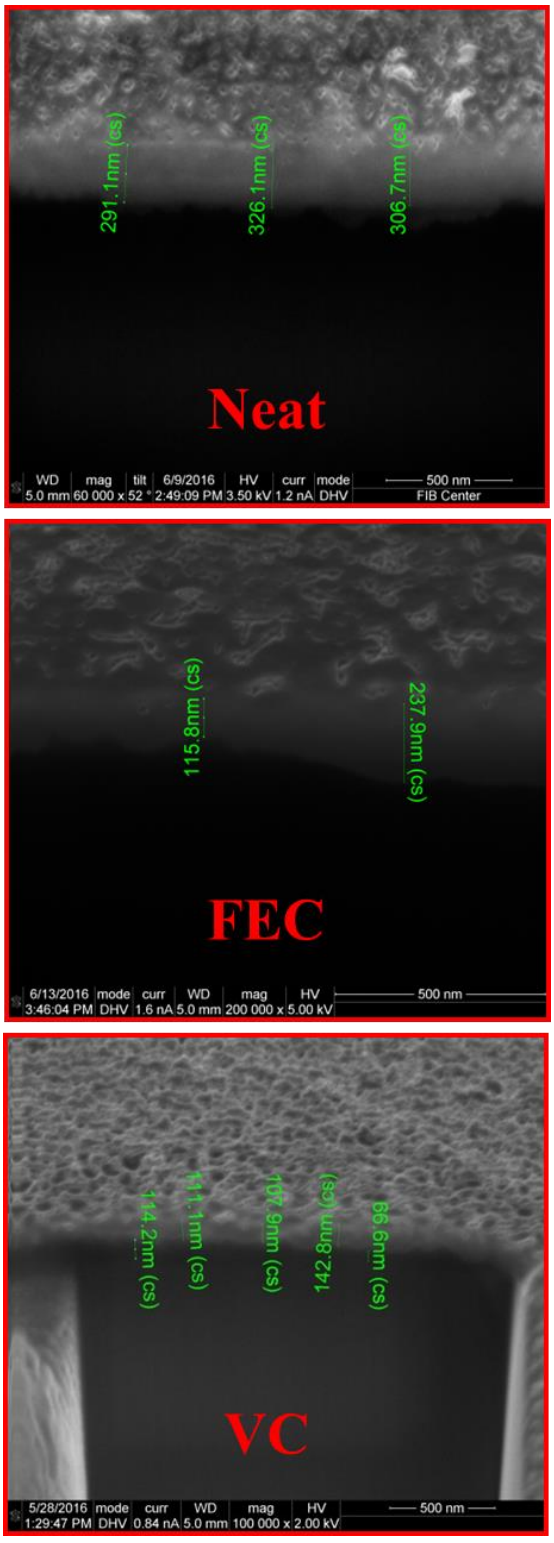

Figure 3.11. HR-SEM images for electrodes passivated in neat, FEC-, and VC-containing electrolytes. The thicknesses observed by microscopy are on the same order of magnitude as predicted by the model.

The electrodes appear passivated with a distinct difference noticeable between sample and SEI. The thicknesses, as indicated by the parameter fittings of Figure 3.9(b), are much larger than were expected based on SEI literature. Additionally, both FEC and VC-containing electrolytes appear to form thinner SEIs than neat electrolyte. The findings support the trends observed in literature, when comparing neat and additive-containing electrolytes. Additionally, the formed SEIs appear uniform in structure with pores or salt crystals still present on the surface.

Although the passivated sample is glassy carbon, the sample is different from the electrode used in Figure 3.4. Differences in the kinetic activity are likely to create SEIs with slightly different thicknesses and compositions. Further, the electrode is briefly exposed to air during transfer from the inert glovebox atmosphere to the SEM. The effects of oxidation of the exposed sample during transfer likely influence the physical structure of the observed SEI. Despite these factors, the SEM images still quantitatively support the large SEI thickness measurements obtained by fitting experimental ferrocene impedance responses and CVs for neat, FEC-containing, and VC-containing electrolyte.

Polymerization Reactions Driving the Formation of Large SEI Thicknesses

To further explore the cause of the larger-than-expected SEI thicknesses, we combine model results with experimental formation data. In Figure 3.12, the total formation charges for neat and FEC-containing electrolyte are given per unit volume of SEI. The total formation charge per unit volume of SEI has been obtained by normalizing the formation charges experimentally measured in Figure 3.4 by the SEI thicknesses obtained from simulation, given in Figure 3.9. As a reference compound for a graphite anode SEI, the total charge required to form lithium

carbonate, Li_2CO_3, is shown in the figure. Assuming a uniform SEI with Li_2CO_3 as the only formation product, the total formation charge per unit volume, Q_v, is calculated as

$$Q_{v,Li_2CO_3} = \frac{\rho_{Li_2CO_3} n_{Li} F}{M W_{Li_2CO_3}}, \tag{3.28}$$

where $\rho_{Li_2CO_3}$ is the density of Li_2CO_3, n_{Li} is the mole fraction of lithium in Li_2CO_3, F is Faraday's constant, and $M W_{Li_2CO_3}$ is the molecular weight of Li_2CO_3. The total formation charge values shown in Figure 3.12 are calculated assuming a completely filled SEI (void fraction = 0).

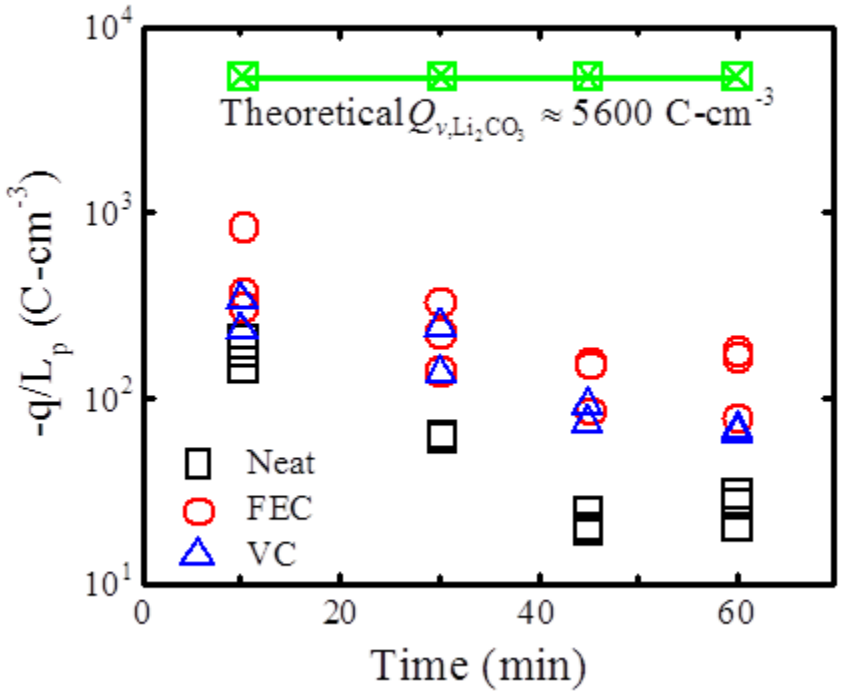

Figure 3.12. The experimental formation charge per unit volume of SEI formed. The total formation charge per unit volume of SEI has been obtained by normalizing the formation charges experimentally measured in Figure 3.4 by the SEI thicknesses obtained from simulation, shown in Figure 3.9. The

normalized formation charge values are provided for neat, FEC-, and VC-containing electrolyte. An additional compound is shown in the figure, Li_2CO_3, which is known to be a standard organic SEI formation product for neat electrolyte.

A stark difference is observed between the amount of charge taken to form the SEIs in this system and that taken to form a standard SEI product like Li_2CO_3 on a porous graphite electrode. We hypothesize that the counterintuitive relationship between formation charge and kinetic and transport resistance, as well as the large SEIs, are the result of polymerization reactions occurring during formation. A noticeable difference is evident in the normalized formation charge amongst neat, FEC- and VC-passivated samples. The difference suggests that the product distribution from additive reduction is closer to a porous graphitic SEI than a neat-electrolyte passivated sample. A number of studies in the literature have shown that organic electrolytes tend to polymerize during the formation process (98-100).

IR Spectroscopy to Determine Polymerization Effect

Following SEM imaging, the passivated electrodes were taken for IR spectroscopy to determine if polymerized compounds were detectable in the SEI. Polymerization reactions would drive unexpected growth of the SEI. In Figure 3.13, IR spectra are given for neat, FEC, and VC-passivated samples. A baseline spectrum is given for a fresh electrode. The IR-spectra peaks were referenced to several investigations of the composition of passivation products on anode surfaces in organic electrolytes (32, 36, 50, 97, 108-110).

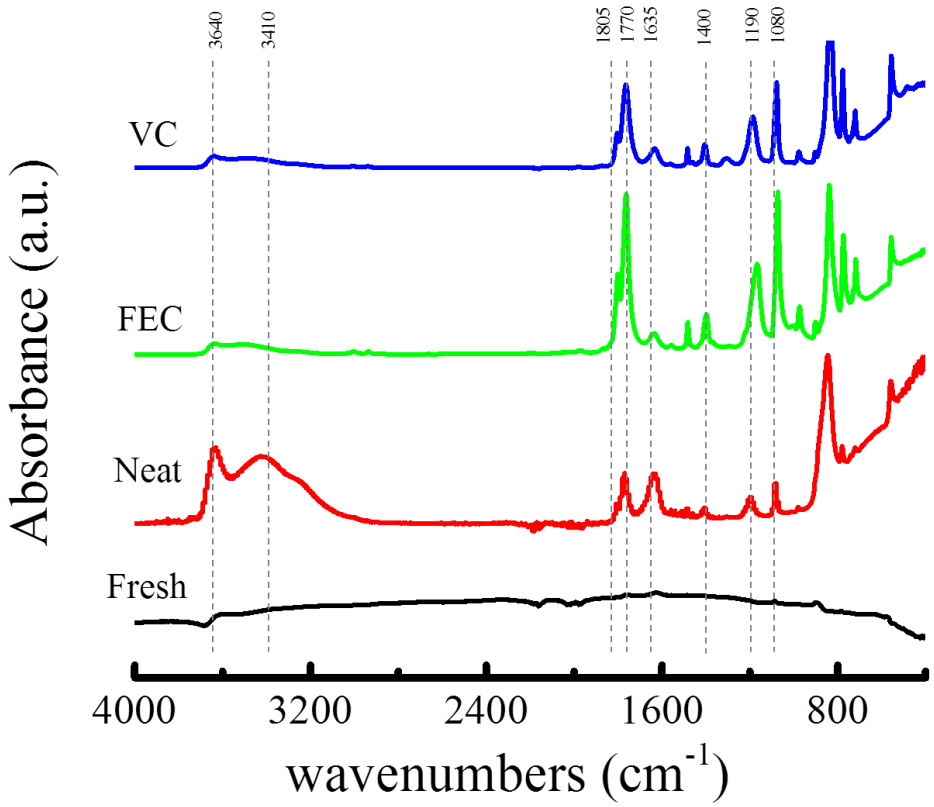

Figure 3.13. FTIR spectra for neat, FEC-, and VC-passivated electrodes. A fresh electrode spectrum is provided, as a baseline. The FTIR spectra comparison indicates the presence of polymerized compounds post passivation.

Several peaks are observed in each spectrum that indicates the presence of polymerized compounds on the electrode surface. For FEC- and VC-containing electrolyte samples, strong peaks are located at around 1770 cm^{-1}, corresponding to poly(FEC) and/or poly(VC) (32). A strong peak is observed for the FEC-passivated sample around 1805 cm^{-1}, corresponding to poly(FEC) (97). For all three passivated samples, peaks exist at around 1635 cm^{-1}, 1400 cm^{-1}, and 1080 cm^{-1} (32). These peaks roughly correspond to compounds characteristic of lithium alkyl carbonates, ROCOOLi.

Additionally, all three passivated samples contain peaks at around 1190 cm^{-1}, corresponding to residual ethylene carbonate in the SEI (110).

The results, however, are only reconcilable if it is assumed that the polymerization reactions in neat electrolyte are more extensive than additive-containing electrolyte. We can only speculate that this is the case, as all electrolytes appear to have polymerized compounds on the surface of their SEIs.

Coupled with the ferrocene impedance and CV measurements, the results thus far are consistent but still counterintuitive. Neat electrolyte passivates the surface of the electrode more effectively than additive-containing electrolyte. Both experimentally obtained and simulated thickness measurements qualitatively and quantitatively support the observation that neat electrolyte reduction provides more surface passivation.

The result is counterintuitive when thought of in terms of capacity fade. The thickness measurements would support the notion of less capacity fade with additive-containing electrolyte. Intuitively, thinner SEIs consume less lithium and solvent, thereby, helping retain capacity. However, for additives to be useful, they must also provide more surface passivation than neat electrolyte would provide. That is, the thinner must also be more passivating and not only thinner. In this work, we have observed the opposite result. The thinner SEIs appear less effective in passivating the surface.

An additional possibility that explains the observed relationship between passivation and SEI thickness between neat and additive-containing electrolyte is from our initial assumption that ferrocene is analogous to a solvent molecule. If ferrocene

kinetics and transport are more similar to lithium transport in the SEI, then the results are consistent with literature observations. In Chapter 4, we continue our study of the ferrocene redox couple to determine if the assumption is valid and what role passivation potential affects the utility of additive-containing electrolytes.

Conclusion

Glassy-carbon electrodes passivated in electrolyte with and without co-solvent additives are compared by investigating the interfacial kinetics and mass transport of the ferrocene redox species. From the outset, the redox species is assumed analogous in kinetics and mass transport to a solvent molecule.

During passivation, film formation charges are generally equivalent to or higher in additive-containing electrolyte in comparison to neat electrolyte. Film formation charge increases with the square root of time for all electrolytes investigated.

Experimental impedance responses and CVs of the ferrocene redox couple are measured after passivation for all electrolytes investigated, providing consistent results. Rates of ferrocene kinetics and mass-transport are shown to decrease with increasing passivation time for all electrolytes. Both FEC- and VC-containing electrolytes pass at least the same amount of formation charge during passivation but passivate the surface much less effectively than neat electrolyte. The result is counterintuitive.

Simulations are used to qualitatively assess the physical characteristics of the SEI formed and provide unique fitting parameters. Parameter estimations of the SEI thickness are on the order of hundreds of nanometers to microns in thickness, much

larger than expected. FIB+SEM cross sectional images of formed SEIs indeed show that the thickness measurements are on the order of hundreds of nanometers after ten minutes of potentiostatic hold, quantitatively supporting model thickness estimates.

The normalization of experimental formation charge with fitted SEI thicknesses indicates that polymerization reactions are influencing SEI structure. Further, FTIR analysis confirms the presence of polymerized SEI products for all three electrolytes. However, the possibility of polymerization reactions only partially reconciles the differences in SEI thickness between neat and additive-containing electrolytes that are observed.

Finally, the counterintuitive behavior between impedance and SEI thickness remains unresolved with the available data. We do note that the results from this investigation are not directly translatable to a porous graphite electrode but do offer insight into SEI formation and growth for various electrolytes on a model surface.

Acknowledgments

We would like to thank Graham Wentz for assisting in FTIR measurements.

References

1. M. Winter, The Solid Electrolyte Interphase – The Most Important and the Least Understood Solid Electrolyte in Rechargeable Li Batteries, in *Zeitschrift für Physikalische Chemie International journal of research in physical chemistry and chemical physics*, p. 1395 (2009).

2. E. Peled, *Journal of the Electrochemical Society*, **126**, 2047 (1979).

3. T. Joshi, K. Eom, G. Yushin and T. F. Fuller, *Journal of the Electrochemical Society*, **161**, A1915 (2014).

4. M. Nie, J. Demeaux, B. T. Young, D. R. Heskett, Y. Chen, A. Bose, J. C. Woicik and B. L. Lucht, *Journal of the Electrochemical Society*, **162**, A7008 (2015).

5. E. Markevich, G. Salitra, K. Fridman, R. Sharabi, G. Gershinsky, A. Garsuch, G. Semrau, M. A. Schmidt and D. Aurbach, *Langmuir* (2014).

6. D. Aurbach, K. Gamolsky, B. Markovsky, Y. Gofer, M. Schmidt and U. Heider, *Electrochimica Acta*, **47**, 1423 (2002).

7. M.-H. Ryou, G.-B. Han, Y. M. Lee, J.-N. Lee, D. J. Lee, Y. O. Yoon and J.-K. Park, *Electrochimica Acta*, **55**, 2073 (2010).

8. C. C. Nguyen and B. L. Lucht, *Journal of the Electrochemical Society*, **161**, A1933 (2014).

9. A. Bordes, K. Eom and T. F. Fuller, *Journal of Power Sources*, **257**, 163 (2014).

10. I. A. Shkrob, Y. Zhu, T. W. Marin and D. Abraham, *The Journal of Physical Chemistry C*, **117**, 19255 (2013).

11. S. E. Sloop, J. K. Pugh, S. Wang, J. B. Kerr and K. Kinoshita, *Electrochemical and Solid-State Letters*, **4**, A42 (2001).

12. H. Tavassol, J. W. Buthker, G. A. Ferguson, L. A. Curtiss and A. A. Gewirth, *Journal of the Electrochemical Society*, **159**, A730 (2012).

13. I. A. Shkrob, Y. Zhu, T. W. Marin and D. Abraham, *J. Phys. Chem. C*, **117**, 19270 (2013).

14. P. Arora, R. E. White and M. Doyle, *Journal of the Electrochemical Society*, **145**, 3647 (1998).

15. J. Vetter, P. Novák, M. R. Wagner, C. Veit, K. C. Möller, J. O. Besenhard, M. Winter, M. Wohlfahrt-Mehrens, C. Vogler and A. Hammouche, *Journal of Power Sources*, **147**, 269 (2005).

16. H. Shin, J. Park, A. M. Sastry and W. Lu, *Journal of the Electrochemical Society*, **162**, A1683 (2015).

17. C. Delacourt, *Journal of the Electrochemical Society*, **160**, A1997 (2013).

18. M. Tang, K. Miyazaki, T. Abe and J. Newman, *Journal of the Electrochemical Society*, **159**, A634 (2012).

19. M. Tang and J. Newman, *Journal of the Electrochemical Society*, **158**, A530 (2011).

20. M. Tang and J. Newman, *Journal of the Electrochemical Society*, **159**, A281 (2012).

21. M. Doyle, J. P. Meyers and J. Newman, *Journal of the Electrochemical Society*, **147**, 99 (2000).

22. M. Tang, S. Lu and J. Newman, *Journal of the Electrochemical Society*, **159**, A1775 (2012).

23. P. A. Staley, C. M. Newell, D. P. Pullman and D. K. Smith, *Analytical Chemistry*, **86**, 10917 (2014).

24. C. O. Laoire, E. Plichta, M. Hendrickson, S. Mukerjee and K. M. Abraham, *Electrochimica Acta*, **54**, 6560 (2009).

25. B. Tjaden, S. J. Cooper, D. J. L. Brett, D. Kramer and P. R. Shearing, *Current Opinion in Chemical Engineering*, **12**, 44 (2016).

26. H. Ota, Y. Sakata, A. Inoue and S. Yamaguchi, *Journal of the Electrochemical Society*, **151**, A1659 (2004).

27. M. Nie, D. Chalasani, D. P. Abraham, Y. Chen, A. Bose and B. L. Lucht, *The Journal of Physical Chemistry C*, **117**, 1257 (2013).

28. C. R. Yang, Y. Y. Wang and C. C. Wan, *Journal of Power Sources*, **72**, 66 (1998).

29. D. Aurbach, B. Markovsky, A. Shechter, Y. Ein-Eli and H. Cohen, *Journal of the Electrochemical Society*, **143**, 3809 (1996).

30. G. V. Zhuang, H. Yang, B. Blizanac and P. N. Ross, *Electrochemical and Solid-State Letters*, **8**, A441 (2005).

CHAPTER 4

INVESTIGATION OF THE DIFFERENCES IN PASSIVATION MECHANISMS OF NEAT AND ADDITIVE-CONTAINING ELECTROLYTES

Introduction

The solid electrolyte interphase (SEI) is a critical component to the commercial success of lithium-ion batteries (LiBs). The SEI forms as a result of electrolyte reduction reactions at the electrode-electrolyte interface. The reactions occur because LiBs typically operate outside of the electrochemical stability window of these organic electrolytes. The reduction reactions result in a significant decrease in LiB charge capacity. However, following the initial formation of the SEI and subsequent loss in capacity, the SEI as acts as a protective barrier between the electrode and electrolyte. That is, the SEI effectively blocks the uncontrolled reduction of electrolyte at the electrode surface, slowing the rate of capacity fade. Because of its unique ability to both consume capacity but also allow LiBs to successfully operate, identifying the characteristics of a stable SEI and the limiting growth mechanisms of the SEI are important to future battery development. The functionality of a stable SEI that allows for long-term battery operation has been identified.

A stable SEI meets two necessary requirements. First, the SEI should prevent the co-intercalation of solvent molecules into the negative electrode material. An example of a negative electrode material is graphite. It is composed of planes of graphene-like layers

that are held together by relatively weak forces (32). Ideally, only lithium ions intercalate into graphite during cell charging. However, some solvent molecules have been shown to co-intercalate in between the graphene planes. Intercalation of solvent molecules causes separation of the graphene planes, leading to the surface exfoliation (111). Prevention of exfoliation requires that the SEI limit solvent transport to the electrode surface where solvent co-intercalation could occur. Second, the SEI should minimize the amount of cycleable lithium consumed in the formation process. On cell assembly, the positive electrode is the source of all of the lithium that shuttles between the electrodes during charge and discharge. This lithium is intended to intercalate and deintercalate on charge and discharge from the positive and negative electrodes. During cycling, the lithium does cycle between the two electrodes. However, a fraction of the lithium is also consumed in the SEI formation process. Because the magnitude of cycleable lithium determines the energy density of the cell, limiting consumption during formation is critical to battery performance.

Chemical additives are frequently added as co-solvents to the primary electrolyte at low concentrations (*ca.*< 5 %) to form the SEI. SEIs formed by additive reduction have been shown to improve capacity retention rates, when compared to neat electrolyte (63, 64, 97). Two additives frequently used in LiBs to form the SEI are fluoroethylene carbonate (FEC) and vinylene carbonate (VC) (30, 97, 102, 112). The effectiveness of the chemical additives in passivating the surface depends on the particular electrode and electrolyte properties. Additionally, the rate of passivation and electrode potential are known to influence the effectiveness of the passivating layer.

Many groups have observed that additive-formed SEIs are more compact in thickness, yet exhibit less capacity fade (30, 64, 112). The observations associated with thickness are intuitive. A less thick SEI has likely consumed less cyceable lithium during formation. However, combined with the assessment of capacity fade, these observations alone are counterintuitive. The thinner SEI should compensate with more kinetic or mass-transport resistance to further electrolyte reduction. Without such compensation, SEIs formed by additive reduction would only increase electrolyte reduction rates. Ultimately, determining the kinetic and mass-transport differences in SEIs formed with neat and additive-containing electrolytes could provide insight into the limiting mechanism of growth of the SEI.

To investigate the how differences in growth mechanisms could affect the kinetic and transport resistances of the SEI, we extend the ferrocene characterization method to analyze the passivating nature of SEIs formed on planar electrodes (37, 44, 58, 60). In the technique, the ferrocene redox shuttle is used to probe the passivating characteristics of the SEI following formation. The ferrocene shuttle is assumed analogous to a solvent molecule. The technique is particularly useful in investigating SEI growth mechanisms, particularly because the equilibrium potential of the ferrocene shuttle is outside the potential of SEI formation.

In Chapter 3, we applied the ferrocene characterization method to SEIs formed on glassy carbon at 0.6 V *vs.* Li/Li^+ for neat and additive-containing electrolytes to investigate the enhancement provided by additive-formed SEIs (61). From the outset, we assumed two characteristics about the system. First, SEIs formed in additive-containing

electrolyte would improve capacity retention. That is, passivated glassy-carbon behaved similarly to graphite. Second, the ferrocene redox shuttle was analogous to a solvent molecule. We reported the counterintuitive result that passivation with additive-containing electrolytes was less effective in suppressing ferrocenium reduction than neat electrolyte, despite neat electrolyte reduction exhibiting a thicker SEI than that formed by additive-containing electrolyte reduction. Effectively, the benefits of additives were never observed in the system.

In this work, we extend the previous study to lower potentials to further explore the counter-intuitive findings observed in Chapter 3. First, we investigate the passivation behavior of neat and additive-containing electrolytes at lower potentials that are closer to practical LiB operation. If ferrocene exhibits similar transport and kinetics through the SEI as solvent, then the benefits of the additives should be observed at lower potentials, where LiBs tend to operate. Second, we examine the assumptions behind the ferrocene characterization method, by varying the concentration of bulk redox shuttle. In our previous work, we assumed that the ferrocene redox shuttle had negligible interaction with the SEI surface. Any interaction with the surface complicates analysis of ferrocene kinetics and transport and eventual determination of SEI growth mechanisms.

Experimental

Electrochemical experiments were conducted in a Teflon three-electrode cell, using an Autolab Metrohm Compact Potentiostat Model PGSTAT101. Potentiostatic holds, EIS, and cyclic voltammetry (CV) experiments were performed in an argon-atmosphere glovebox at room temperature. Inside of the glovebox, the three-electrode

cell was placed on vibration-damping mats (McMaster-Carr) to minimize convection from vibrations.

A chlorotrifluoroethylene (CTFE) shrouded glassy-carbon electrode, 3 mm in diameter, was used as the working electrode (Basi, Inc.). Lithium foil was used as both counter and reference electrodes (Sigma Aldrich). Three electrolytes were used to passivate the working electrode. Neat electrolyte contained 1:1 (by weight) ethylene carbonate: diethyl carbonate with 1 M $LiPF_6$ (BASF). Two separate additive containing electrolytes were prepared by adding 5 wt% FEC (Sigma Aldrich) or 5 wt% VC (Sigma Aldrich) to the neat electrolyte. VC additive was filtered in the glovebox before use to remove excess BHT stabilizer. The working electrode was separately passivated in 3 mL of neat, FEC-, and VC-containing electrolytes. Following passivation, the cell potential was allowed to rise to $\geq$ 2.7 V *vs.* Li/Li^+ over the course of approximately three hours. Then, 1 mL of a neat electrolyte solution containing approximately 6.1 and 7.4 mmol of ferrocene (Fc) and ferrocenium hexafluorophosphate (Fc^+) was added to the passivating electrolyte (Sigma Aldrich). After dilution, the final Fc and Fc^+ concentrations are 1.65 ± 0.1 mmol and 1.85 ± 0.1 mmol. The steady-state, equilibrium potential was approximately 3.241 V for the solution. Additionally, after the cell potential rise, the lithium foil counter electrode was replaced with a platinum coiled wire (Pine Instruments). The platinum coiled wire allowed the reverse reaction to occur to keep the concentration of redox species constant in the electrolyte.

EIS and CV scans were then performed on the system after reaching equilibrium. Equilibrium times ranged from several minutes to several hours. Any data not within

3.241 ± 0.005 V after addition of Fc/Fc^+ was discarded. EIS measurements were taken from 100 kHz to 10 mHz with a 5 mV perturbation around the working electrode equilibrium potential. Then, CV scans were taken at 1 mV-s^{-1} from 3.14 V to 3.34 V. EIS and CV scans were also taken of a pristine glassy-carbon electrode (Basi, Inc.) of 3 mm in diameter in contact with the electrolyte to measure the concentration of redox species in the electrolyte solution. All glassy-carbon electrodes were polished with 0.05 μm alumina solution (Pine Instruments) before passivation. EIS was performed prior to each potentiostatic hold to measure the high frequency resistance (HFR) of the electrode, which measured 16 ± 3 Ω-cm^2.

Experiments were performed to measure the thicknesses of SEIs formed in neat electrolyte. Polypropylene cells, approximately 2.0 mL in volume, were used for SEI formation experiments on glassy-carbon disc electrodes (Ted Pella, Inc.), with electrode surface area being limited by an O-ring (McMaster-Carr). After passivation, the glassy-carbon working electrode was then removed from the cell, separated from the O-ring, and gently rinsed with approximately 1 mL of DMC (Sigma Aldrich) to remove excess lithium salt. The electrode was dried > 1 hour in the antechamber of the glovebox and subsequently taken for analysis following the drying period. A focused ion beam + scanning electron microscope (FEI Nova Nanolab 200, gallium liquid metal ion source) was used to open a regular cross-sectional face by trench milling. The ion accelerating voltage was 30 kV and polishing cuts were made at approximately 30 pA. Following polishing, SEM images were taken at 5 kV. During transfer from the glovebox to the scanning electron microscope, the electrode was briefly exposed to oxygen and moisture from the air.

Model

Cyclic voltammetry and impedance model formulations are developed in Chapter 3.

Results

Pristine Electrode

In Figure 4.1, CV scans obtained on separate days at 1 mV-s^{-1} are given for a polished glassy-carbon electrode. Prior to the CV scan, the glassy-carbon electrode was passivated for several minutes and then subsequently polished with alumina paste. The experiment was repeated several times, of which two representative CV scans of the polished electrode, labeled A and B, are given. A simulated CV based on the Nernst equation is overlaid on the experimental voltammograms. Experimental conditions show good reproducibility from day to day. The Nernst equation, coupled with mass-transport expressions of the redox shuttle in the electrolyte, is used to obtain the simulated CV. Under Nernstian conditions, the concentrations are related to the cell potential by

$$E_{cell} = E^{0} + \frac{RT}{nF}\ln\left(\frac{c_o(0)}{c_r(0)}\right), \tag{4.1}$$

where E_{cell} is the reversible cell potential and E^0 is the standard potential for the reaction. As previously shown, Fc^+ reduction is a one-electron-transfer reaction, $n = 1$. For this one-electron-transfer reaction, the measured open-circuit potential is expected to be approximately 3.24 V *vs.* Li/Li^+ (44, 106). From the simulation, we infer that using alumina polish is indeed effective in removing surface films from the electrode after passivation. At high and low overpotentials away from equilibrium (approximately 3.24

V vs. Li/Li+), experimentally measured current densities are greater than those predicted by the Nernst equation. These differences are the result of natural convection in the cell causing changes to boundary layer thicknesses over the scan range.

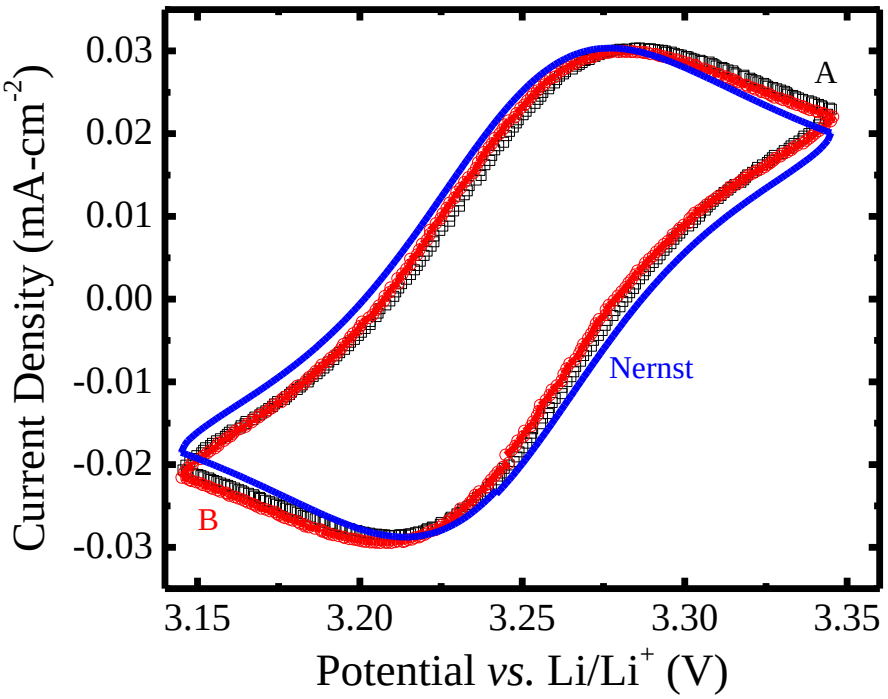

Figure 4.1. Experimental (A and B) and simulated (Nernst) CVs for a pristine glassy-carbon electrode with Fc/Fc^+ in the electrolyte. The CV scans are obtained at 1 mV-s^{-1}. Approximately 1.8 mmol and 1.6 mmol of Fc^+ and Fc, respectively, have been added to neat electrolyte. Day to day reproducibility of experimental voltammograms is good. A simulated CV is overlaid on the experimental CVs. The cleaning procedure is effective in restoring the electrode after passivation.

SEI Formation

After verifying the electrode cleaning procedure, the glassy-carbon electrode was passivated at 0.1 V and 0.3 V. These two potentials were selected based on the relevant

reduction peaks on CVs in Figure 3.2 for neat, FEC-, and VC-containing electrolytes (61). The CVs show several minor reduction peaks, but a particularly large peak was present near 0.4 V for each electrolyte.

In Figure 4.2, the formation charge is given as a function of time for 0.1 V and 0.3 V for neat and additive-containing electrolytes. The data is obtained by measuring the current density over the time of the experiment. The current density measurements can be prone to noise, particularly at extended hold times when the current is small, due to automated functions such as automatic switching of current range as a feature on the potentiostat. To smooth out the measured noise, the current density is integrated with respect to the hold time to obtain the formation charge density, $-q$. The final magnitude of formation charge, obtained from the final point on each formation charge curve, is also shown for all three potentials as individual data points. The measured q values range from approximately 3.5 mC-cm^{-2} to 12.5 mC-cm^{-2}.

There are similarities in the passivation curves trends at 0.1 V and 0.3 V for each electrolyte. First, the formation charge curves are parabolic with time. The same parabolic shape is found for the final formation charge values versus time. The parabolic shape of each of the q *vs.* t curves and final q value *vs.* t indicates that the passivation mechanisms are indeed similar. Second, the rate of passivation is greater at the lower reduction potential of 0.1 V. The result is only intuitive if we consider that SEI growth is not limited solely by solvent diffusion to the electrode surface. At 0.1 V the driving force for electrolyte reduction is greater than at 0.3 V, the more positive potential.

In contrast, there are several differences in the passivation trends observed at 0.1 V compared to those observed 0.3 V. First, we observe distinct differences in the passivation rates for neat and additive-containing electrolytes at 0.3 V. Both neat and FEC-containing electrolytes have similar q values for the same passivation times. In comparison, the q values for VC-containing electrolyte tend to be greater for the same amount of passivation time. The differences in q values suggests that a either physical properties of the formed SEIs are unique or that the passivation mechanisms are slightly different for each electrolyte. Second, the passivation curves appear less reproducible at 0.1 V with neat electrolyte than at 0.3 V. The lessened reproducibility is likely linked to the lower passivation potential. At lower potentials the driving force for reduction increases, likely changing the passivation mechanism or stability of the passivation products. Additionally, small changes in the reference electrode potential have a much larger impact on reduction rates than at 0.3 V and 0.6 V. Counterintuitively, we do not observe the same trends in FEC- and VC-containing electrolytes. Rather, the reproducibility of the curves appears to remain consistent for FEC-containing electrolyte and actually improves for VC-containing electrolyte. The deviation of passivation trends at 0.1 V, compared to 0.3 V, indicates that potential and electrolyte have a coupled influence on the rate of passivation.

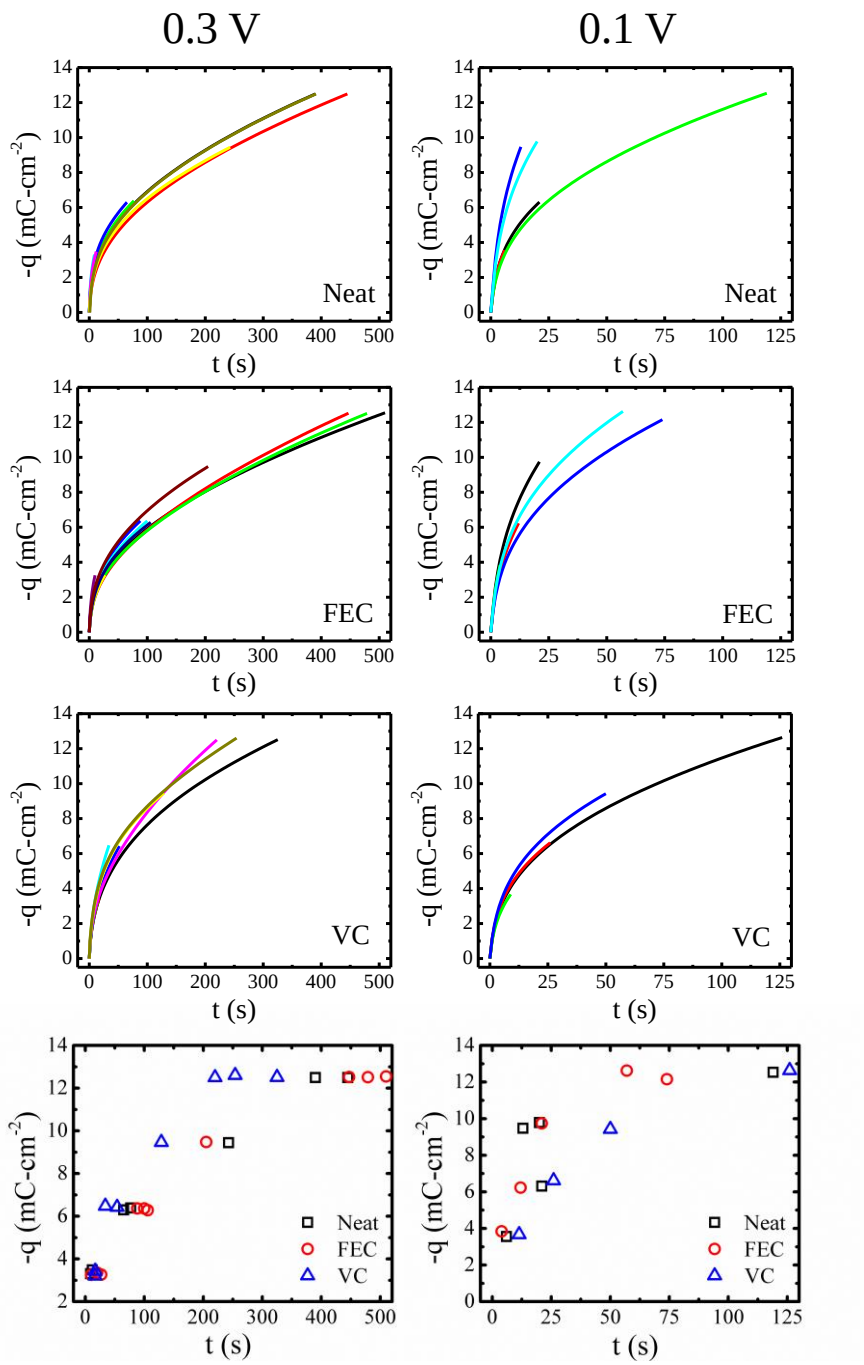

Figure 4.2. Formation charge measurement at 0.1 V and 0.3 V. Multiple experiments for neat, FEC-, and VC-containing electrolytes are shown at each potential. Figures in each column are measured at the labeled potential. The final point from each formation charge curve is shown as the last subfigure in each column. The shape of the curves over the sampled time is parabolic, independent of the electrolyte. The final points from the formation charge curve experiments are also parabolic with time.

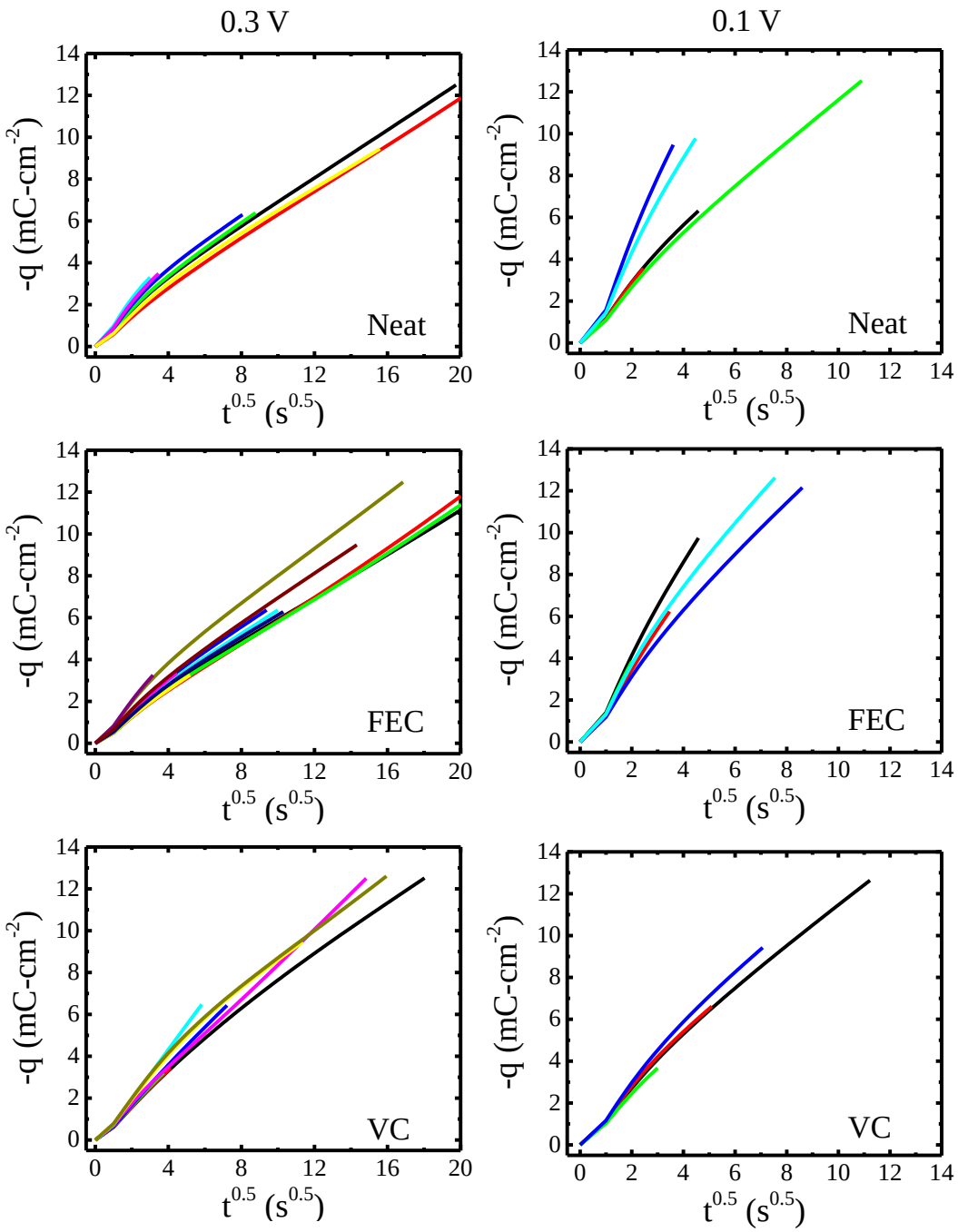

Figure 4.3. The linear dependence of the formation charge *vs.* $\sqrt{t}$ at 0.1 V and 0.3 V *vs.* Li/Li$^+$. Multiple experiments for neat, FEC-, and VC-containing electrolytes are shown at each potential. Figures in each column are measured at the labeled potential.

In Figure 4.3, the formation charge data provided in Figure 4.2 are cast against the square root of time. For each electrolyte at both potentials, the formation charge appears to scale linearly with the square root of time. There are bends in the data for all samples at approximately 1 second. The different slopes of the formation charge lines before and after 1 second are partially attributable to charging of the double-layer capacitor and electrolyte resistance from the working to reference electrodes. After approximately 1 second, the data scales relatively linearly with the square root of time with a different slope. Several of the formation charge curves have a slightly curved appearance. We suspect that the curvature is likely the result of convection in the cell or an incompletely formed SEI. Any convection or incompletely formed SEIs would cause the diffusion of soluble SEI products away from the surface. The diffusion of these species from the surface would create void space at the surface for undersirable SEI formation reactions.

Thus far, we have observed a parabolic growth rate of the SEI at each potential and electrolyte. The growth rate scales linearly with the square root of time for each sample shown. Additionally, it appears that each electrolyte causes unique characteristics when comparing their respective formation charge curves. The parabolic growth rate and linear square root of time dependence indicates a transport limited growth mechanism. For a single-layer representation of the SEI, the rate of growth of the SEI is given as

$$\frac{dL_p}{dt} = \frac{M\ (1-\varepsilon_p)}{nF\ \rho} i\ , \tag{4.2}$$

where L_p is the thickness of the single layer, M is the molecular weight, ε_p is the porosity, F is Faraday's constant, ρ is the density of the SEI, n is the number of electrons

transferred, and i is the current density that forms the SEI. Assuming that only L_p and i are functions of time, integration of equation (4.2) gives the thickness in terms of the formation charge Q as

$$L_p = \frac{M\ (1 - \varepsilon_p)}{nF\ \rho} Q\ . \tag{4.3}$$

That is, for a constant porosity SEI, the thickness of the SEI scales with the formation charge.

Ploehn *et al.* showed that, for a solvent diffusion limited system, the thickness of the SEI scales with the square root of time (71). They assumed that a thin surface layer exists on the electrode surface so that solvent is not always present for reduction. Likewise, Peled showed that by assuming migration or diffusion of electrons across the SEI limited growth, the thickness of the SEI would then scale with the square root of time (4). The linear scaling of the formation charge experiments with the square root of time suggests that SEI growth is limited by the transport of electrons or solvent at both potentials for all electrolytes. Therefore, we infer that the passivation mechanisms for each electrolyte are the same.

In Figure 4.3, representative impedance responses of Fc/Fc^+, measured at 0.3 V, are given for neat, FEC-, and VC-containing electrolytes. Both Nyquist- and Bode-plot formats are provided for each electrolyte for the measured passivation charge. The impedance spectra include the same features as in Figure 3.8(a) and Figure 3.8(b). In Nyquist-plot format, each spectrum contains at least one arc at high frequencies and a

second lower frequency arc that tends to increase in width with more formation charge. The low frequency end of each spectrum bends into the shape of a 45-degree line. This low-frequency portion of the spectrum is a result of bulk electrolyte semi-infinite diffusion of Fc/Fc^+. The magnitude of the high frequency intercept is determined by the solution resistance, measured between the working and reference electrodes, prior to the experiment. The high frequency resistance remains unchanged after passivating the surface. In Bode-plot format, the magnitude of the impedance increases with more passivation charge for all electrolytes. The result is intuitive, as a longer hold time allows for the passage of more formation charge. Additive-containing electrolyte appears to passivate the surface less than neat electrolyte, based on the magnitude of the impedance.

The trends of increasing passivation time and increasing impedance for each electrolyte are in agreement with our previous findings at 0.6 V. However, the result is still counterintuitive. To examine this assertion, we revisit our assumptions. From the outset, we have first assumed that if Fc/Fc^+ is analogous to solvent molecules. Second, we assume that additive-containing electrolyte should better passivate the surface than neat electrolyte. That is, we expect more Fc/Fc^+ kinetic and transport resistance for the same magnitude of passivation for additive-containing electrolytes . The results for this system indicate that, despite the same magnitude of passivation, the additives are not effective in passivating the surface. Rather, the benefits of additives are not observed in the impedance responses in Figure 4.3.

In Figure 4.5, representative impedance responses of the ferrocene redox shuttle, measured at 0.1 V, are given for neat, FEC-, and VC-containing electrolytes. Both

Nyquist- and Bode-plot formats are provided for each electrolyte for the measured passivation charge. Several of the same characteristics of the impedance spectra measured at 0.3 V are observable at 0.1 V. First, the same high frequency behavior observed at 0.3 V is observed at 0.1 V. The high frequency resistance remains constant with increasing passivation time. Second, each impedance spectrum contains a single arc or multiple arcs for kinetic and mass-transport resistances. A low frequency bulk Fc/Fc^+ transport tail is also observed in some of the low frequency data. Third, in both Nyquist- and Bode-plot formats, the impedance increases with increasing amounts of surface passivation. Fourth, the benefits of additives are never truly observed in the system, even at 0.1 V. Additive-containing electrolytes never passivate the surface more effectively than neat-electrolyte. Rather, the electrolytes tend to exhibit similar magnitudes of impedance for the same amount of formation charge. Again, the result is counterintuitive but is consistent with the observations at 0.6 V and 0.3 V *vs.* Li/Li^+.

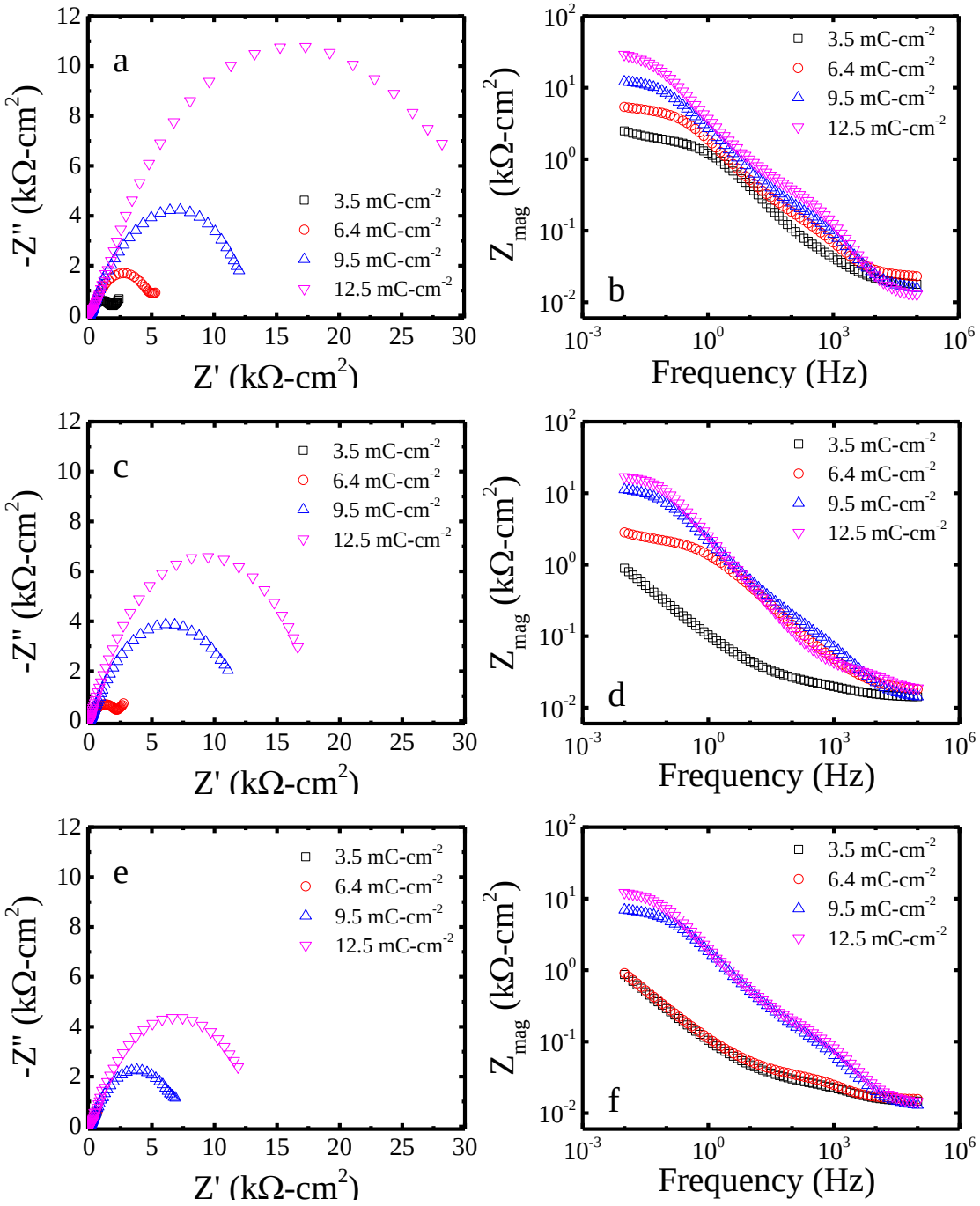

Figure 4.4. Impedance responses of Fc/Fc^{+}after passivation at 0.3 V *vs.* Li/Li^{+}. Both Nyquist and Bode plots are shown for neat, FEC-, and VC-containing electrolytes. Four formation charges are shown. (a) and (b) correspond to neat electrolyte, (c) and (d) correspond to FEC-containing electrolyte, and (e) and (f) correspond to VC-containing electrolyte. The magnitude of the impedance increases with increasing

passivation time for all electrolytes. However, additive-containing electrolyte appears to be less effective at passivating the surface than neat electrolyte.

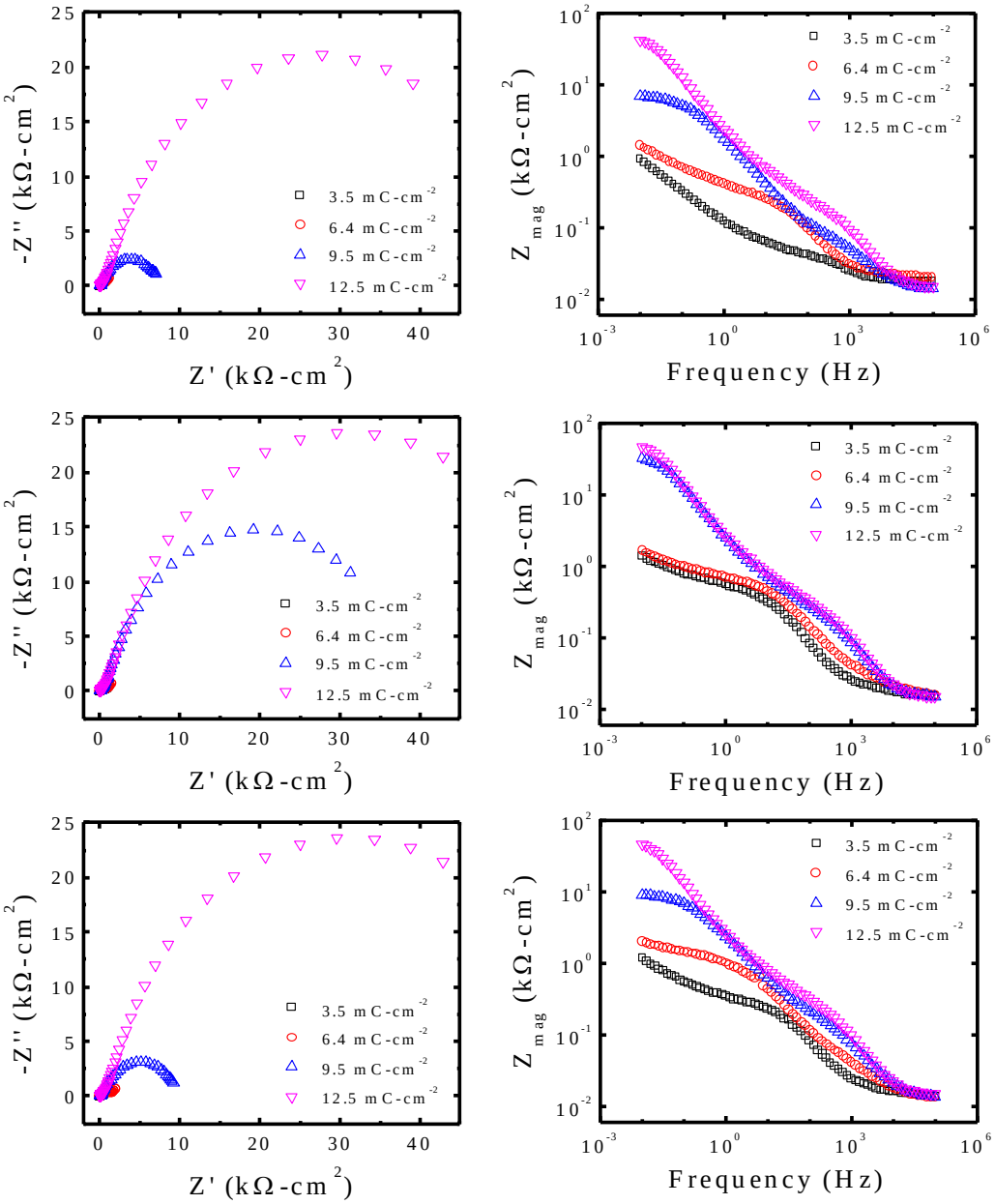

Figure 4.5. Impedance responses of Fc/Fc^+ after passivation at 0.1 V *vs.* Li/Li^+. Both Nyquist and Bode plots are shown for neat, FEC-, and VC-containing electrolytes. Four formation charges are shown. (a) and (b) correspond to neat electrolyte, (c) and (d) correspond to FEC-containing electrolyte, and (e) and (f) correspond to VC-containing electrolyte. The magnitude of the impedance increases with increasing

passivation time for all electrolytes. However, additive-containing electrolyte appears, at best, to be equally passivating as neat electrolyte.

In Figure 4.6, the average slopes of the linear formation charge curves in Figure 4.3 are given versus the passivation potential. Values at 0.6 V are also measured linear formation charge curves obtained at 0.6 V. The slopes are obtained by averaging the individual passivation experiments at each potential for the listed electrolyte. We observe that, the slopes increase with decreasing passivation potential for each electrolyte. From the observed relationship between slope of the formation charge curves and potential, we infer that growth of the SEI is not limited by mass transfer of solvent alone. Electron transport influences the rate of SEI formation over this potential range. We note that the slopes appear significantly different at 0.1 V for VC-containing electrolyte than neat and FEC-containing electrolyte. However, due to the passivation rate, the experimental uncertainty in the measurements is significantly increased.

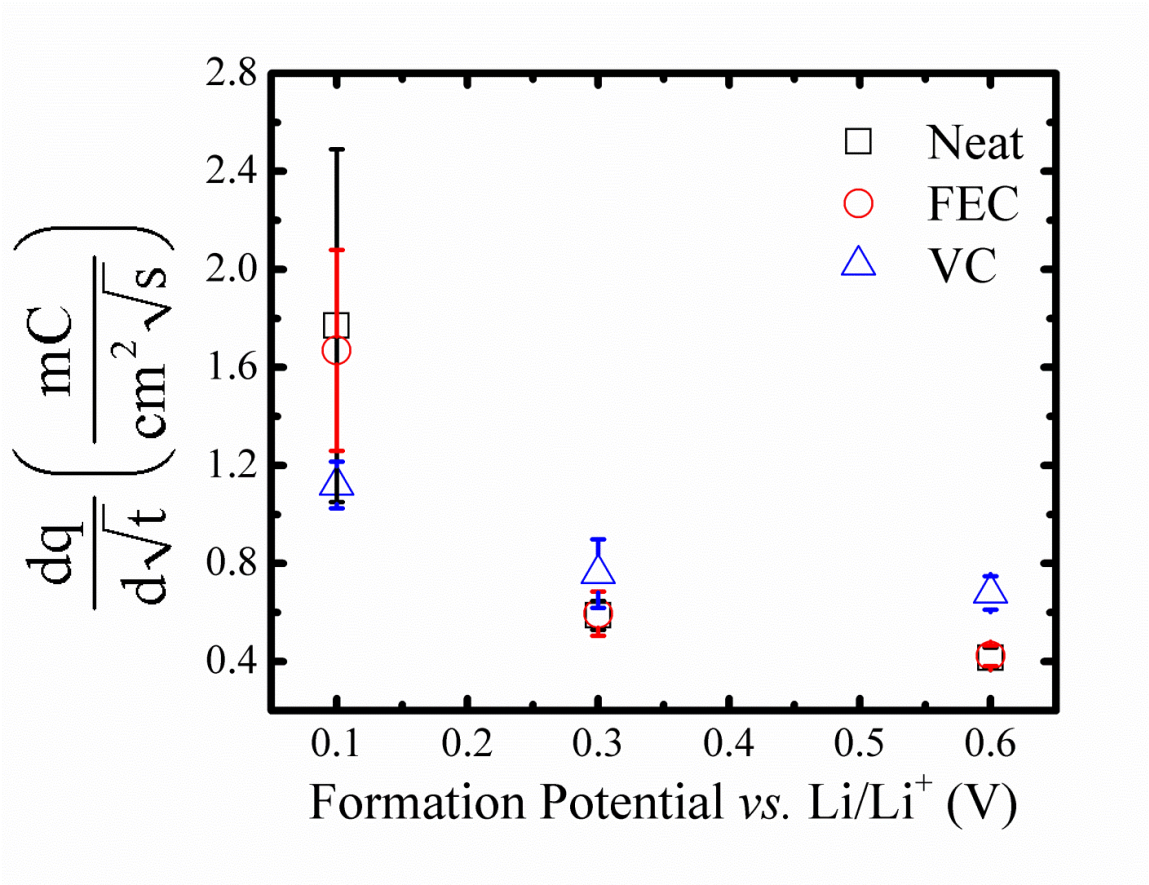

Figure 4.6. Average slope of formation charge vs. the square root of time. Neat, FEC-containing, and VC-containing electrolyte passivation slopes are calculated at 0.1 V, 0.3 V, and 0.6 V. The 0.6 V slopes are obtained from experimental data, shown in Figure 3.3(b). Neat and FEC-containing electrolyte tend to similar average slopes. VC-containing electrolyte is markedly different in average slope. The data suggests that formation is not only limited by rates of mass-transfer of solvent through the SEI.

The Validity of the Bruggeman Relation

In Chapter 3, we observed that Fc/Fc^+ transport through a porous SEI led to the formation of a low frequency mass-transport arc in the Nyquist plot of the impedance spectrum. To quantify the changes in the SEI for different magnitudes of passivation, we developed a mathematical model to obtain fitted parameters from the low frequency

mass-transport arc of the impedance reponse. The through film Fc/Fc^+ flux with Fick's law, was defined with an effective diffusivity of both species in the redox couple. Furthermore, the effective diffusivity of both Fc/Fc^+ includes a correction for the porosity and tortuosity of the film. We invoked a common simplication made in battery literature, the Bruggeman relation, to uniquely define the porosity and tortuosity. However, as shown in Figure 3.9 and Figure 3.11, there was a significant difference in the magnitude of the model-fitted and experimentally-measured thicknesses for a ten minute passivation time at 0.6 V. In this section, we attempt to resolve this difference by exploring the applicability of the Bruggeman relation and adsorption of Fc/Fc^+ on the surface of the porous SEI.

In Figure 4.7(a), an SEM image is provided of a glassy-carbon electrode passivated for 10 minutes in neat electrolyte at 0.3 V. The image confirms the presence of an SEI, approximately 500 nm in thickness, on the glassy-carbon surface. The observed SEI is surprisingly thick and appears to be physically homogenous, which is in agreement with our previous findings (61). In comparison, model thicknesses obtained from a fit of the impedance spectrum predict the SEI thickness to be at least one order of magnitude greater.

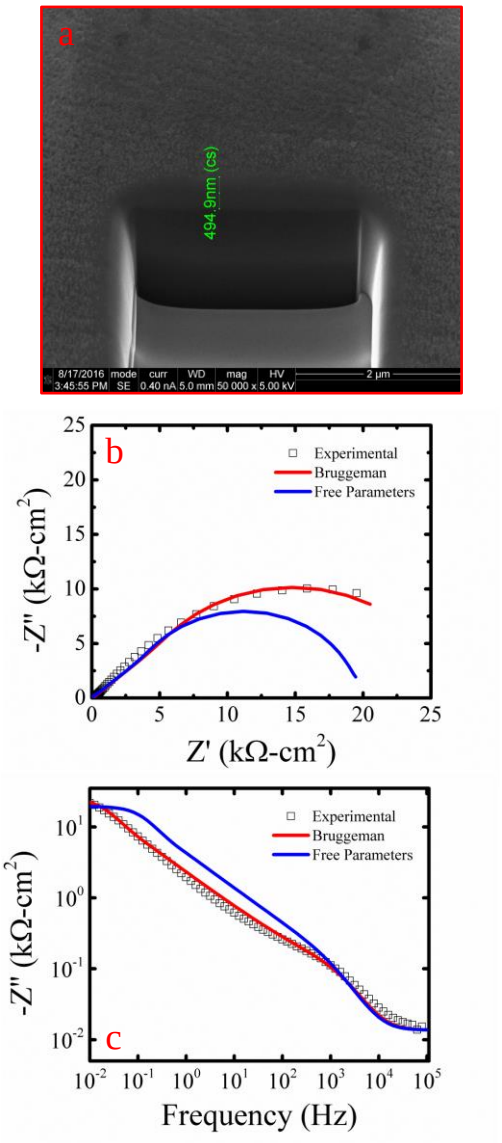

Figure 4.7. SEM image of a glassy-carbon electrode with SEI and Nyquist and Bode plots of Fc/Fc^{+} under the same passivation conditions. (a) The electrode is passivated in neat electrolyte for 10 minutes at 0.3 V. The SEI appears structurally homogeneous and approximately 500 nm in thickness. (b) Nyquist plot and (c) Bode plot of the impedance response with simulation results overlaid. simulation results are overlaid on experimental data. The Bruggeman relation only effectively represents the data when the SEI thickness is set to 31 µm. For a description of the labels "Bruggeman" and "Free Parameters," see text.

In Figure 4.7(b), multiple data fittings are overlaid on the measured impedance spectra for a ten minute hold on glassy-carbon in neat electrolyte. There are two fits of the data shown. The first fitting uses the Bruggeman relation. Under the conditions of this fitting, $L_p = 31\times10^{-6}$ m, $\varepsilon_p = 0.07$, and $\tau_p = 3.7$. Therefore, the fitted thickness is 60 times greater than the experimentally observed thickness measurement, which implies that there is an inadequacy in the model formulation.

The second fit is labeled "Free Parameters" and uses the thickness obtained from SEM measurements, 500 nm, as that of the porous layer. Then, the porosity and tortuosity are fitted as free variables. Through the simulation, we find that there are no reasonable values of porosity that allow the simulation to fit the experimental data. The conditions for the simulation are $\varepsilon_p = 1$ and $\tau_p = 2800$. Any values less than $\varepsilon_p = 1$ worsen the simulation and experimental agreement. For a good fit, the 500 nm thickness of the SEI requires that the void fraction of the porous layer exceed unity. Obviously, the porosity of the system cannot be larger than unity. The requirement that $\varepsilon_p > 1$ is because of the low characteristic frequency (<100 mHz) of the mass-transport arc in the experimental data.

Because both the resistance and capacitance of the layer determine the characteristic frequency of the mass-transport arc, we expect more capacitance to shift the characteristic frequency to lower frequencies. The in-pore concentration of Fc^+ is $\varepsilon_p c_{Fe^+}$, and the porosity exceeding a value of 1 indicates a greater than expected concentration of Fc/Fc^+. From these relationships between in-pore concentration

capacitance and the mass-transport arc, we infer that another phenomenon is the source of the additional Fc/Fc^+ needed to shift the low frequency response.

In Figure 4.8, the relationship between the characteristic frequency of the Fc^+ mass-transport process and bulk Fc^+ concentration is explored. Representative impedance responses of Fc/Fc^+ after passivation in neat, FEC-, and VC-containing passivated glassy-carbon samples are given. The samples were passivated for 10 minutes at 0.3 V. The experiments were repeated twice for each sample to ensure reproducibility.

Following passivation, Fc/Fc^+ was added to the electrolyte, and the cell was allowed to come to equilibrium. The impedance response of the passivated glassy-carbon electrode was then measured. A CV of a pristine glassy-carbon electrode was used to obtain the redox shuttle concentration in the electrolyte. The concentration of redox shuttle was gradually increased with time. After each increase, the impedance response was again measured at the equilibrium open-circuit voltage. The concentration of redox shuttle was determined from a CV of a separate pristine glassy-carbon electrode in the shuttle-containing electrolyte after an addition of redox shuttle.

As in Figure 3.6, the Nyquist plot of the response contains two arcs. The first arc is visible if the real and imaginary axes were to be expanded and is assigned to Fc/Fc^+ kinetics. The second arc is Fc/Fc^+ mass-transport process through the SEI. The characteristic frequency of the mass transport process is represented by the topmost point of the mass-transport arc in the Nyquist plot. The impedance responses include a label, $f_{c,}$ which is representative of this characteristic frequency. A summary of the characteristic frequencies measured against bulk Fc^+ concentration for each electrolyte is provided.

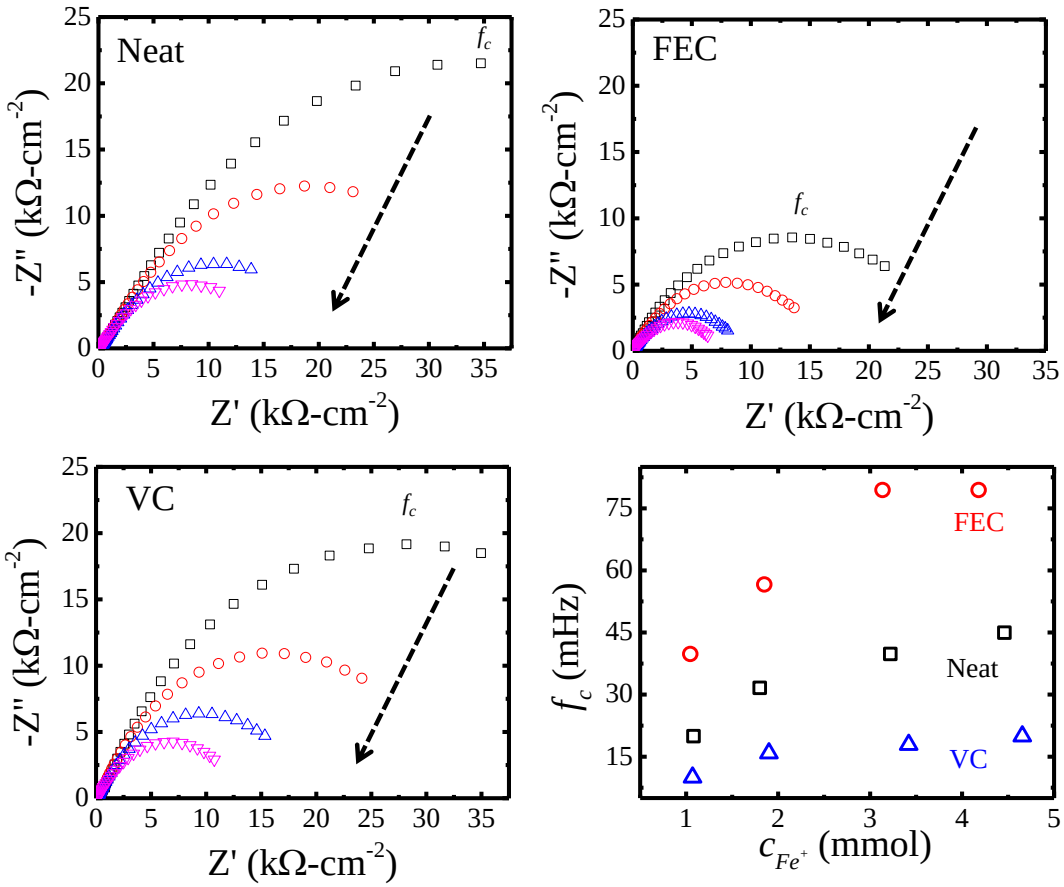

Figure 4.8. Characteristic frequency and bulk Fc^+ concentration relationship. The impedance response of 10 min passivated samples at 0.3 V is given. The concentration of Fc^+ is increased and measurements are obtained at approximately 3.241 V for all samples. Measurements for neat, FEC-, and VC-containing electrolytes are provided. The characteristic frequency is labelled 'f_c.' A downward pointing arrow is shown in the direction of increasing Fc^+ concentration. There is a noticeable shift in the characteristic frequency with increasing concentration, suggesting adsorption of Fc^+ on the formed SEI.

There are significant changes observed in the impedance spectra with increases in concentration. The low-frequency mass-transport arc width decreases with increasing concentration. The result is expected, as the arc width is proportional to the inverse of the bulk concentration of Fc^+,

$$R_p = \frac{1}{c_{Fc^+,bulk}} \frac{RT}{F^2} \frac{L_p \tau_p}{D_{Fc^+,bulk} \varepsilon_p}, \tag{4.4}$$

where R_p is the arc width.

In each electrolyte, by changing the bulk Fc/Fc+ concentrations, we observe a shift in the characteristic frequency of the mass-transport arc. The characteristic frequency of the mass-transport process changes by a factor of two, from the first bulk concentration to the last bulk concentration. Eventually, the characteristic frequency plateaus with increasing concentration, indicating that bulk concentration changes are no longer affecting the transport process. That is, the magnitude of the contributing effect plateaus. In our current model formulation, changes in the bulk concentration do not cause a shift of the characteristic frequency, except in the case that the ratio of the Fe/Fc^+ significantly changes in the bulk. A large change in the bulk concentration ratio would be observed in changes in the open-circuit potential, which is governed by the Nernst equation. However, we did not observe changes in the open-circuit potential after the addition of redox shuttle.

The change in the characteristic frequency with concentration indicates that there is a surface adsorption interaction of Fc^+ with the SEI. The shape of the characteristic frequency profile is analogous to an adsorption isotherm. With increasing concentration, more Fc^+ is adsorbed onto the surface of the porous SEI, until the surface is saturated. At saturation, there are less additional vacant adsorption sites for bulk Fc^+.

To test this surface adsorption hypothesis, we amend the material balance for Fc^+ in the porous SEI to include the effects of adsorption of Fc^+. From the outset, we assume

that the bulk Fc^+ is in constant thermodynamic equilibrium with the bulk concentration. That is, there are no rate limitations for adsorption and desorption of Fc^+. The modified material balance of Fc^+ in the SEI is given as

$$\frac{\partial \varepsilon_p c_{Fc^+}}{\partial t} = D \frac{\varepsilon_p}{\tau_p} \frac{\partial^2 c_{Fc^+}}{\partial x^2} - a_p \frac{\partial Q_p}{\partial t}. \tag{4.5}$$

The last term in equation (4.5) is the adsorption correction. The term is defined by two parameters. The first parameter, a_p, represents the specific interfacial area of the SEI and is a ratio of real surface area of SEI to total volume of SEI. The second parameter is Q_p, which represents the moles of Fc^+ adsorbed on the SEI per unit real surface area of SEI. The entire term is analogous to the accumulation term in the material balance. Rearranging equation (4.5) leads to

$$\left(\varepsilon_p + a_p \frac{dQ_p}{dc_{Fc^+}} \right) \frac{\partial c_{Fc^+}}{\partial t} = D \frac{\varepsilon_p}{\tau_p} \frac{\partial^2 c_{Fc^+}}{\partial x^2}. \tag{4.6}$$

We can only speculate on the exact shape of the $\frac{dQ_p}{dc_{Fc^+}}$ adsorption profile from Figure 4.8. The slope is originally the largest in magnitude at low concentrations and approaches 0 at towards the saturation concentration. Therefore, at low concentrations where saturation of the vacant adsorption sites is not observed, the magnitude of $\frac{dQ_p}{dc_{Fe^+}}$ is largest. Because there is no practical method to determine the actual surface area of the SEI, the specific interfacial area term is lumped into the slope of the adsorption profile. Linearizing and perturbing equation (4.6) leads to

$$\left(\varepsilon_p + a_p \frac{dQ_p}{dc_{Fc^+}} \right) \frac{\partial \tilde{c}_{Fc^+} \exp(j\omega t)}{\partial t} = D \frac{\varepsilon_p}{\tau_p} \frac{\partial^2 \tilde{c}_{Fc^+} \exp(j\omega t)}{\partial x^2}. \quad (4.7)$$

In Figure 4.9, simulated impedance responses using the adsorption parameter are overlaid on the experimental impedance responses obtained in Figure 4.8 for neat electrolyte. All equations in the model formulation remain unaltered except the material balance, which is replaced with equation (4.7). There are two experimental constraints available for data analysis, the arc width and the characteristic frequency. Previously, the thickness of the SEI, porosity, and tortuosity of the SEI were three fitted parameters obtained from the two experimental constraints. The assumption for the fitting was that the Bruggeman relation defined the relationship between porosity and tortuosity. However, we have shown the Bruggeman relation does not apply for the SEI in this system, and now we have incorporated an additional fitting parameter, $\frac{\partial Q_p}{\partial c_{Fc^+}}$. With the additional fitting parameter, there are two parameters that must be set. From the SEM imaging in Figure 4.7, the SEI thickness, L_p, is set to 500 nm. The porosity is set from the three remaining parameters. We choose the porosity because the tortuosity uniquely affects the arc width, and the fitting parameter is a newly defined parameter. To our knowledge, there are no measurements of the porosity of the SEI in the literature. For the purposes of this simulation, we assume that $\varepsilon_p = 0.3$.

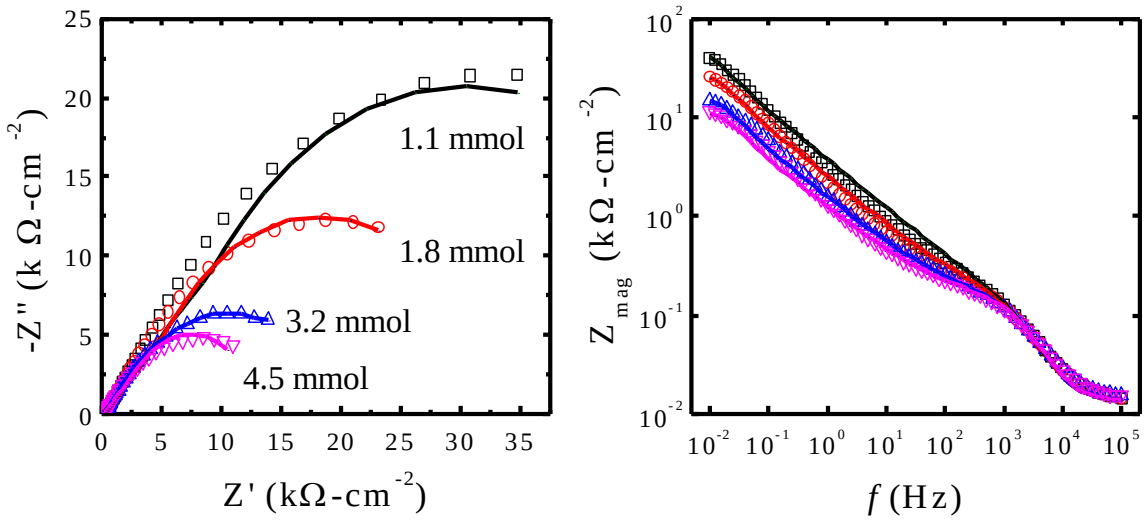

Figure 4.9. Nyquist and Bode plots of the impedance response of the Fc/Fc^+ after 10 minutes of passivation at 0.3 V in neat electrolyte, with simulation results overlaid. The adsorption fitting parameter, $\frac{dQ}{dc_{Fc+}}$ is changed amongst simulations. $\frac{dQ}{dc_{Fc+}}$ is 5.8 (squares), 4.7 (circles), 4 (upward triangles), and 3.6 (downward triangles).

τ_p and dQ_p/dc_{Fc^+} are fitted to the arc width and frequency of the impedance response. The tortuosity is a structural parameter and should remain constant with changes in the bulk concentration of Fc/Fc^+. The value of the tortuosity is approximately 1100 in each simulation. The parameter value is two orders of magnitude greater than typically reported for graphite porous electrodes (113). However, because graphite composite electrodes are structurally composed of particles, a direct comparison is invalid. Rather, the unexpectedly high value of tortuosity could be possible if the pore spaces were not interconnected over the length of the porous SEI. In this case, regions disconnected from the majority of the pores of the SEI would represent paths of infinite

tortuosity. Averaged over the entire thickness, these regions of infinite porosity could then drastically increase the observed value of the tortuosity.

The adsorption parameter is at a maximum value at the lowest concentration of bulk Fc^+ and gradually decreases with increasing bulk Fc^+ concentration. The adsorption parameter allows for a better fit of the experimental data by shifting the characteristic frequency of the mass-transport process. However, the value never reaches zero over the experimental range of bulk Fc^+ concentrations despite df_c/dc_{Fc^+} appearing to approaching zero in Figure 4.8. There are two possible explanations for the non-zero value of the parameter. First, the concentration range over which bulk Fc^+ is varied is too narrow. For example, if the maximum concentration of bulk Fc^+ was increased an order of magnitude, we might still observe a shift in the characteristic frequency. This result would indicate that the saturation concentration of bulk Fc^+ was not reached over the concentration range tested in Figure 4.8. Second, the resolution of the points between frequency measurements is too low. The discrete values of the frequency likely require that additional points be sampled in the range for better resolution of changes in the characteristic frequency with increases in the bulk Fc/Fc^+ concentration.

Conclusion

SEIs were formed on glassy-carbon electrodes to investigate if potential influenced the passivation characteristics of neat and additive-containing electrolytes. Lowering the formation potential led to faster passivation of the glassy-carbon electrode for all electrolytes. The formation charge was determined parabolic with time for all

electrolytes at all potentials. Impedance responses measurements at 0.3 V and 0.1 V showed that the benefits of additives were not observed at either potential.

The formation charge was found to scale linearly with the square root of time, indicating transport limited growth for each electrolyte. The average slope of the linear formation charge curves increased with decreasing potential, indicating electrons influence SEI growth rates. It appears that the ferrocene redox couple is not a good representation of solvent molecules.

SEI thickness measurements obtained from FIB+SEM, coupled with experimental impedance responses under the same SEI formation conditions, prove that the Bruggeman relation is not sufficient in defining a relationship between porosity and tortuosity for this system. Varying the concentration of Fc^+ in the electrolyte indicates that adsorption of Fc^+ on the SEI surface acts to shift the characteristic frequency of the mass-transport arc. Incorporating the adsorption effect into the model allows for better Nyquist and Bode plot fittings and should be considered when fitting experimental data with an impedance response model. The values of tortuosity are found to be two orders of magnitude greater than those observed in porous electrodes, suggesting that some pores are not interconnected with the remainder of the SEI.

References

1. D. Aurbach, K. Gamolsky, B. Markovsky, Y. Gofer, M. Schmidt and U. Heider, *Electrochimica Acta*, **47**, 1423 (2002).

2. Y. Yamada, Y. Takazawa, K. Miyazaki and T. Abe, *The Journal of Physical Chemistry C*, **114**, 11680 (2010).

3. E. Markevich, G. Salitra, K. Fridman, R. Sharabi, G. Gershinsky, A. Garsuch, G. Semrau, M. A. Schmidt and D. Aurbach, *Langmuir* (2014).

4. C. C. Nguyen and B. L. Lucht, *Journal of the Electrochemical Society*, **161**, A1933 (2014).

5. M.-H. Ryou, G.-B. Han, Y. M. Lee, J.-N. Lee, D. J. Lee, Y. O. Yoon and J.-K. Park, *Electrochimica Acta*, **55**, 2073 (2010).

6. M. Nie, J. Demeaux, B. T. Young, D. R. Heskett, Y. Chen, A. Bose, J. C. Woicik and B. L. Lucht, *Journal of the Electrochemical Society*, **162**, A7008 (2015).

7. H. Shin, J. Park, A. M. Sastry and W. Lu, *Journal of the Electrochemical Society*, **162**, A1683 (2015).

8. L. Liao, P. Zuo, Y. Ma, Y. An, G. Yin and Y. Gao, *Electrochimica Acta*, **74**, 260 (2012).

9. M. Tang, S. Lu and J. Newman, *Journal of the Electrochemical Society*, **159**, A1775 (2012).

10. M. Tang, K. Miyazaki, T. Abe and J. Newman, *Journal of the Electrochemical Society*, **159**, A634 (2012).

11. M. Tang and J. Newman, *Journal of the Electrochemical Society*, **158**, A530 (2011).

12. M. Tang and J. Newman, *Journal of the Electrochemical Society*, **159**, A281 (2012).

13. R. R. Jaini, B. P. Setzler, A. G. Star and T. F. Fuller, *Journal of the Electrochemical Society*, **163**, A2185 (2016).

14. C. O. Laoire, E. Plichta, M. Hendrickson, S. Mukerjee and K. M. Abraham, *Electrochimica Acta*, **54**, 6560 (2009).

15. H. J. Ploehn, P. Ramadass and R. E. White, *Journal of the Electrochemical Society*, **151**, A456 (2004).

16. E. Peled, *Journal of the Electrochemical Society*, **126**, 2047 (1979).

17. J. D. Fairweather, D. Spernjak, A. Z. Weber, D. Harvey, S. Wessel, D. S. Hussey, D. L. Jacobson, K. Artyushkova, R. Mukundan and R. L. Borup, *Journal of the Electrochemical Society*, **160**, F980 (2013).

18. B. Tjaden, S. J. Cooper, D. J. L. Brett, D. Kramer and P. R. Shearing, *Current Opinion in Chemical Engineering*, **12**, 44 (2016).

19. T. DuBeshter, P. K. Sinha, A. Sakars, G. W. Fly and J. Jorne, *Journal of the Electrochemical Society*, **161**, A599 (2014).

CHAPTER 5

A PHYSICS-BASED MODEL OF THE IMPEDANCE RESPONSE OF A GRAPHITE|LINMC CELL

Introduction

Rechargeable lithium ion cells are extensively used in commercial markets for applications ranging from powering mobile phones to powering satellites (1). The popularity of these batteries results from their high energy densities and theoretical capacities, environmentally friendly components, potentially low costs, and long cycling life (2). There exists a multitude of materials that have been developed to meet the wide range of applications. Each of these materials has a different specific capacity (Ah/g), specific energy (Wh/g), cycle stability, and safety limitations, and is typically selected to meet the requirements of the application. An array of experimental techniques has been developed to characterize the performance of the cell. Accurate characterization of the material properties is critical to ensure that the optimal electrode chemistry is chosen to meet the needs of the application.

Electrochemical impedance spectroscopy (EIS) is a fast, *in situ*, and non-destructive technique for characterizing electrochemical systems. In EIS, the system is perturbed from the steady-state condition by applying a small perturbation to the voltage or current and measuring the response. The impedance is defined as the ratio of the voltage to current response. The system is perturbed over a range of frequencies, and the impedance is measured at each frequency in the range. Impedance data are frequently

represented in formats to provide insight into governing physical processes and allow for a separation of time constants for multiple physical processes based on the frequency measurement. However, several processes with similar time constants exist in cells that complicate the interpretation of impedance spectra.

The difficulties in interpreting impedance spectra arise because of numerous physical processes occurring within the cell having similar time constants. Examples of overlapping processes include lithium transport through the solid electrolyte interphase (SEI), electrode double-layer charging, lithium transport in the electrolyte solution, and solid-phase lithium transport. Additionally, experimental evidence suggests that the high frequency and mid-frequency processes in lithium ion battery impedance spectra are dominated by transport through the SEI (28, 61, 79, 114).

Interpretation of impedance measurements are most commonly resolved by equivalent circuit analogs. This method requires assumption of the physics of the processes involved, potentially leading to multiple interpretations during data fitting and subsequent difficulty in relating the chosen circuit to measureable physical parameters (diffusivities, conductivities, porosities, etc.).

Physics-based impedance models offer a more fundamental method to interpret experimental impedance data. These physics-based electrode models are convenient in relating the measured impedance response to fundamental physical parameters and can be easily modified to capture non-ideal impedance responses. In some cases, the models are used for parametric studies, with intent on distinguishing the overlapping physical processes that influence the impedance response. In other cases, the models are utilized

to fit experimental impedance spectra, with the intent of elucidating the causes of cell degradation.

Several groups have developed physics-based models to simulate the impedance response of single or dual-lithium ion insertion cells for parametric study or towards the incorporation of additional physics-based effects. Doyle *et al.* developed an impedance model that incorporated a full-cell sandwich macroscopic model based on porous electrode and concentrated solution theory (87). Their model described transport and kinetics in a lithium polymer cell with one insertion electrode. They concluded that the interpretation of the low frequency portion of impedance spectra can be complicated by overlapping time constants from electrode processes. Because of the overlapping processes, extraction of the solid-phase diffusivity requires impedance data at low enough frequencies such that solid diffusion is the dominating impedance at the measured frequencies. Meyers *et al.* developed an impedance model for a porous electrode that incorporated particle size distribution and a surface film (115). The model did not consider solution phase diffusion limitations. They found the impedance simulations were useful in qualitatively discussing interfacial and solid phase diffusion processes. They also note that the contributions from particle size distributions influence the magnitude of the low frequency impedance response. Devan *et al.* presented the analytical solution of the impedance response of a single porous electrode with linear kinetics and solution phase concentration gradients present (96). The analytical expression showed that, for a particular set of physical parameters, solution phase concentration gradients manifest at low frequencies. More recently, Gambhire *et al.* developed an impedance model that incorporated particles that underwent phase

transitions (83). They found that phase transitions caused distinctions in the low-frequency impedance response that were useful in estimating the battery state of charge. Chen *et al.* simulated the impedance response for a porous electrode with various active material morphologies and constructed microstructures (80). The generated microstructures were then defined in terms of their physical properties and parameterized as impedance model inputs. They found that the coupled effect of particle shape and electrode microstructure alters the impedance response over the entire frequency spectrum.

Other groups have utilized impedance models to extract physical parameters in the interest of analyzing cell performance. Dees *et al.* investigated the post-cycling impedance response of an $LiNi_{0.80}Co_{0.15}Al_{0.05}O_2$ (LiNCA) anode (81). Microscopic imaging of cycled particles indicated the presence of a second outer layer composed primarily of nickel that was believed to form during the cycling process. Experimental EIS measurements of the LiNCA electrode suggested the presence of an additional capacitive loop present at high frequencies. The new capacitive loop was attributed to lithium transport within the modified surface layer. After modifying the model to include transport through a second outer layer on the particle, they successfully observed an additional capacitive loop on the simulated impedance spectra. Abraham *et al.* used an impedance model to obtain physical parameters for a $LiNi_{0.80}Co_{0.15}Al_{0.05}O_2$ cathode (116). They extracted lithium diffusion coefficients in the solid phase and kinetic exchange-current densities at states of charge between 3 and 4.7 V *vs.* Li/Li^+. They noted that the changes in these parameters were qualitatively supported by changes in electrode structure observed by *in situ* x-ray diffraction measurements. To obtain improved

experimental data fits, they introduced a tri-modal particle size distribution. Zavalis *et al.* developed an impedance model that incorporated a porous electrode model that considered current collector resistance and capacitance affects (117). They optimized the simulated impedance response to fit experimental spectra from a three-electrode cell for a $LiFePO_4$|mesocarbon microbead (MCMB) graphite system. Scanning electron microscopy (SEM) images of cycled electrodes suggested significant structural changes in the $LiFePO_4$ electrode causing a reduction in electrode porosity. The changes observed in experimentally obtained impedance responses for the cell supported this hypothesis. Li *et al.* developed an impedance response model with a constant-phase element to capture time constant dispersion in the impedance response (118). In their model, the thermodynamic expressions governing open-circuit potential behavior were changed to the Nernst equation for both electrodes. They used the model to obtain fitted parameters, like film resistance, over the course of cell cycling.

In this work, we develop a physics-based impedance model that is compared to experimental impedance data obtained for a commercial graphite|LiNMC full cell. The role of film formation on the cathode is investigated as a possible high-frequency feature in an experimental impedance response.

Model Formulation

General Model Equations

Figure 5.1 is an illustration of graphite|separator|$LiNi_{0.33}Mn_{0.33}Co_{0.34}O_2$ cell. The porous electrodes consist of secondary active insertion material particles, binder, and

additives to improve electronic conductivity. An electronically inert separator is sandwiched between the two porous electrodes. The secondary particles are composed of smaller primary particles in each electrode. These particles are assumed spherical and are sometimes enveloped in a surface film. Current collects close the ends of the cell, and the total length of the cell is defined as L_{cell}. Along the length of the cell, $x = 0$ is defined as the position in the porous electrode corresponding to the anode current collector and $x = L_{cell}$ as that corresponding to the cathode current collector.

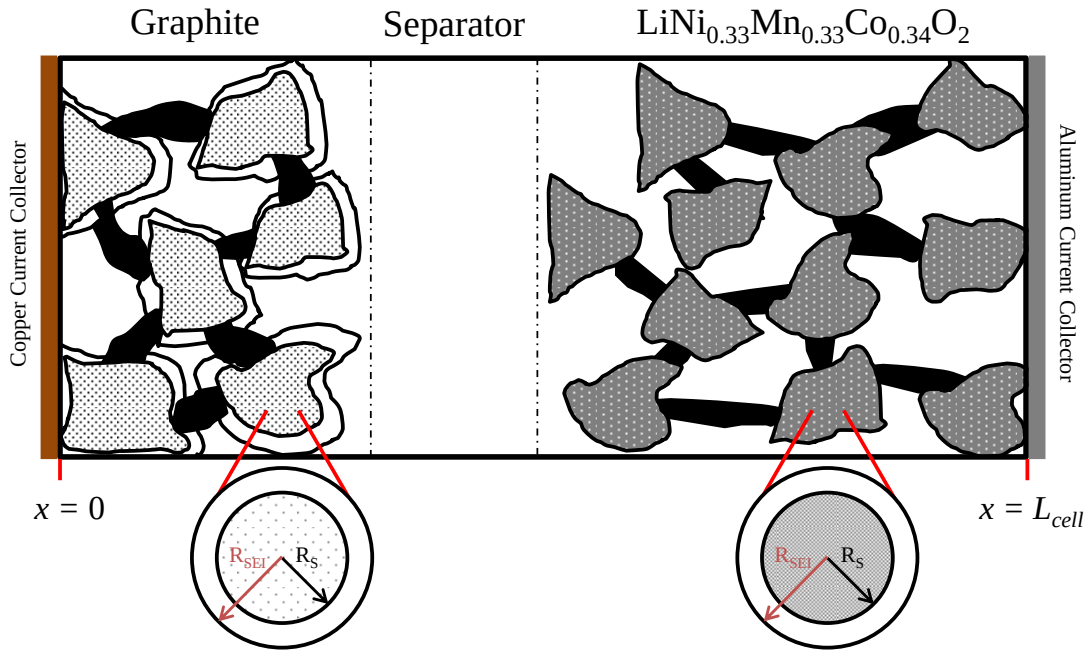

Figure 5.1. Illustration of the dual-lithium ion insertion cell with two porous insertion electrodes with separator and current collectors. Secondary particles are shown in the main illustration. A detailed primary particle is shown in an expanded version of the illustration. The graphite electrode particles are enveloped by a surface film.

In Figure 5.2, a detailed illustration is given of charge placement in a secondary particle, film, and electrolyte. An equivalent circuit representation of the current paths is also provided. ϕ_1 and ϕ_2 are the potentials of the solid particle and solution phase adjacent to the surface film, respectively. In this model formulation, we assume the existence of two capacitors and two resistors. The capacitor at the solid-film interface is the double-layer capacitance (C_{dl}). The outer capacitor is the film capacitor (C_f) and short circuits the film. Additionally, the film capacitor is the smaller of the two capacitors. As the electrode potential is perturbed from open circuit, the outer capacitor is the first to charge. After sufficient charge builds on the outer capacitor, charge begins to trickle across the film (R_f). The charge then reaches the solid-film interface, charging the double-layer capacitor. After sufficient charging of the double layer, the charged species intercalate into the solid particle (R_{ct}). Those charged species then diffuse towards the center of the particle (R_{part}-Z_{conc})

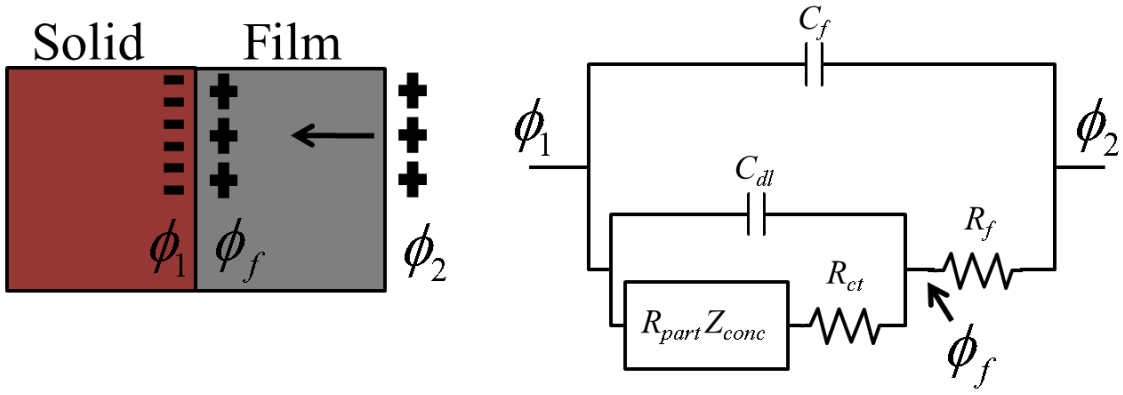

Figure 5.2. Detailed charge placement illustration, with corresponding current paths for the development of the single particle model. See text for discussion.

Using Figure 5.2 as a reference, we begin by describing the transport equations that govern lithium transport across the particle. There are two primary branches for current density leaving the solution-phase to pass across the film. The total current density, i_{tot}, along the two primary branches is given as

$$i_{tot} = i_{f,R} + i_{f,C}, \tag{5.1}$$

where $i_{f,C}$ is the capacitive film current density, and $i_{f,R}$ is the resistive through-plane film current density. The resistive film current density is given as

$$i_{f,R} = \frac{k_f}{L_f}(\phi_f - \phi_2) = \frac{1}{R_f}(\phi_f - \phi_2), \tag{5.2}$$

where k_f is the film conductivity, L_f is the film thickness, ϕ_f is the potential at the electrode- film interface, ϕ_2 is the potential at the film-electrolyte interface. The current density that passes through the film capacitor is given as

$$i_{f,C} = C_f \frac{d(\phi_1 - \phi_2)}{dt}. \tag{5.3}$$

The current density that passes through the resistor of the film enters into the solid particle. At the solid-film interface, there are two parallel paths for current density to pass. The current density that crosses the two parallel paths is given as

$$i_{f,R} = i_{dl} + i_{\text{int}}, \tag{5.4}$$

where i_{dl} is the current density due to charging the double layer, and i_{int} is the intercalation current density. The current associated with double-layer charging is given as

$$i_{dl} = C_{dl} \frac{d(\phi_1 - \phi_f)}{dt}. \tag{5.5}$$

Lithium intercalates into the electrode. The intercalation requires the presence of active sites, θ, and electrons, e^-. Expressed in terms of lithium ions,

$$\text{Li}^+ + e^- + \theta \Leftrightarrow \text{Li-}\theta\ . \tag{5.6}$$

The intercalation kinetics are governed by the Butler-Volmer expression,

$$i_{\text{int}} = i_0 \left\{ \exp\left(\frac{\alpha_a F \eta}{RT} \right) - \exp\left(\frac{-\alpha_c F \eta}{RT} \right) \right\}, \tag{5.7}$$

where $i_0 = kFc^{\alpha_a}(c_{\max} - c_s)^{\alpha_a} c_s^{\alpha_c}$ and is the assumed form of the rate constant. In the expression, k is the net reaction rate constant, α_a and α_c are charge-transfer coefficients, F is Faraday's constant, R is 8.314 J-mol^{-1}-K^{-1}, T is the temperature at the particle-SEI interface, c_s is the solid concentration in the particle, and c_{max} is the maximum concentration in the particle. The overpotential, η, represents the driving force away from equilibrium that is applied to the solid and is defined as

$$\eta = \phi_1 - \phi_2 - U\ , \tag{5.8}$$

where U is the equilibrium potential. Conservation of charge for each porous electrode is given as

$$a\frac{i_{tot}}{F} = -\frac{s_i}{n}\frac{di_2}{dx}. \tag{5.9}$$

where i_2 is the current in the electrolyte phase, a is the specific interfacial surface area, s_i is the stoichiometric coefficient of the charge-transfer reaction, and n represents the number of electrons transferred. The specific interfacial area for spherical particles is

$$a = 3\frac{(1-\varepsilon_2)}{R_s}, \tag{5.10}$$

where ε_2 is the ratio of pore volume to total electrode volume, and R_s is the solid particle radius. A material balance on lithium salt in the electrolyte phase is given as

$$\frac{\partial(\varepsilon_2 c)}{\partial t} = \nabla\cdot(D_{eff}\nabla c) - \frac{i_2\cdot\nabla t_+^0}{F} + \frac{a i_{tot}(1-t_+^0)}{F}. \tag{5.11}$$

where c is the in-pore concentration of the electrolyte, D_{eff} is the effective diffusivity of the electrolyte phase, and t_+^0 is the transference number. Solid phase transport is treated as lithium diffusion in spherical particles. The governing equation is given as

$$\frac{\partial c_s}{\partial t} = \frac{1}{r^2}\frac{\partial}{\partial r}\left(r^2\left(D_{eff,s}\frac{\partial c_s}{\partial r}\right)\right). \tag{5.12}$$

where $D_{eff,s} = D_s \left(\frac{c_s}{c_{max}} \right)^{\gamma}$, r is the radial coordinate, D_s is the diffusivity of lithium in the solid phase, and γ is a fitted parameter. At the center of the particle, no flux boundary conditions apply,

$$\frac{\partial c_s}{\partial r} = 0 \text{ at } r = 0 . \tag{5.13}$$

At the solid-film particle interface, the inward intercalation current density is related to the particle surface concentration as

$$\frac{i_{int}}{F} = -D_s \frac{\partial c_s}{\partial r} \text{ at } r = R_s . \tag{5.14}$$

The total superficial current density, I, is in the solution phase or through the solid phase of the composite electrode and is conserved. That is,

$$I = i_1 + i_2 . \tag{5.15}$$

where i_1 is the electronic current density, and i_2 is the solution-phase current density. Electronic current flows in the solid matrix and is given by Ohm's Law,

$$i_1 = -\sigma_{eff} \frac{d\phi_1}{dx} , \tag{5.16}$$

where σ_{eff} is the effective electronic conductivity in the solid phase. The solution-phase current density is given by a modified version of Ohm's Law,

$$i_2 = -\kappa_{eff}\frac{d\phi_2}{dx} + \frac{\kappa_{eff}RT}{F}\left(1 + \frac{\partial \ln f_A}{\partial \ln c}\right)(1 - t_+^0)\frac{d \ln c}{dx}. \quad (5.17)$$

κ_{eff} is the effective conductivity of the electrolyte phase. To our knowledge, data are not readily available in the literature on the salt activity coefficient, f_a. Therefore, f_a is assumed to be 1. At the ends of the cell, there is no flux of lithium in the electrolyte phase,

$$\frac{dc}{dx} = 0. \quad (5.18)$$

Additionally, current flows in only the solid at the ends of the cell.

$$\frac{d\phi_2}{dx} = 0. \quad (5.19)$$

The effective transport properties are used in the case of porous media. These modified transport properties are given as

$$D_{eff} = D\varepsilon_2^{1.5} \quad (5.20)$$

$$\sigma_{eff} = \sigma\varepsilon_1^{1.5} \quad (5.21)$$

$$\kappa_{eff} = \kappa\varepsilon_2^{1.5} \quad (5.22)$$

For the anode, the open-circuit potential function (74) is given as

$$U_{An} = -0.132 + 1.41\exp(-3.52x_{An}), \quad (5.23)$$

where

$$x_{An} = \frac{c_s(0)}{c_{s,\max}}. \tag{5.24}$$

For the cathode, the open-circuit potential function is measured for the cathode material and shown in Figure 5.3.

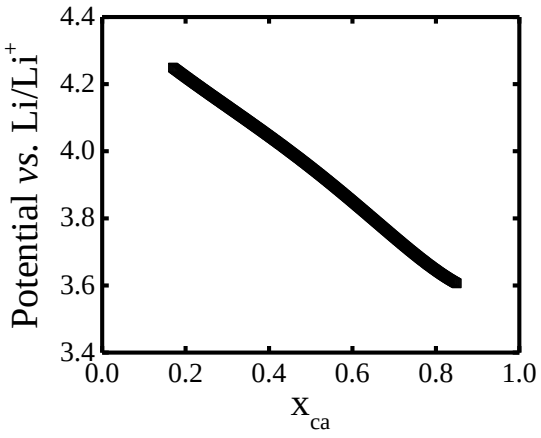

Figure 5.3. The open-circuit potential function of the cathode material.

The fitted open-circuit potential function, obtained from Figure 5.3, is given as

$$U_{Ca} = 2.529x^4 - 4.8092x^3 + 2.9923x^2 - 1.6323x + 4.463, \tag{5.25}$$

where

$$x_{Ca} = \frac{c_s(0)}{c_{s,\max}}. \tag{5.26}$$

Physical-Model Equations Transformed

In this section, the transformed physical-model equations are provided. We first discuss how the model equations are transformed from the time to frequency domain. Then, we define the impedance response in terms of cell potential and current. Next, we develop the single particle impedance model equations. Finally, the single particle model impedance response is expanded to a porous electrode impedance response.

Simulation of Impedance Model

To simulate EIS, the model equations are transformed from the time domain to the frequency domain using the technique employed by Meyers and Doyle *et al.* (87, 115). From the outset, the system is assumed to have a steady state at the open-circuit conditions. Then, the variables in the system are casted into the sum of steady-state variables, representing DC conditions, and perturbation variables. For example, for a given variable, X,

$$X = \bar{X} + \mathrm{Re}\left[\tilde{X}\exp(j\omega t)\right] \tag{5.27}$$

where variables with overbars are at steady-state, variables with tildes are complex variables, j is the imaginary unit, and ω is the angular frequency. The variable is used to evaluate a function, f,

$$f(X) = f(\bar{X} + \mathrm{Re}[\tilde{X}\exp(j\omega t)]). \tag{5.28}$$

In EIS, perturbations to the system are small so that the system response is linear. After neglecting higher order terms, we find that

$$f(X) = f(\bar{X}) + \left.\frac{df}{dX}\right|_{SS} (\mathrm{Re}[\tilde{X}\exp(j\omega t)]), \tag{5.29}$$

where the first derivative of the function is evaluated around the steady state condition. After evaluation of Equation (5.29), the variable is then cast into a real and an imaginary component. Overall, the procedure leads to steady-state, real, and imaginary sets of equations.

Impedance Definitions

The cell potential and current density include a steady-state and oscillating contribution that depends on the angular frequency, ω, as

$$\eta = \bar{\eta} + \mathrm{Re}\left\{\eta \exp(j\omega t)\right\} \tag{5.30}$$

and

$$i = \bar{i} + \mathrm{Re}\left\{\tilde{i}\exp(j\omega t)\right\}, \tag{5.31}$$

where terms with overbars denote a steady-state component, and the complex variable is an oscillating component expressed as a phasor with magnitude and phase angle. The impedance response is given as the ratio of voltage-to-current phasors and can be separated into real and imaginary components as

$$Z(\omega) = \frac{\tilde{\eta}}{\tilde{i}} = Z_{re} + jZ_{im}. \tag{5.32}$$

Single-Particle Model Development

Using Figure 5.2 as a reference, the total current density across the film is given as

$$i_{tot} = i_{f,R} + i_{f,C} . \tag{5.33}$$

The current density associated with charging the film capacitor is given as

$$\tilde{i}_{f,C} = j\omega C_f \left(\tilde{\phi}_1 - \tilde{\phi}_2\right) . \tag{5.34}$$

The current density that through the resistive portion of the film is given as

$$\tilde{i}_{f,R} = \frac{\kappa_f}{L_f}\left(\tilde{\phi}_f - \tilde{\phi}_2\right) = \frac{\left(\tilde{\phi}_f - \tilde{\phi}_2\right)}{R_f} . \tag{5.35}$$

The current density across the solid-film interface is given as

$$\tilde{i}_{f,R} = \tilde{i}_{dl} + \tilde{i}_{\text{int}} . \tag{5.36}$$

The current charging the double layer is

$$\tilde{i}_{dl} = j\omega C_{dl}\left(\tilde{\phi}_1 - \tilde{\phi}_f\right) . \tag{5.37}$$

Linearization of the intercalation current density around open circuit gives

$$\tilde{i}_{\text{int}} = \left.\frac{d\,\bar{i}_{\text{int}}}{d\,\bar{\eta}}\right|_{\bar{\eta}=0} \tilde{\eta} \tag{5.38}$$

where

$$\tilde{\eta} = \tilde{\phi}_1 - \tilde{\phi}_2 - \left.\frac{d\overline{U}}{d\overline{c}_s}\right|_{\overline{c}_s = c_{sf}} \tilde{c}_{sf} \,. \tag{5.39}$$

We can define the lithium concentration at the particle surface as

$$\tilde{c}_{sf} \equiv \tilde{c}_s \Big|_{r=R_s} \tag{5.40}$$

where the subscript *sf* represents the surface concentration. The solid surface concentration can be obtained from Equation (5.12), which describes solid phase transport.

The open-circuit potential function has a non-linear dependence on particle surface concentration. The general form for the intercalation current density that applies for both electrodes is given as

$$\tilde{i}_{int} = \frac{(\alpha_a + \alpha_c) i_0 F}{RT} \left(\tilde{\phi}_1 - \tilde{\phi}_f - \left.\frac{d\overline{U}}{d\overline{c}_s}\right|_{\overline{c}_s = c_{sf}} \tilde{c}_{sf}\right). \tag{5.41}$$

The potential at open circuit is dependent on the surface concentration of lithium in the particle.

Consequently, the flux of lithium at the particle-film surface is given as

$$\frac{\tilde{i}_{int}}{F} = -\overline{D}_{s,eff} \left.\frac{d\tilde{c}_s}{dr}\right|_{r=R_s} \,. \tag{5.42}$$

The solid phase diffusivity is assumed to have concentration dependence. Rewriting Equation (5.12) in terms of steady-state and perturbation variables gives

$$\frac{\partial\left(\bar{c}_s + \tilde{c}_s \,\mathrm{Re}\left(\exp(j\omega t)\right)\right)}{\partial t} = \frac{1}{r^2}\frac{\partial}{\partial r}\left(r^2\left(\left(\bar{D}_{s,eff} + \tilde{D}_{s,eff}\,\mathrm{Re}\left(\exp(j\omega t)\right)\right)\frac{\partial \bar{c}_s + \tilde{c}_s \,\mathrm{Re}\left(\exp(j\omega t)\right)}{\partial r}\right)\right) \tag{5.43}$$

The system is at steady-state, and second order effects are not considered due to the a priori assumption of linearity. Therefore, expansion of Equation (5.43) leads to

$$j\omega\tilde{c}_s = \frac{\bar{D}_{s,eff}}{r^2}\frac{\partial}{\partial r}\left(r^2\left(\frac{\partial \tilde{c}_s}{\partial r}\right)\right). \tag{5.44}$$

The diffusivity of lithium in the solid phase is then only a function of the steady-state solid surface concentration. The solution to Equation (5.44), combined with Equations (5.40) and (5.42), is

$$\frac{\tilde{c}_{sf}\bar{D}_{s,eff}F}{\tilde{i}_{int}R_s} = \frac{\tanh(\sqrt{j\Omega})}{\sqrt{j\Omega} - \tanh(\sqrt{j\Omega})}, \tag{5.45}$$

where $\Omega = \frac{\omega R_s^2}{\bar{D}_{s,eff}}$ (115). This transfer function provides the relationship between surface concentration of lithium and flux into the particle. The following identities are used to express Equation (5.45) into real and imaginary components,

$$\sqrt{j\Omega} = \frac{\sqrt{2}}{2}(1+j) \tag{5.46}$$

and

$$\tanh(x + jy) = \frac{\sinh(2x) + j\sin(2y)}{\cosh(2x) + \cos(2y)}. \tag{5.47}$$

We can define Equation (5.45) as a dimensionless concentration impedance,

$$Z_{conc} = \frac{\tilde{c}_{sf}\bar{D}_{s,eff}F}{\tilde{i}_{int}R_s}. \tag{5.48}$$

Combining Equation (5.48) with Equation (5.41) gives

$$\tilde{i}_{int} = \frac{(\alpha_a + \alpha_c)i_0F}{RT}(\tilde{\phi}_1 - \tilde{\phi}_f - \left.\frac{d\bar{U}}{d\bar{c}_s}\right|_{\bar{c}_s = c_{sf}} \frac{Z_{conc}R_s}{\bar{D}_{s,eff}F}\tilde{i}_{int}) \tag{5.49}$$

We define two parameters

$$\begin{aligned} R_{ct} &= \frac{RT}{(\alpha_a + \alpha_c)i_0F} \\ R_{part} &= \left.\frac{d\bar{U}}{d\bar{c}_s}\right|_{\bar{c}_s = c_{sf}} \frac{R_s}{\bar{D}_{s,eff}F} \end{aligned} \tag{5.50}$$

that describe the charge-transfer resistance and the diffusional resistance in the particle. Rewriting Equation (5.50) with the two parameters gives

$$\tilde{i}_{int} = \frac{1}{\left(R_{ct} + R_{part}Z_{conc}\right)}\left(\tilde{\phi}_1 - \tilde{\phi}_f\right). \tag{5.51}$$

Rewriting Equation (5.36) using Equation (5.51) leads to

$$\tilde{i}_{f,\mathrm{R}} = \left(j\omega C_{dl} + \frac{1}{\left(R_{ct} + R_{part} Z_{conc} \right)} \right) \left(\tilde{\phi}_1 - \tilde{\phi}_f \right). \tag{5.52}$$

Rewriting Equation (5.52) in terms of the impedance,

$$Z_{solid} = \frac{1}{\left(j\omega C_{dl} + \frac{1}{\left(R_{ct} + R_{part} Z_{conc} \right)} \right)} \tag{5.53}$$

where Z_{solid} describes the particle impedance without surface film. We note that Z_{solid} is a complex number because of the concentration impedance, Z_{conc}. Equation (5.52) can be combined with Equations (5.33), (5.34), and (5.35), to give the total current density

$$\tilde{i}_{tot} = \left\{ \left[\frac{1}{Z_{solid} + R_f} \right] + j\omega C_f \right\} \left(\tilde{\phi}_1 - \tilde{\phi}_2 \right). \tag{5.54}$$

Rewriting for the total particle impedance, Z_{tot},

$$Z_{tot} = \frac{1}{\frac{1}{Z_{solid} + R_f} + j\omega C_f}. \tag{5.55}$$

Expansion to a Porous Electrode

The single particle model equations are coupled to the porous electrode model through the total particle current density, $\tilde{i}_{tot}$. The material balance in the electrolyte is given as

$$\frac{\partial(\varepsilon_2 \tilde{c}\exp(j\omega t))}{\partial t} = \nabla\cdot(D_{eff}\nabla\tilde{c}\exp(j\omega t)) - \frac{\tilde{i}_2\exp(j\omega t)\cdot\nabla t_+^0}{F} + \frac{a\tilde{i}_{tot}\exp(j\omega t)(1-t_+^0)}{F} \tag{5.56}$$

The flux of lithium in the electrolyte phase is given as

$$\tilde{N} = -D_{eff}\nabla\tilde{c} + \frac{\tilde{i}_2 t_+^0}{F} \tag{5.57}$$

The charge balance on the electrolyte is given as

$$a\tilde{i}_{tot} = -\frac{s_i}{nF}\frac{d\tilde{i}_2}{dx}, \tag{5.58}$$

The total current density from anode to cathode current collectors is

$$\tilde{I} = \tilde{i}_1 + \tilde{i}_2 \tag{5.59}$$

The electronic current density in the solid is given as

$$\tilde{i}_1 = -\sigma_{eff}\frac{d\tilde{\phi}_1}{dx}. \tag{5.60}$$

The solution phase current density is given as

$$\tilde{i}_2 = -\kappa_{eff}\frac{d\tilde{\phi}_2}{dx} + \frac{\kappa_{eff}RT}{F}\left(1+\frac{\partial\ln f_A}{\partial\ln\tilde{c}}\right)(1-t_+^0)\frac{d\ln\tilde{c}}{dx}, \tag{5.61}$$

There is no flux of salt through the ends of the cell

$$\tilde{N} = 0 . \tag{5.62}$$

At the ends of the cell, the current density flows through the solid matrix

$$\tilde{I} = \tilde{i}_1 . \tag{5.63}$$

As a reference, the potential in the electrolyte at the cathode current collector is set to zero,

$$\tilde{\phi}_2 = 0 . \tag{5.64}$$

The total cell impedance, $z_{tot,cell}$, is given as

$$Z_{tot,cell} = \frac{\tilde{\phi}_1\Big|_{x=0} - \tilde{\phi}_1\Big|_{x=L_{cell}}}{\tilde{I}\Big|_{x=0}} . \tag{5.65}$$

Open-Circuit Potential Functions

For the anode, the open-circuit potential function is given as

$$\bar{U}_{An} = -0.132 + 1.41\exp(-3.52\bar{x}_{An}) , \tag{5.66}$$

where

$$\bar{x}_{An} = \frac{\bar{c}_{sf}(0)}{c_{s,\max}} . \tag{5.67}$$

For the anode, evaluating the derivative of the open-circuit potential function gives,

$$\left.\frac{d\overline{U}_{An}}{d\overline{c}_{s,An}}\right|_{\overline{c}_s=\overline{c}_{sf}} = 1.41\left(\frac{-3.52}{c_{s,\max}}\exp(-3.52\frac{\overline{c}_{sf}}{c_{s,\max}})\right). \quad (5.68)$$

For the cathode, the open-circuit potential function is given as

$$\overline{U}_{Ca} = 2.529\overline{x}_{Ca}^4 - 4.8092\overline{x}_{Ca}^3 + 2.9923\overline{x}_{Ca}^2 - 1.6323\overline{x} + 4.463, \quad (5.69)$$

where

$$\overline{x}_{Ca} = \frac{\overline{c}_{sf}(0)}{c_{s,\max}}. \quad (5.70)$$

For the cathode, evaluating the derivative of the open-circuit potential function gives

$$\left.\frac{d\overline{U}}{d\overline{c}_s}\right|_{\overline{c}_s=\overline{c}_{sf}} = (-\frac{1.6323}{c_{\max}} + \frac{5.9846}{c_{\max}^2}\overline{c}_{sf} - \frac{14.4276}{c_{\max}^3}\overline{c}_{sf}^2 + \frac{10.1192}{c_{\max}^4}\overline{c}_{sf}^3). \quad (5.71)$$

COMSOL Multiphysics software (version 4.3a) is used to solve the relevant system of equations to obtain the single-particle and full-cell impedances. Equations (5.45), (5.48), and (5.55) are solved to obtain the single-particle impedance. Equations (5.56) through (5.65) are solved, along with Equation (5.54), to obtain the full-cell impedance.

Experimental Procedure

Fresh graphite|LiNMC cells were calendar aged for 3200 hours at 75°C and 50 % state of charge (SOC). The impedance response of the fresh cells was measured prior to aging. After aging, calendar-aged cells were measured over a frequency range of 1 MHz to 10 mHz with a perturbation voltage of 5 mV_{RMS}. Following EIS, transmission electron

microscopy images of the LiNMC cathode samples were obtained by a Tecnai G2 F30 (FEI, Netherlands) operated at an accelerating voltage of 300 kV. For sample preparation, electrodes were submerged in dimethyl carbonate (DMC) under Argon gas and sonicated to separate NMC particles from the current collector surface. NMC powders, solvated by DMC, were then drop casted on a TEM grid. The samples were exposed to air for a short period of time for transfer to the sample chamber.

Experimental Results

Cathode Particle TEM Results

In Figure 5.4, TEM images are given of a cathode particle for fresh and aged electrodes. Figure 5.4(a) and Figure 5.4(b) are fresh and aged samples, respectively. Figure 5.4(c) and Figure 5.4(d) are magnifications of Figure 5.4(a) and Figure 5.4(b), respectively. The images show LiNMC particles in the presence of electrolyte. We infer from the images that calendar aging causes the formation of a surface layer on the cathode particles. The thickness of this layer on the cathode particles is approximately 5 nm.

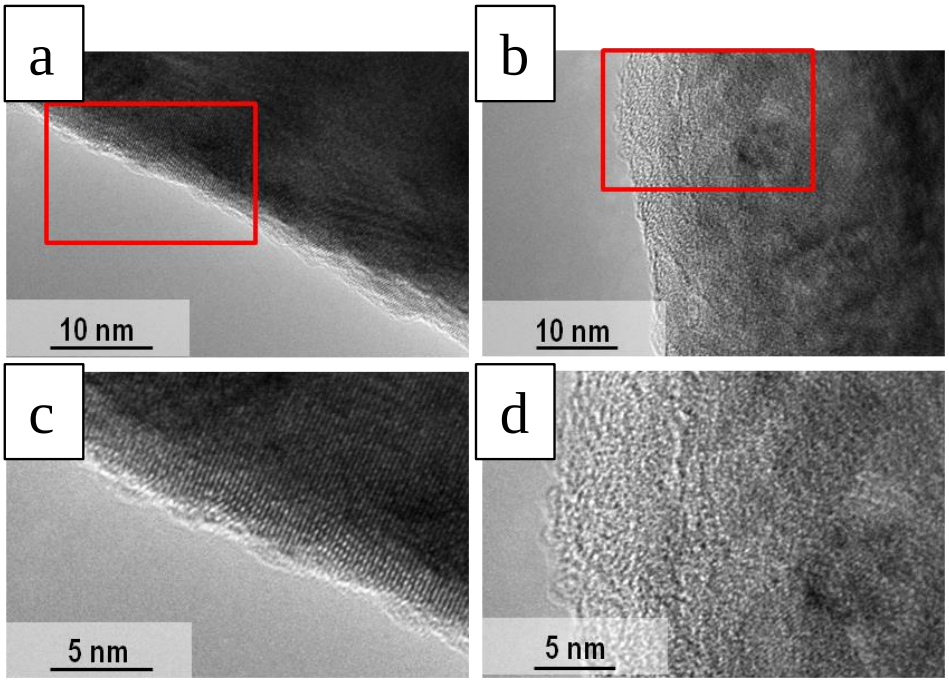

Figure 5.4. TEM images of fresh (a) and aged (b) cells taken of the cathode. (c) and (d) are magnifications of (a) and (b), respectively. A surface layer is found on the cathode particles following aging. Images obtained from the unpublished work of Jung Tae Lee et al.

Full Cell Impedance Response Measurements

Nyquist- and Bode-plot formats are parametric plots of the frequency response of a system. The Nyquist-plot format is a complex plane format that includes the imaginary and real components of the impedance response. The imaginary and real components of the response are uniquely measured at each frequency over a frequency range. These components are then collected at each frequency and combined to provide information on the frequency response of the system. This format is the most common format of representation in the lithium-ion battery literature. However, in this format, information about the frequency is lost, unless otherwise explicitly labelled on the Nyquist plot.

The second format is referred to as a Bode-plot format. This representation of the frequency response is a collection of the real and imaginary responses, defined as a magnitude of the impedance response at each frequency. In Blot-plot format, the magnitude of the impedance is defined as

$$Z_{mag} = \sqrt{Z_{Re}^2 + Z_{Im}^2}, \tag{5.72}$$

where Z_{Re} and Z_{Im} are the magnitudes of the real and imaginary components of the impedance at a single frequency. These versions of the response are advantageous because information about the frequency is explicitly provided. However, Bode-plot representation is less commonly represented in lithium-ion battery literature. Here, we utilize both Nyquist- and Bode-plot formats to investigate the processes that compose the impedance response.

In Figure 5.5, experimental impedance responses of representative fresh and calendar-aged graphite|LiNMC cells are given in Nyquist-plot (Figure 5.5(a) and Figure 5.5(b)) and Bode-plot (Figure 5.5(c)) formats. Figure 2(b) is an expansion of the real and imaginary axes of Figure 5.5(a). The fresh cell and calendar-aged responses in each subfigure are represented by black squares and red circles, respectively.

The fresh cell response includes two arcs, slightly separated in frequency space, over the high- and mid-frequency ranges. The arcs are frequently referred to as kinetic arcs because they are the result of intercalation reactions at the solid-film interface (96). The two kinetic arcs correspond to interfacial processes occurring at the solid-particle surfaces of the porous electrodes.

At approximately 3 Hz, there is a distinct separation of mid- and low-frequency responses, causing an elbow in the data. Following the elbow, there is a cluster of points, which extend into the shape of a curved line. The curved line response is a result of lithium transport in the solid-phase particles of the two porous electrodes. The Bode-plot representation provides analogous information about the impedance response but with respect to the frequency.

There are unique features in the response that illustrate the effects of calendar aging in the Nyquist-plot formats. The two primary features are a shift in the high-frequency intercept and the presence of an additional arc. The high frequency intercept is defined as the value of the real-axis intercept of the impedance at high frequencies. In Figure 5.5(b), the high-frequency intercept shift is evident, with the real axis intercept increasing from 3.6 Ω-cm^2 to 4.2 Ω-cm^2 following calendar aging. We assume that the shift is attributed to the presence of a surface layer after calendar aging on the negative electrode.

The second feature is the appearance of a third arc in the impedance spectrum. From the outset, we assume that, in the fresh cell impedance measurement, the first kinetic arc is the anode response (20 kHz), and the second kinetic arc is the cathode response (400 Hz). The kinetic arcs are arbitrarily assigned because we do not have the individual impedance responses of each electrode. In the calendar-aged impedance measurement, the first arc is designated the film response (65 kHz), the second kinetic arc the anode response (300 Hz), and the third arc is the cathode response (5 Hz). The purpose of this work is to investigate the high frequency response of the impedance spectrum after aging to determine if the cathode particle in Figure 5.4 is observable on

the impedance spectrum. In the next section, we explore the magnitude of the parameters of the film needed to cause the appearance of a new arc at high frequencies in the impedance spectrum.

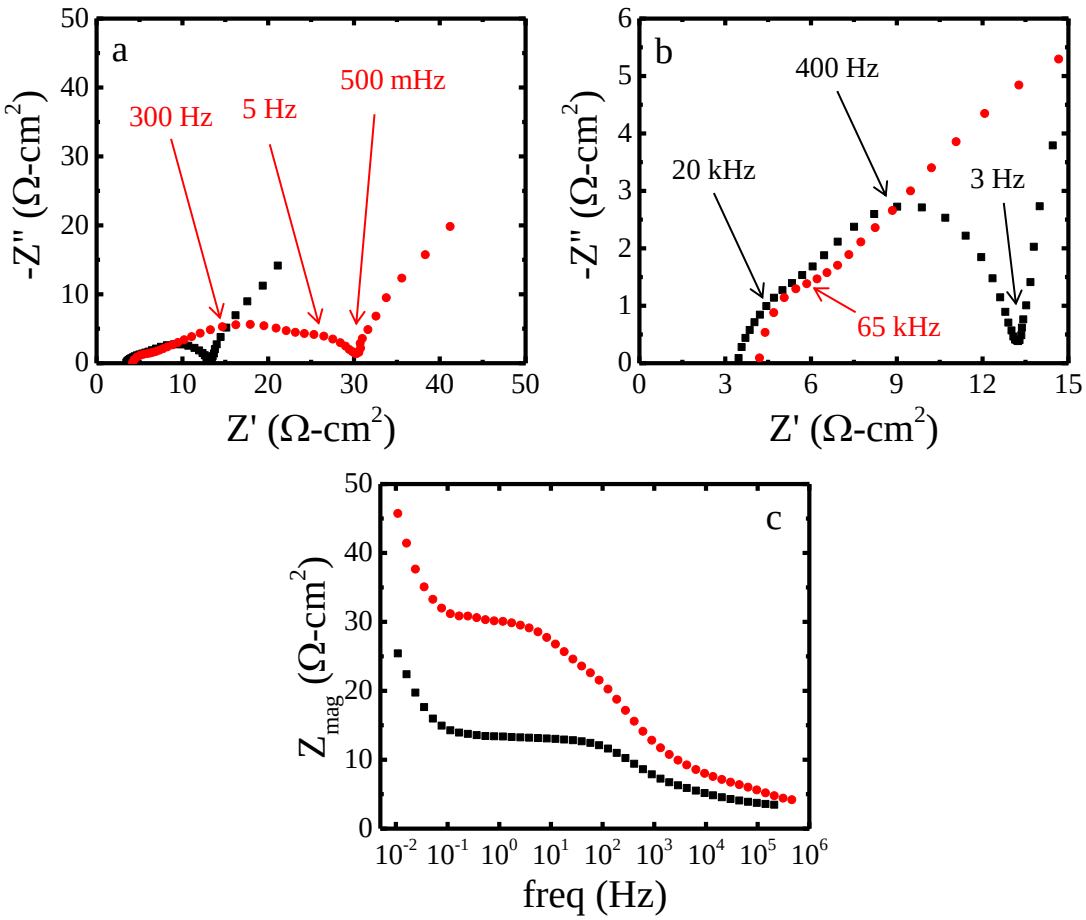

Figure 5.5. Experimental impedance responses for both fresh and calendar-aged full cells. (a) Nyquist-plot format of the entire spectrum for each cell, (b) the real and imaginary axes of (a) are been expanded, and (c) Bode-plot format of the entire spectrum for each cell. Fresh (squares) and calendar aged (circles) indicate that degradation leads to a separate process that causes the formation of a distinct semicircle in Nyquist-plot format at high frequencies. Spectra were obtained from the unpublished work of Tapesh Joshi *et al*.

Model Results

The model is used to simulate the impedance response of the full cell and analyze experimental spectra obtained for the, both fresh and aged. In Table 1, cell parameters are provided for the fresh and calendar-aged simulations. These parameters are constant between the simulations. The reported parameters are measured, obtained from the literature, or assumed due to inconsistencies in the literature. In Table 2, the values of fitted parameters from the experimental spectra are provided for both fresh and aged cells.

Table 1. List of parameters used for the solid matrix, electrolyte, separator, and SEI physical properties that are assumed constant in each simulation.

Symbol	Units	Anode (graphite)	Separator	Cathode (NCM)
R_s	m	3.5×10^{-6} [a]	-	1.1×10^{-6} [m]
c_{max}	mol/m^3	30474[e]	-	48794[e]
L	m	65×10^{-6} [m]	25×10^{-6} [a]	75×10^{-6} [m]
α_a	-	0.5[a]	-	0.5[a]
α_c	-	0.5[a]	-	0.5[a]
D	m^2/s	7.0×10^{-10} (119)	7.0×10^{-10} (119)	7.0×10^{-10} (119)
c_2^0	mol/m^3	1200[m]	1200[m]	1200[m]
D_s	m^2/s	5×10^{-15} (120)	-	2.2×10^{-15} (121)
ε_1	-	0.49 (119)	-	0.59 (119)

ε_2	-	0.485 [119]	0.59 [119]	0.385 [119]
T	K	298	298	298
κ	S/m	0.89 [122]	0.89 [122]	0.89 [122]
σ	S/m	100 [123]	--	100 [123]
γ	-	1[a]	-	1[a]

[a]Assumed, [e]Estimated, [m]Measured,

[s]http://www.celgard.com/pdf/library/Celgard_Product_Comparison_10002.pdf

Table 2. A parameter comparison of fresh and aged cells.

		Fresh		Aged	
Symbol	Units	Anode (graphite)	Cathode (LiNMC)	Anode (graphite)	Cathode (LiNMC)
i_0	A/m^2	9	0.45	4.5	0.4
C_{dl}	F/m^2	0.01	0.01	0.18	0.12
D_{eff}	m^2/s	3.17 x 10^{-10}	1.67 x 10^{-10}	1.01 x 10^{-11}	1.67 x 10^{-10}
κ_{eff}	S/m	0.40	0.21	0.013	0.21
C_f	F/m^2	0	0	0	21 x 10^{-9}
L_f	m	0	0	10 x 10^{-9} [a]	5 x 10^{-9} [m]
κ_f	S/m	0	0	7.5 x 10^{-4}	3.8 x 10^{-7}

[a]Assumed, [m]Measured

In Figure 5.6, Nyquist- and Bode-plot formats are provided of experimental impedance responses for the fresh full cell, with simulated responses overlaid on the experimental spectrum. The simulation adequately captures the experimental impedance

response from approximately 200 kHz to 10 Hz. At approximately 200 kHz, the separator is the primary contributor to the real value of the impedance. The high frequency resistance, R_{HFR}, is determined by the physical properties of the insulating porous separator and is given as

$$R_{HFR} = \frac{L_{sep}\tau}{\kappa_e \varepsilon_{sep}}. \tag{5.73}$$

For the separator material, the tortuosity is determined to be 4.63 for $R_{HFR} = 3.5\ \Omega - \mathrm{cm}^2$. At high frequencies, the corresponding Bode plot shows that the $R_{HFR} = 3.5\ \Omega - \mathrm{cm}^2$.

In addition to the separator response, both anode and cathode kinetic arcs appear over the frequency range of 200 kHz to 1 Hz. The contributions of each electrode are distinguished in both Nyquist- and Bode-plot formats by their unique characteristic frequencies. The characteristic frequency, f_c, is defined as

$$f_c = \frac{1}{2\pi R_{ct} C_{dl}} = \frac{nF i_0}{2\pi RTC_{dl}}. \tag{5.74}$$

The characteristic frequencies of cathode and anode kinetic arcs are approximately 5 kHz and 250 Hz, respectively. For the anode, $i_0 = 9\ \mathrm{A\text{-}m^{-2}}$ and $C_{dl} = 10\ \mathrm{mF\text{-}m^{-2}}$. For the cathode, $i_0 = 0.45\ \mathrm{A\text{-}m^{-2}}$ and $C_{dl} = 10\ \mathrm{mF\text{-}m^{-2}}$.

From 100 Hz until approximately 10 mHz, the simulated response takes on a similar slope as the experimental data but is limited in replicating the experimental

impedance response. In the Nyquist-plot format, clustered from 100 Hz to 1 Hz are points that approach the real axis. With decreasing frequency, the simulated response appears as an approximate 45° sloped line. The sloped line is in response to concentration gradients that accumulate in the cell. In this case, the sloped-line portion of the response primarily is attributable to diffusion in the solid phase. A secondary contribution to the impedance response at low frequencies are due to concentration gradients forming in the solution phase of the along the length of the cell. However, the concentration gradients only minimally contribute to the response over the frequency range due to the high effectivity diffusivity in the solution phase. In Bode-plot format, the cluster of points is the flattened portion of the response between 100 to 1 Hz. Then, the subsequent solid-phase diffusion arc begins at approximately 1 Hz and continues until the end of the response.

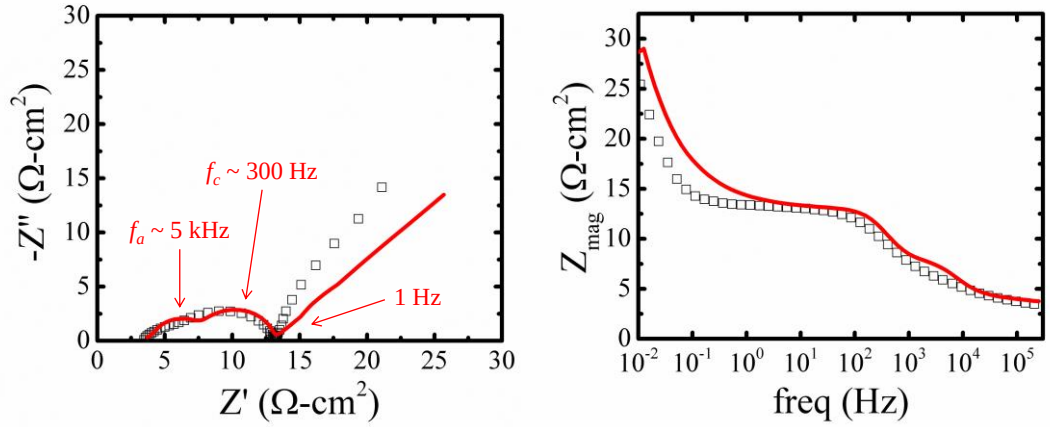

Figure 5.6. Nyquist- and Bode-plot formats of the impedance response at 50 % SOC for a full graphite|LiNMC cell during first cycle charging.

In Figure 5.7, Nyquist- and Bode-plot formats of the calendar-aged cell are given at 50 % SOC. In the calendar-aged response, there are several phenomena that are

important to address in the spectrum. First, as previously mentioned, calendar aging causes an increase in the high frequency resistance, approximately $0.6\ \Omega - cm^2$. We speculated that the increase was likely a result of surface film formation on the negative electrode particles. The phenomenon of surface film formation on anode particles, and its impact on the HFR, is well documented in the literature (79, 124).

In our analysis, we have assumed that the anode film thickness is 10 nm, which is within the order of magnitudes reported for several anode materials (30, 108, 125). For such film thickness, the conductivity of the film is at least three orders of magnitude less than the solution-phase conductivity. The conductivity is sensible, primarily because the film is solid and a product of electrolyte reduction. Additionally, the film must have a zero capacitance. If the film were capacitive, then the impedance spectrum would contain a new arc at high frequencies. That is, we would still observe a shift in the high frequency response, but the shift would arise because of an additional arc in the spectrum.

Second, the cathode particle film is visible in the high frequency portion of the impedance response. From the simulation, the cathode parameters are determined to be L_f = 5 nm, C_f = 21 nF-cm^{-2}, and k_f = 380 nS-m^{-1}. That is, for the film response to appear at high frequencies, the film capacitance must be several orders of magnitude less than the double-layer capacitance. This difference in capacitance allows for enough separation in the characteristic frequencies for both film and double-layer charging so that each is distinguishable in the spectrum. Assuming the structure of a parallel-plate capacitor, the relative permittivity of the film can be obtained from the capacitance and is given as

$$\varepsilon_r = \frac{L_f C_f}{\varepsilon_0}, \tag{5.75}$$

where ε_r is the relative permittivity of the film, and $\varepsilon_0 = 8.854 \times 10^{-12}$ F-m^{-2}. For the simulated values, $\varepsilon_r = 0.12$. The result is not sensible, as it is smaller than unity. For comparison, the relative permittivity of propylene carbonate and ethylene carbonate has been reported as $\varepsilon_r = 64$ and $\varepsilon_r = 89$, respectively (126). Increasing the value of the relative permittivity by an order of magnitude requires an equivalent increase in the film thickness or decrease in f_c for the cathode film to appear in the spectrum. However, the change in these parameters would have to be at least an order of magnitude. Therefore, there is no possibility that the cathode particle film is the source of the high frequency arc in the impedance spectrum in the present experimental impedance responses.

Third, we observe a significant change in the anodic kinetic arc. Simulation results indicate that the anode kinetic rate constant and solution phase effective properties all decrease after calendar aging. Intuitively, the kinetic rate constant can slow due to degradation of the electrode surface. We initially tested only a decrease in the kinetic rate constant between simulations. The resulting data fits were found to be poor and inconclusive in both Nyquist- and Bode-plot format.

Decreasing the both the kinetic rate constant and solution phase effective transport properties provided for a good fit of the experimental data. A change in the kinetic arc width is not limited to changes in the lithium-intercalation rate constant. There are two additional sources of impedance that can arise. First, the changes can be observed with a more pronounced porous electrode effect at high frequencies (96). The

length of porous electrode, distributed interfacial impedance, and effective conductivity of the solution phase all contribute to the magnitude of the porous electrode effect. Second, the changes in the kinetic arc width may be the result of more pronounced concentration gradients in the electrolyte. A decrease in the effective diffusivity in the solution phase could be a possible cause of the kinetic arc width increase in the solution phase.

A change in the intrinsic conductivity and diffusivity of the salt in the solution phase is unlikely to cause the sharp decline observed in the effective properties. The cell temperature remains relatively constant over the experiment. Rather, we suspect that calendar aging leads to changes in the porosity and tortuosity of the anode. The effective conductivity and diffusivity of the salt in the solution phase is dependent on the porosity to tortuosity ratio. A decrease in the porosity of the electrode would ultimately impact the magnitude of the porous electrode effect. The decrease in anode porosity is in qualitative agreement with recent investigations on electrode microstructural changes after SEI formation in graphite anodes (127). However, the model fittings indicate that the porosity to tortuosity ratio decreases by a factor of 10. Assuming that the Bruggeman relation defines the relationship between porosity and tortuosity,

$$\frac{\left(\varepsilon_2^{1.5}\right)_{\text{fresh}}}{\left(\varepsilon_2^{1.5}\right)_{\text{aged}}} = 10 \tag{5.76}$$

where the subscripts fresh and aged represent the fresh and calendar-aged cells. Evaluation of Equation (5.76) indicates that the porosity must decrease by a factor of 4.6 after aging. To our knowledge, such a decrease has not been observed in the literature.

Rather, we suspect that Bruggeman relation does not necessarily apply for these electrodes. The relation was initially developed for systems in which transport is obstructed by cylindrical or spherical particles (107). From the outset, model formulation assumes that the solid particles are indeed spherical in shape. However, SEI formation affects the pore structure and the shape of the obstructions that are encountered by the perturbation signal. Therefore, it is not necessary that the porosity change significantly during aging. More likely, tortuosity likely increases and offsets the decrease in porosity. Tortuosity increases could result from pores losing interconnection. Increased surface film formation likely fills pore spaces in the electrode. The resulting loss in pore volume would then create gaps in the connectivity of pores, drastically increasing the tortuosity in regions of the electrode.

Finally, aging of the cell leads to an extreme change in the double-layer capacitance of both electrodes. Although seemingly unlikely, the formation of a film on the solid particle surface may change the amount of adsorbed species at the solid-film interface. These adsorbed species would then contribute to the magnitude of the capacitance.

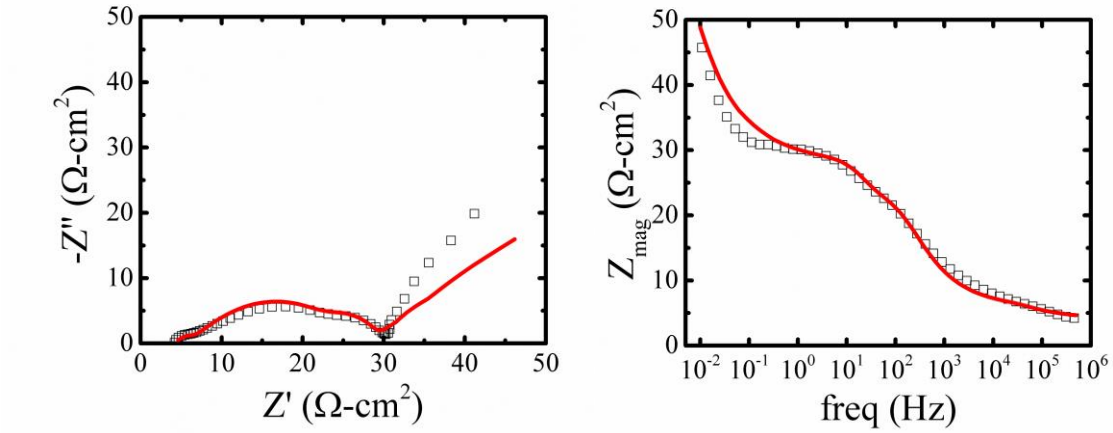

Figure 5.7. Nyquist- and Bode-plot formats of the impedance response at 50 % SOC for a full graphite|LiNMC cell after 3200 hours of calendar aging at 75° C.

The model has several strengths and deficiencies that should be addressed. The model adequately captures the general shape and slopes presented in the experimental impedance data for fresh and calendar-aged cells. The model allows distinguishing between the individual responses of the porous electrodes over the high- and mid-frequency ranges. Additionally, the model provides insight into film formation and the subsequent impact of films on the impedance response.

However, there are several improvements that can be made to the model formulation to address deficiencies in simulation and experimental data agreement over the high- and mid-frequency ranges. First, the model uses ideal capacitors. In most equivalent circuit fittings, ideal capacitors are frequently replaced with CPEs. The CPE is in itself an effective fitting parameter because the capacitance is treated as frequency dependent. It is not based on any measureable physics and, therefore, is only helpful in improving data fitting. A better understanding of additional interfacial capacitive processes, like surface adsorption on the solid particle and solvent-solid interaction, is needed to capture the underlying physical phenomena causing the frequency dependent capacitance that is observed in the spectra.

Second, the model fails to correctly capture the low-frequency solid-phase diffusion response. Current model formulation does not include the coupling of the faradaic response with the bulk concentration. Inclusion of the concentration on the faradaic response in Equation (5.7) gives

$$i_{\text{int}} = i_0 \left\{ \exp\left(\frac{\alpha_a F \eta}{RT} \right) - \frac{c}{c_0} \exp\left(\frac{-\alpha_c F \eta}{RT} \right) \right\}, \tag{5.77}$$

where c is the lithium-ion concentration in the solution phase and c_0 is the initial concentration in the solution phase. The inclusion of this term would cause the addition of concentration impedances in the anode and cathode. If their characteristic frequencies are in the appropriate frequency range, then these concentration impedances would capture part of the curvature observed in the low frequency Nyquist-plot formats that the model currently lacks. The concentration impedance is typically represented by a finite Warburg element in impedance spectra (128). Additionally, a particle size distribution (PSD) would aid in changing the slope of the low frequency response. The low frequency response starts as a 45° line off of the real axis. As lithium reaches the center of the particle, the 45° line begins to bend upwards into a capacitive line. The characteristic frequency for diffusion process, f_{diff}, is

$$f_{diff} = \frac{\bar{D}_s}{R_s^2} \tag{5.78}$$

The inclusion of a PSD would create multiple overlapping low frequency responses, each with their individual time constants. These overlapping responses would then cause part of the curvature observed in the low frequency response of the Nyquist plots.

Finally, we were unable to uniquely identify a physical process that would contribute to the third arc in the calendar-aged impedance spectrum. We suspect that concentration gradients are not fully incorporate into the model, which is leading to the discrepancy between experiment and simulation. In future work, we will incorporate the

coupling of solution phase concentration to the Butler-Volmer kinetic expression to understand the contribution of concentration gradients on the impedance response.

Conclusions

A mathematical model of the impedance response of a graphite|LiNMC is presented for the investigation of experimental impedance spectra before and after calendar aging. A new arc is observed in experimental impedance measurements after calendar aging. Transmission electron microscopy of cathode particles shows the formation of a surface film after calendar aging.

Simulation of the impedance response indicates that the surface film could be a potential cause of the new arc observed in the spectrum after calendar aging. However, it is unlikely that the new high frequency arc can be assigned to the film for two reasons. The film capacitance must be significantly smaller than the double-layer capacitance at each solid-film interface for the film response to be the highest frequency arc. In turn, the relative permittivity associated with the film would be at least an order of magnitude lower than expected. Additionally, the inclusion of a film at high frequencies would require that the double-layer capacitances increase by at least an order of magnitude, which is also unlikely.

There is a significant change in the anode response. The increase in anodic kinetic arc width is attributed to both a decrease in the rate constant and an order of magnitude decrease in the effective transport properties in the anode after calendar aging the cell. A significant reduction in the anode porosity is highly unlikely. Rather, we

suspect that invoking the Bruggeman relation to define the relationship between porosity and tortuosity is incorrect for this system.

The model does not adequately capture the low-frequency solid-phase diffusion responses in both electrodes. The model can be improved by inclusion of additional processes, such as a particle size distribution, which are measureable and can be expressed as model parameters.

References

1. J. M. Tarascon and M. Armand, *Nature*, **414**, 359 (2001).

2. J. B. Goodenough and K.-S. Park, *Journal of the American Chemical Society*, **135**, 1167 (2013).

3. J. S. Newman, *Electrochemical systems*, Hoboken, N.J. : J. Wiley, Hoboken, N.J. (2004).

4. E. Peled, *Journal of the Electrochemical Society*, **126**, 2047 (1979).

5. E. Peled, D. Golodnitsky and G. Ardel, *Journal of the Electrochemical Society*, **144**, L208 (1997).

6. M. Winter, The Solid Electrolyte Interphase – The Most Important and the Least Understood Solid Electrolyte in Rechargeable Li Batteries, in *Zeitschrift für Physikalische Chemie International journal of research in physical chemistry and chemical physics*, p. 1395 (2009).

7. P. Verma, P. Maire and P. Novák, *Electrochimica Acta*, **55**, 6332 (2010).

8. V. Etacheri, R. Marom, R. Elazari, G. Salitra and D. Aurbach, *Energy & Environmental Science*, **4**, 3243 (2011).

9. N. Nitta, F. Wu, J. T. Lee and G. Yushin, *Materials Today*, **18**, 252 (2015).

10. M. M. Thackeray, W. I. F. David, P. G. Bruce and J. B. Goodenough, *Materials Research Bulletin*, **18**, 461 (1983).

11. B. Wang, J. B. Bates, F. X. Hart, B. C. Sales, R. A. Zuhr and J. D. Robertson, *Journal of the Electrochemical Society*, **143**, 3203 (1996).

12. A. K. Padhi, K. S. Nanjundaswamy and J. B. Goodenough, *Journal of the Electrochemical Society*, **144**, 1188 (1997).

13. A. Sobkowiak, M. R. Roberts, R. Younesi, T. Ericsson, L. Häggström, C. W. Tai, A. M. Andersson, K. Edström, T. Gustafsson and F. Björefors, *Chemistry of Materials*, **25**, 3020 (2013).

14. B. L. Ellis, K. T. Lee and L. F. Nazar, *Chemistry of Materials*, **22**, 691 (2010).

15. R. Spotnitz, *Journal of Power Sources*, **113**, 72 (2003).

16. M. Ecker, J. B. Gerschler, J. Vogel, S. Käbitz, F. Hust, P. Dechent and D. U. Sauer, *Journal of Power Sources*, **215**, 248 (2012).

17. J. Vetter, P. Novák, M. R. Wagner, C. Veit, K. C. Möller, J. O. Besenhard, M. Winter, M. Wohlfahrt-Mehrens, C. Vogler and A. Hammouche, *Journal of Power Sources*, **147**, 269 (2005).

18. P. Arora, R. E. White and M. Doyle, *Journal of the Electrochemical Society*, **145**, 3647 (1998).

19. R. Fong, U. von Sacken and J. R. Dahn, *Journal of the Electrochemical Society*, **137**, 2009 (1990).

20. J. R. Dahn, E. W. Fuller, M. Obrovac and U. von Sacken, *Solid State Ionics*, **69**, 265 (1994).

21. D. Guyomard and J. M. Tarascon, *Solid State Ionics*, **69**, 222 (1994).

22. B. A. Johnson and R. E. White, *Journal of Power Sources*, **70**, 48 (1998).

23. X. Zhang, B. Winget, M. Doeff, J. W. Evans and T. M. Devine, *Journal of the Electrochemical Society*, **152**, B448 (2005).

24. J. W. Braithwaite, A. Gonzales, G. Nagasubramanian, S. J. Lucero, D. E. Peebles, J. A. Ohlhausen and W. R. Cieslak, *Journal of the Electrochemical Society*, **146**, 448 (1999).

25. T. Aoshima, K. Okahara, C. Kiyohara and K. Shizuka, *Journal of Power Sources*, **97–98**, 377 (2001).

26. J. Lu, C. Zhan, T. Wu, J. Wen, Y. Lei, A. J. Kropf, H. Wu, D. J. Miller, J. W. Elam, Y.-K. Sun, X. Qiu and K. Amine, *Nature Communications*, **5**, 5693 (2014).

27. J. L. Esbenshade and A. A. Gewirth, *Journal of the Electrochemical Society*, **161**, A513 (2014).

28. T. Joshi, K. Eom, G. Yushin and T. F. Fuller, *Journal of the Electrochemical Society*, **161**, A1915 (2014).

29. N. P. W. Pieczonka, Z. Liu, P. Lu, K. L. Olson, J. Moote, B. R. Powell and J.-H. Kim, *The Journal of Physical Chemistry C*, **117**, 15947 (2013).

30. M. Nie, J. Demeaux, B. T. Young, D. R. Heskett, Y. Chen, A. Bose, J. C. Woicik and B. L. Lucht, *Journal of the Electrochemical Society*, **162**, A7008 (2015).

31. H. Bryngelsson, M. Stjerndahl, T. Gustafsson and K. Edström, *Journal of Power Sources*, **174**, 970 (2007).

32. D. Aurbach, K. Gamolsky, B. Markovsky, Y. Gofer, M. Schmidt and U. Heider, *Electrochimica Acta*, **47**, 1423 (2002).

33. D. Aurbach, M. D. Levi, E. Levi and A. Schechter, *The Journal of Physical Chemistry B*, **101**, 2195 (1997).

34. D. Aurbach, B. Markovsky, I. Weissman, E. Levi and Y. Ein-Eli, *Electrochimica Acta*, **45**, 67 (1999).

35. F. A. Soto, Y. Ma, J. M. Martinez de la Hoz, J. M. Seminario and P. B. Balbuena, *Chemistry of Materials*, **27**, 7990 (2015).

36. G. V. Zhuang, H. Yang, B. Blizanac and P. N. Ross, *Electrochemical and Solid-State Letters*, **8**, A441 (2005).

37. M. Tang and J. Newman, *Journal of the Electrochemical Society*, **159**, A281 (2012).

38. D. Goers, M. Holzapfel, W. Scheifele, E. Lehmann, P. Vontobel and P. Novák, *Journal of Power Sources*, **130**, 221 (2004).

39. M. Lanz and P. Novák, *Journal of Power Sources*, **102**, 277 (2001).

40. W. H. Kong, H. Li, X. J. Huang and L. Q. Chen, *Journal of Power Sources*, **142**, 285 (2005).

41. S. Tsubouchi, Y. Domi, T. Doi, M. Ochida, H. Nakagawa, T. Yamanaka, T. Abe and Z. Ogumi, *Journal of the Electrochemical Society*, **160**, A575 (2013).

42. M. Murakami, H. Yamashige, H. Arai, Y. Uchimoto and Z. Ogumi, *Electrochemical and Solid-State Letters*, **14**, A134 (2011).

43. S. Shi, P. Lu, Z. Liu, Y. Qi, L. G. Hector, H. Li and S. J. Harris, *Journal of the American Chemical Society*, **134**, 15476 (2012).

44. M. Tang and J. Newman, *Journal of the Electrochemical Society*, **158**, A530 (2011).

45. K. Edström, M. Herstedt and D. P. Abraham, *Journal of Power Sources*, **153**, 380 (2006).

46. U. von Sacken, E. Nodwell, A. Sundler and J. R. Dahn, *Solid State Ionics*, **69**, 284 (1994).

47. A. v. Cresce, S. M. Russell, D. R. Baker, K. J. Gaskell and K. Xu, *Nano Letters*, **14**, 1405 (2014).

48. S.-H. Lee, H.-G. You, K.-S. Han, J. Kim, I.-H. Jung and J.-H. Song, *Journal of Power Sources*, **247**, 307 (2014).

49. A. Bordes, K. Eom and T. F. Fuller, *Journal of Power Sources*, **257**, 163 (2014).

50. H. Ota, Y. Sakata, A. Inoue and S. Yamaguchi, *Journal of the Electrochemical Society*, **151**, A1659 (2004).

51. C. S. Wang, A. J. Appleby and F. E. Little, *Journal of Electroanalytical Chemistry*, **497**, 33 (2001).

52. R. Yazami and Y. F. Reynier, *Electrochimica Acta*, **47**, 1217 (2002).

53. S. S. Zhang, M. S. Ding, K. Xu, J. Allen and T. R. Jow, *Electrochem. Solid State Lett.*, **4**, A206 (2001).

54. R. Yazami and P. Touzain, *Journal of Power Sources*, **9**, 365 (1983).

55. A. Funabiki, M. Inaba and Z. Ogumi, *Journal of Power Sources*, **68**, 227 (1997).

56. K. A. Hirasawa, T. Sato, H. Asahina, S. Yamaguchi and S. Mori, *Journal of the Electrochemical Society*, **144**, L81 (1997).

57. Y. Yamada, K. Miyazaki and T. Abe, *Langmuir*, **26**, 14990 (2010).

58. M. Tang, K. Miyazaki, T. Abe and J. Newman, *Journal of the Electrochemical Society*, **159**, A634 (2012).

59. M. Tang and J. Newman, *Journal of the Electrochemical Society*, **159**, A1922 (2012).

60. M. Tang, S. Lu and J. Newman, *Journal of the Electrochemical Society*, **159**, A1775 (2012).

61. R. R. Jaini, B. P. Setzler, A. G. Star and T. F. Fuller, *Journal of the Electrochemical Society*, **163**, A2185 (2016).

62. S. S. Zhang, *Journal of Power Sources*, **162**, 1379 (2006).

63. E. Markevich, G. Salitra, K. Fridman, R. Sharabi, G. Gershinsky, A. Garsuch, G. Semrau, M. A. Schmidt and D. Aurbach, *Langmuir* (2014).

64. M.-H. Ryou, G.-B. Han, Y. M. Lee, J.-N. Lee, D. J. Lee, Y. O. Yoon and J.-K. Park, *Electrochimica Acta*, **55**, 2073 (2010).

65. J. C. Burns, A. Kassam, N. N. Sinha, L. E. Downie, L. Solnickova, B. M. Way and J. R. Dahn, *Journal of the Electrochemical Society*, **160**, A1451 (2013).

66. S.-K. Jeong, M. Inaba, R. Mogi, Y. Iriyama, T. Abe and Z. Ogumi, *Langmuir*, **17**, 8281 (2001).

67. Y. Wang, S. Nakamura, K. Tasaki and P. B. Balbuena, *Journal of the American Chemical Society*, **124**, 4408 (2002).

68. M. Broussely, S. Herreyre, P. Biensan, P. Kasztejna, K. Nechev and R. J. Staniewicz, *Journal of Power Sources*, **97–98**, 13 (2001).

69. A. M. Colclasure, K. A. Smith and R. J. Kee, *Electrochimica Acta*, **58**, 33 (2011).

70. C. Wang, A. J. Appleby and F. E. Little, *Electrochimica Acta*, **46**, 1793 (2001).

71. H. J. Ploehn, P. Ramadass and R. E. White, *Journal of the Electrochemical Society*, **151**, A456 (2004).

72. V. Battaglia and J. Newman, *Journal of the Electrochemical Society*, **142**, 1423 (1995).

73. J. Christensen and J. Newman, *Journal of the Electrochemical Society*, **151**, A1977 (2004).

74. T. F. Fuller, M. Doyle and J. Newman, *Journal of the Electrochemical Society*, **141**, 1 (1994).

75. M. Doyle, T. F. Fuller and J. Newman, *Journal of the Electrochemical Society*, **140**, 1526 (1993).

76. D. D. Macdonald, *Electrochimica Acta*, **51**, 1376 (2006).

77. E. P. Randviir and C. E. Banks, *Analytical Methods*, **5**, 1098 (2013).

78. C. R. Yang, J. Y. Song, Y. Y. Wang and C. C. Wan, *J. Appl. Electrochem.*, **30**, 29 (2000).

79. J. S. Gnanaraj, R. W. Thompson, S. N. Iaconatti, J. F. DiCarlo and K. M. Abraham, *Electrochem. Solid State Lett.*, **8**, A128 (2005).

80. C.-F. Chen and P. P. Mukherjee, *Physical Chemistry Chemical Physics*, **17**, 9812 (2015).

81. D. Dees, E. Gunen, D. Abraham, A. Jansen and J. Prakash, *Journal of the Electrochemical Society*, **152**, A1409 (2005).

82. D. W. Dees, K. G. Gallagher, D. P. Abraham and A. N. Jansen, *Journal of the Electrochemical Society*, **160**, A478 (2013).

83. P. Gambhire, K. S. Hariharan, A. Khandelwal, V. S. Kumar, S. M. Kolake, D. Oh and S. Doo, *Journal of the Electrochemical Society*, **161**, A183 (2014).

84. J. Huang, H. Ge, Z. Li and J. Zhang, *Journal of the Electrochemical Society*, **161**, E3202 (2014).

85. J. Song and M. Z. Bazant, *Journal of the Electrochemical Society*, **160**, A15 (2013).

86. S. Sunde, I. A. Lervik, L. E. Owe and M. Tsypkin, *Journal of the Electrochemical Society*, **156**, B927 (2009).

87. M. Doyle, J. P. Meyers and J. Newman, *Journal of the Electrochemical Society*, **147**, 99 (2000).

88. N. Mellgren, S. Brown, M. Vynnycky and G. Lindbergh, *Journal of the Electrochemical Society*, **155**, A304 (2008).

89. M. R. Shoar Abouzari, F. Berkemeier, G. Schmitz and D. Wilmer, *Solid State Ionics*, **180**, 922 (2009).

90. M. Musiani, M. E. Orazem, N. Pébère, B. Tribollet and V. Vivier, *Journal of the Electrochemical Society*, **158**, C424 (2011).

91. M. E. Orazem, I. Frateur, B. Tribollet, V. Vivier, S. Marcelin, N. Pébère, A. L. Bunge, E. A. White, D. P. Riemer and M. Musiani, *Journal of the Electrochemical Society*, **160**, C215 (2013).

92. J. Bisquert, G. Garcia-Belmonte, F. Fabregat-Santiago, N. S. Ferriols, P. Bogdanoff and E. C. Pereira, *The Journal of Physical Chemistry B*, **104**, 2287 (2000).

93. U. Rammelt and G. Reinhard, *Corrosion Science*, **27**, 373 (1987).

94. R. de Levie, *Journal of Electroanalytical Chemistry and Interfacial Electrochemistry*, **281**, 1 (1990).

95. T. Pajkossy, *Journal of Electroanalytical Chemistry*, **364**, 111 (1994).

96. S. Devan, V. R. Subramanian and R. E. White, *Journal of the Electrochemical Society*, **151**, A905 (2004).

97. C. C. Nguyen and B. L. Lucht, *Journal of the Electrochemical Society*, **161**, A1933 (2014).

98. I. A. Shkrob, Y. Zhu, T. W. Marin and D. Abraham, *The Journal of Physical Chemistry C*, **117**, 19255 (2013).

99. S. E. Sloop, J. K. Pugh, S. Wang, J. B. Kerr and K. Kinoshita, *Electrochemical and Solid-State Letters*, **4**, A42 (2001).

100. H. Tavassol, J. W. Buthker, G. A. Ferguson, L. A. Curtiss and A. A. Gewirth, *Journal of the Electrochemical Society*, **159**, A730 (2012).

101. I. A. Shkrob, Y. Zhu, T. W. Marin and D. Abraham, *J. Phys. Chem. C*, **117**, 19270 (2013).

102. H. Shin, J. Park, A. M. Sastry and W. Lu, *Journal of the Electrochemical Society*, **162**, A1683 (2015).

103. C. Delacourt, *Journal of the Electrochemical Society*, **160**, A1997 (2013).

104. X. Zhang, R. Kostecki, T. J. Richardson, J. K. Pugh and P. N. Ross, *Journal of the Electrochemical Society*, **148**, A1341 (2001).

105. P. A. Staley, C. M. Newell, D. P. Pullman and D. K. Smith, *Analytical Chemistry*, **86**, 10917 (2014).

106. C. O. Laoire, E. Plichta, M. Hendrickson, S. Mukerjee and K. M. Abraham, *Electrochimica Acta*, **54**, 6560 (2009).

107. B. Tjaden, S. J. Cooper, D. J. L. Brett, D. Kramer and P. R. Shearing, *Current Opinion in Chemical Engineering*, **12**, 44 (2016).

108. M. Nie, D. Chalasani, D. P. Abraham, Y. Chen, A. Bose and B. L. Lucht, *The Journal of Physical Chemistry C*, **117**, 1257 (2013).

109. C. R. Yang, Y. Y. Wang and C. C. Wan, *Journal of Power Sources*, **72**, 66 (1998).

110. D. Aurbach, B. Markovsky, A. Shechter, Y. Ein-Eli and H. Cohen, *Journal of the Electrochemical Society*, **143**, 3809 (1996).

111. Y. Yamada, Y. Takazawa, K. Miyazaki and T. Abe, *The Journal of Physical Chemistry C*, **114**, 11680 (2010).

112. L. Liao, P. Zuo, Y. Ma, Y. An, G. Yin and Y. Gao, *Electrochimica Acta*, **74**, 260 (2012).

113. T. DuBeshter, P. K. Sinha, A. Sakars, G. W. Fly and J. Jorne, *Journal of the Electrochemical Society*, **161**, A599 (2014).

114. K. Eom, T. Joshi, A. Bordes, I. Do and T. F. Fuller, *Journal of Power Sources*, **249**, 118 (2014).

115. J. P. Meyers, M. Doyle, R. M. Darling and J. Newman, *Journal of the Electrochemical Society*, **147**, 2930 (2000).

116. D. P. Abraham, S. Kawauchi and D. W. Dees, *Electrochimica Acta*, **53**, 2121 (2008).

117. T. G. Zavalis, M. Klett, M. H. Kjell, M. Behm, R. W. Lindström and G. Lindbergh, *Electrochimica Acta*, **110**, 335 (2013).

118. S. E. Li, B. Wang, H. Peng and X. Hu, *Journal of Power Sources*, **258**, 9 (2014).

119. P. Ramadass, B. Haran, P. M. Gomadam, R. White and B. N. Popov, *Journal of the Electrochemical Society*, **151**, A196 (2004).

120. M. Safari and C. Delacourt, *Journal of the Electrochemical Society*, **158**, A562 (2011).

121. Y. Wei, J. Zheng, S. Cui, X. Song, Y. Su, W. Deng, Z. Wu, X. Wang, W. Wang, M. Rao, Y. Lin, C. Wang, K. Amine and F. Pan, *Journal of the American Chemical Society*, **137**, 8364 (2015).

122. M. Z. Kufian and S. R. Majid, *Ionics*, **16**, 409 (2010).

123. V. Srinivasan and J. Newman, *Journal of the Electrochemical Society*, **151**, A1530 (2004).

124. P. Los, A. Lasia, J. Fournier, L. Brossard and H. Ménard, *Journal of the Electrochemical Society*, **141**, 2716 (1994).

125. V. Etacheri, O. Haik, Y. Goffer, G. A. Roberts, I. C. Stefan, R. Fasching and D. Aurbach, *Langmuir*, **28**, 965 (2012).

126. S. J. An, J. Li, C. Daniel, D. Mohanty, S. Nagpure and D. L. Wood Iii, *Carbon*, **105**, 52 (2016).

127. S. Frisco, A. Kumar, J. F. Whitacre and S. Litster, *Journal of the Electrochemical Society*, **163**, A2636 (2016).

128. D. R. Franceschetti, J. R. Macdonald and R. P. Buck, *Journal of the Electrochemical Society*, **138**, 1368 (1991).

CHAPTER 6

SUMMARY AND RECOMMENDATIONS

We have presented a detailed investigation of the role of surface films on electrodes used in lithium-ion batteries (LiBs). In the negative electrode of a LiB, the surface film is referred to as the solid electrolyte interphase (SEI). The SEI is a complicated but essential portion of a LiB because it reduces the rate of capacity fade. Therefore, there is much interest in understanding the growth and physical characteristics of the SEI.

In the first part of our work, we are motivated by a less than intuitive observation frequently reported in the literature: SEIs formed from additive-containing electrolytes are thinner than those formed with neat electrolyte, yet are more effective in slowing the rate of capacity fade. The observation of a thinner SEI is consistent with less capacity fade. However, combined with the observation on capacity fade, the observation is counterintuitive. That is, solvent transport across a thinner SEI should act to accelerate the rate of capacity fade.

We investigate these observations using a model system that contains an *in situ* electrochemical probe. The electrode is planar glassy carbon, and the electrochemical probe is the ferrocene redox shuttle. The ferrocene redox shuttle is assumed analogous to solvent molecules in the solution phase. Glassy carbon is shown to be an ideal electrode by cyclic voltammetry. The electrode has no intercalation capacity, and therefore any reduction on the surface only forms SEI. Neat and additive-containing electrolytes are used to form SEIs at 0.6 V *vs.* Li/Li^+. Passivation curves display characteristics of

transport limited growth and follow a noticeable pattern amongst the three electrolytes. Neat electrolyte is observed to passivate the surface more than additive-containing electrolyte for the same amount of hold time from impedance spectroscopy. From microscopy, neat electrolyte is found to form thicker SEIs than additive-containing electrolyte. The combined observations, both impedance and SEI thickness, for neat and additive-containing electrolyte SEIs are found to be in contrast to observations in the literature. Additionally, each electrolyte produces unexpectedly thick SEIs. Polymerization reactions are suspected to cause the formation of surprisingly thick SEIs. Finally, it is speculated that either the assumption that ferrocene is analogous to solvent molecules is incorrect or the benefits of additives are not observed until lower passivation potentials are reached.

In the second part of our work, we build on part one to determine if the benefit of additives is ever observed in this system. The electrode is passivated at lower potentials that are more likely reached in practical LiBs. Two potentials are chosen for passivation, 0.3 V and 0.1 V. The same behavior that characterizes the findings at 0.6 V is again observed at 0.3 V. For the same magnitude of formation charge, neat electrolyte is more passivating than additive electrolyte. At 0.1 V, under certain conditions, additive-containing electrolyte becomes as passivating as neat electrolyte for the same amount of formation charge. However, the benefits of additives are never observed in the system. The evidence presented suggests that ferrocene is not an analog of solvent.

In the third part of our work, we extend our previous investigations of negative electrode surface films to the positive electrode of a real LiB. Fresh and calendar aged

LiBs are found to have significant differences in their impedance responses. In the associated impedance response of the cathode, a new arc is observed following calendar aging. Through microscopic analysis, a surface film on the cathode particles is found to develop in the aged cell. A full-cell physics-based model is developed to simulate the impedance response to determine if the cathode surface film results in a new arc. Simulation of the impedance response suggests that, although it is possible that the film causes a new arc in the spectrum, the result is not likely. The low calculated relative permittivity of the film is used to justify the conclusion.

Despite not behaving identically to solvent molecules, we recommend further investigation of surface passivation with ferrocene but instead on ionic liquid electrolytes. These electrolytes can be advantageous for high temperature applications, but a very scarce amount of literature is available on their performance. In our current setup that uses a stationary electrode, the system has internal kinetic, internal mass-transport, and external mass-transport resistances. We use EIS to separate time constants to isolate the internal, kinetic, and total mass-transport resistances. We suggest using a rotating disk electrode (RDE) for the investigation of ionic liquid SEIs. The RDE allows removing all external mass transport limitations. In an RDE setup, we suggest performing cyclic voltammetry of the ferrocene shuttle after forming the SEI in lieu of measuring the impedance response. The CV allows separation of the internal kinetics from total mass transport. In this case, the external mass-transport limitations would no longer be present. Therefore, mass-transport would only be of internal ferrocene transport through the SEI. This ensures that kinetic and mass-transport parameters can be uniquely extracted and give the study a more quantitative perspective.

Additionally, we recommend reformulating the full-cell impedance response model to include a coupling of the Butler-Volmer kinetic expression to the bulk electrolyte concentration. We suspect that the new arc observed in the experimental impedance response data is a result of concentration gradients in the solution phase of the electrolyte.